INFORMATION TO USERS

This manuscript has been reproduced from the microfilm master. UMI films the text directly from the original or copy submitted. Thus, some thesis and dissertation copies are in typewriter face, while others may be from any type of computer printer.

The quality of this reproduction is dependent upon the quality of the copy submitted. Broken or indistinct print, colored or poor quality illustrations and photographs, print bleedthrough, substandard margins, and improper alignment can adversely affect reproduction.

In the unlikely event that the author did not send UMI a complete manuscript and there are missing pages, these will be noted. Also, if unauthorized copyright material had to be removed, a note will indicate the deletion.

Oversize materials (e.g., maps, drawings, charts) are reproduced by sectioning the original, beginning at the upper left-hand corner and continuing from left to right in equal sections with small overlaps.

ProQuest Information and Learning
300 North Zeeb Road, Ann Arbor, MI 48106-1346 USA
800-521-0600

UMI®

THEORETICAL SPECTRA AND ATMOSPHERES OF EXTRASOLAR GIANT PLANETS

by

David L. Sudarsky

A Dissertation Submitted to the Faculty of the

DEPARTMENT OF ASTRONOMY

In Partial Fulfillment of the Requirements
For the Degree of

DOCTOR OF PHILOSOPHY

In the Graduate College

THE UNIVERSITY OF ARIZONA

2 0 0 2

UMI Number: 3060957

UMI®

UMI Microform 3060957

Copyright 2002 by ProQuest Information and Learning Company.
All rights reserved. This microform edition is protected against
unauthorized copying under Title 17, United States Code.

ProQuest Information and Learning Company
300 North Zeeb Road
P.O. Box 1346
Ann Arbor, MI 48106-1346

THE UNIVERSITY OF ARIZONA ®
GRADUATE COLLEGE

As members of the Final Examination Committee, we certify that we have read the dissertation prepared by David Sudarsky

entitled Theoretical Spectra and Atmospheres of Extrasolar Giant Planets

and recommend that it be accepted as fulfilling the dissertation requirement for the Degree of Doctor of Philosophy

Adam Burrows 8/15/2002
Adam Burrows Date

James W. Liebert 8/15/02
James W. Liebert Date

William B. Hubbard 8/15/02
William B. Hubbard Date

8/15/02
Jonathan Lunine Date

Date

Final approval and acceptance of this dissertation is contingent upon the candidate's submission of the final copy of the dissertation to the Graduate College.

I hereby certify that I have read this dissertation prepared under my direction and recommend that it be accepted as fulfilling the dissertation requirement.

Adam Burrows 8/15/2002
Dissertation Director Adam Burrows Date

STATEMENT BY AUTHOR

This dissertation has been submitted in partial fulfillment of requirements for an advanced degree at The University of Arizona and is deposited in the University Library to be made available to borrowers under rules of the Library.

Brief quotations from this dissertation are allowable without special permission, provided that accurate acknowledgment of source is made. Requests for permission for extended quotation from or reproduction of this manuscript in whole or in part may be granted by the head of the major department or the Dean of the Graduate College when in his or her judgment the proposed use of the material is in the interests of scholarship. In all other instances, however, permission must be obtained from the author.

SIGNED: ____________________

ACKNOWLEDGMENTS

The present work could not have been completed without the important contributions and support of a number of individuals, to whom I am very grateful. First, I would like to thank my advisor, Adam Burrows, both for his scientific vision and his general enthusiasm. Ivan Hubeny has also been integral to this project by providing his stellar atmosphere code, a modified version of which was used in this work.

My thanks go out to collaborators from the Lunar and Planetary Laboratory, Bill Hubbard, Jonathan Lunine, Jonathan Fortney, and Curtis Cooper, for their useful contributions and insightful discussions. Other collaborators from Steward Observatory, Phil Pinto and Christopher Sharp, and Drew Milsom from Physics, have also been very helpful in the completion of this dissertation.

I am also grateful to those that did not work directly with me on this project but have provided a beneficial work environment and useful discussions, including Jim Liebert, Todd Thompson, Audra Baleisis, Jennifer Scott, Aimee Hungerford, and the secretaries and personnel of Steward Observatory. Finally, I would like to express my deep appreciation to my wife, Tami Rogers, for her invaluable support, suggestions, and perseverance.

DEDICATION

Dedicated to my parents, for their truly unconditional support.

TABLE OF CONTENTS

LIST OF FIGURES 9

ABSTRACT 13

1 EXTRASOLAR PLANETS: A NEW FIELD IN ASTRONOMY AND PLANETARY SCIENCES 14

1.1 Atmospheres of EGPs 18

1.2 An In-Depth Study of EGP Systems 21

2 NUMERICAL MODELING OF EXTRASOLAR GIANT PLANETS (EGPS) AND BROWN DWARFS 24

2.1 Feautrier Method 26

2.2 True Asymmetric Feautrier Method 27

2.3 Discontinuous Finite Element Method 30

2.4 Direct Solution of the Transfer Equation 32

2.5 Achieving Radiative Equilibrium Via Accelerated Lambda Iteration . 34

3 ATMOSPHERIC COMPOSITION 38

3.1 Chemical Abundances in EGPs and Brown Dwarfs 39

3.2 Composition Profiles 40

3.3 Condensation and Rainout 42

3.4 Gravitational Settling Versus True Equilibrium 45

3.5 Photoionization of Alkali Metals 46

4 ATOMIC AND MOLECULAR SCATTERING AND ABSORPTION . 55

4.1 Molecular Absorption 55

4.2 Atomic Species 57

4.3 Total Gaseous Absorption Opacities 57

4.4 Rayleigh Scattering 58

5 MIE THEORY AND OPTICAL PROPERTIES OF CONDENSATES 67
5.1 Mie Theory 69
5.2 Optical Properties of Condensates Relevant to EGP Atmospheres . . 71
5.3 Particle Size Distributions 73
5.4 A Sample of the Results: Condensate vs. Gas Opacities 74

6 CLASSES OF EXTRASOLAR GIANT PLANETS 83
6.1 Jovian Class I EGPs 85
6.2 Water Class II EGPs 86
6.3 Gaseous Class III EGPs 87
6.4 Close-In Class IV EGPs 89
6.5 Class V Roasters 90

7 SPECIFIC EGP MODELS 102
7.1 The Upsilon Andromeda System 104
7.2 The Transiting Planet, HD 209458b 108
7.3 Orbiting a Cool Star: The GJ 876 System 111
7.4 51 Pegasi b and Tau Bootes b 112
7.5 The 55 Cancri System and its New Long-Period Planet 116
7.6 Some Other EGPs of Interest 119
7.7 Jupiter and Jovian-Class Planets 121

8 PARAMETER STUDIES 150
8.1 A Generic Model Sequence from 5AU to 0.05 AU 150
8.2 Effects of Inner Boundary Flux Variation 152
8.3 Effects of Surface Gravity Variation 154
8.4 Effects of Condensate Particle Size Variation 156
8.5 Photoionization Depths of the Alkali Metals 157

9 DETECTION AND IMAGING OF EGPs IN LIGHT OF THEORETICAL MODELS 170

9.1 Spectral Separation Methods 171

9.2 Ground-Based Differential Direct Imaging 172

9.3 Transit Searches and Photometric Reflected Light Detection 173

9.4 Interferometric Imaging 176

9.5 Interferometric Astrometry 179

9.6 Coronagraphic Imaging 180

REFERENCES 183

LIST OF FIGURES

2.1 Comparison of Asymmetric Feautrier code results to Monte Carlo and analytic solutions for a deep. homogeneous atmospheres. 37

3.1 Equal abundance boundaries for CO-CH_4 and for N_2-NH_3 in temperature-pressure space. 50

3.2 Plot of gas-phase number fractions in the atmosphere of a close-in EGP. 51

3.3 Plot of gas-phase number fractions in the atmosphere of a brown dwarf with $T_{\rm eff}$= 1000 K. 52

3.4 Plot of gas-phase number fractions in the atmosphere of a cool EGP. 53

3.5 Pressure depth of sodium ionization versus angle from the substellar point in the atmosphere of a close-in EGP. 54

4.1 Water. methane. and CO absorption cross sections at T = 1600 K. P = 1 bar. 60

4.2 Water. methane. and ammonia absorption cross sections at T = 200 K. P = 1 bar. 61

4.3 Water, methane. and CO absorption cross sections at T = 1600 K. P = 1 bar (out to 30 μm). 62

4.4 Water, methane, and ammonia absorption cross sections at T = 200 K. P = 1 bar (out to 30 μm). 63

4.5 H_2-H_2 collision-induced absorption (CIA) cross sections at various temperatures and pressures. 64

4.6 LTE absorption cross sections of the alkali metals, lithium. sodium. potassium, rubidium, and cesium. 65

4.7 Depiction of the differences in total. abundance-weighted gaseous opacities in hot and cold EGP atmospheres at P = 1 bar. 66

5.1 Mie theory extinction and scattering results for ice spheres of radius 0.5, 5, and 50 μm. 76

5.2 Mie theory scattering asymmetry factor results for ice spheres of radius 0.5, 5, and 50 μm. 77

5.3 Real indices of refraction for condensates relevant to the atmospheres of EGPs. 78

5.4 Imaginary indices of refraction for condensates relevant to the atmospheres of EGPs. 79

5.5 Imaginary indices of refraction for ammonia ice and candidate nonequilibrium species. 80

5.6 Absorption and scattering opacities of forsterite and iron compared with the total gaseous opacity at T = 1600 K, P = 10 mbar. 81

5.7 Absorption and scattering opacities of condensed water (ice) compared with the total gaseous opacity at T = 250 K, P = 1 bar. . 82

6.1 Temperature-Pressure profiles for each of the EGP classes. 92

6.2 Emergent spectrum of a Class I EGP. 93

6.3 Emergent spectrum of a Class II EGP. 94

6.4 Emergent spectrum of a Class III EGP. 95

6.5 Comparison of the T-P structure of a Class III EGP with that of a cloud-free brown dwarf of the same effective temperature and surface gravity. 96

6.6 Comparison of the emergent spectrum of a Class III EGP with that of a cloud-free brown dwarf of the same surface gravity and total integrated emergent flux. 97

6.7 Emergent spectrum of a Class IV EGP. 98

6.8 Effect of a deep silicate cloud on the T-P structure of a Class IV EGP. 99

6.9 Emergent spectrum of a Class IV EGP with its deep silicate cloud relative to that of a cloud-free model. 100

6.10 Emergent spectrum of a Class V EGP. 101

7.1 Visible and near-infrared spectra of υ b, c, and d. 127

7.2 T-P profiles of υ And b, c, and d. 128

7.3 Fiducial T-P profile of υ And b versus that of a cloud-free model . . . 129

7.4 Fiducial model spectrum of υ And b versus that of a cloud-free model. 130

7.5 Wavelength-dependent planet-to-star flux ratios for υ And b, c, and d. 131

7.6 Visible and near-infrared spectrum of HD209458b. 132

7.7 T-P profile of HD 209458b. 133

7.8 Wavelength-dependent planet-to-star flux ratio of HD209458b. 134

7.9 Visible and near-infrared spectra of GJ 876b and c. 135

7.10 T-P profiles of GJ 876 b and c. 136

7.11 Wavelength-dependent planet-to-star flux ratios for GJ 876 b and c. . 137

7.12 Cloud-free 51 Peg b T-P profiles with incident flux weighting of 1/4, 1/2, and 1. 138

7.13 T-P profiles of τ Boo b and 51 Peg b. 139

7.14 Visible and near-infrared spectra of τ Boo b and 51 Peg b. 140

7.15 Wavelength-dependent planet-to-star flux ratios for τ Boo b and 51 Peg b. 141

7.16 Visible and near-infrared spectra of 55 Cancri b and d. 142

7.17 T-P profiles of 55 Cancri b and d. 143

7.18 Wavelength-dependent planet-to-star flux ratios for 55 Cnc b and d from 0.4 to 30 μm. 144

7.19 Visible model spectra of HD 114762b for various surface gravities and inner boundary fluxes. 145

7.20 Model spectrum of ϵ Eri b from 0.4 to 30 μm. 146

7.21 Visible and near-infrared spectra of HD 83443b, HD 114762b, and ϵ Eri b. 147

7.22 T-P profiles of HD 83443b, HD 114762 b, and ϵ Eri b. 148

7.23 Geometric albedo spectrum of Jupiter. 149

8.1 Cloud-free EGP T-P profiles as a function of orbital distance from a G0V primary. 159

8.2 Cloud-free EGP emergent spectra as a function of orbital distance from a G0V primary. 160

8.3 A comparison of the visible spectra of cloud-free EGPs orbiting a G0V primary with that of an isolated brown dwarf. 161

8.4 Comparison of the visible spectra of cloud-free EGPs without Rayleigh scattering with that of an isolated brown dwarf. 162

8.5 EGP T-P structure as a function of inner boundary flux. 163

8.6 EGP emergent spectra as a function of inner boundary flux. 164

8.7 EGP T-P structure as a function of surface gravity. 165

8.8 EGP emergent spectra as a function of surface gravity. 166

8.9 Effects of cloud particle size variation on visible and near-infrared emergent spectrum of a Class II EGP. 167

8.10 Effects of cloud particle size variation on the emergent spectrum of a Class II EGP out to 30 μm. 168

8.11 Simulated spectral effects of photoionization in the outermost atmosphere of a Class V roaster. 169

ABSTRACT

This work is a detailed study of extrasolar giant planet (EGP) atmospheres and spectra. Models representative of the full range of systems known today are included, from the extreme close-in EGPs to Jovian-like planets at large orbital radii. Using a self-consistent planar atmosphere code along with the latest atomic and molecular cross sections, cloud models, Mie theory treatment of grain scattering and absorption, and incident stellar fluxes, I produce an extensive set of theoretical EGP atmosphere models and emergent spectra.

The emergent spectra of EGPs strongly depend upon their outer atmospheric chemical compositions, which in turn depend upon the run of temperature and pressure with atmospheric depth. Because of qualitative similarities in the compositions and spectra of objects within several broad temperature ranges, EGPs fall naturally into five groups, or composition classes. Such a classification scheme, however preliminary, brings a degree of order to the rich variety of EGP systems known to exist today.

Generic models that represent the EGP classes, as well as a set of specific models for a number of important systems that have been detected, are provided. Furthermore, the effects on emergent EGP spectra of varying key parameters such as surface gravity, cloud particle sizes, orbital distance, etc. are modeled. A discussion of current and future ground-based and space-based missions to detect and characterize EGPs in light of theoretical spectral models is included to facilitate an understanding of which systems are most likely to be studied successfully.

1 EXTRASOLAR PLANETS: A NEW FIELD IN ASTRONOMY AND PLANETARY SCIENCES

Since the first detection of an extrasolar giant planet (EGP) by radial velocity measurements in 1995 (51 Pegasi b; Mayor & Queloz 1995), a great variety of EGPs has been revealed. To date, there are roughly 100 known planets orbiting nearby stars, and many hundreds more are expected within the next decade.

While it is not often that a new subfield of astronomy and planetary sciences is undertaken with such intensity, as has been the case these past few years, the existence of planets in orbit about other stars should not come as a great surprise. There has never been a good physical reason for believing that planets exist only around our main sequence star, with the countless others standing barren of such bodies. But what did come as a great surprise was the proximity of the gas giant, 51 Peg b, to its main sequence star. At 0.05 AU, it is 100 times closer to its star than Jupiter is to the Sun. Our familiar notion of the gas giants at large orbital distances and terrestrial planets at small distances has forever been shattered by 51 Peg b and its kin. The radial velocity method clearly favors the detection of massive objects at small orbital distances, but this fact does not make the discovery of 51 Peg b any less astonishing.

To date, detections of EGPs have been via Doppler spectroscopy of their central stars. Because such detections do not reveal the inclination of the planet's orbit, only the minimum or projected mass (M$\sin i$) can be inferred. Currently, the range of known M$\sin i$ ranges from less than half a Saturn mass to over 10 Jupiter masses. Some of the more massive objects may turn out to be mass brown dwarfs or even M-dwarfs in nearly face-on orbits, but a firm collection of EGPs is now in hand. One object, HD 209458b, actually transits its primary, revealing its edge-on orbit and, hence, its mass of $0.69 M_J$. However, with the majority of EGPs, we are not so fortunate, and accurate astrometric measurements will need to be made to obtain orbital inclinations. What is noteworthy is the fact that the majority of close-in EGPs have a projected mass under $1 M_J$, even though the more massive objects are more likely to be detected by this method. The more massive objects detected tend to be found at larger distances, many beyond 1 AU. The absence of massive close-in objects is a subject that many dynamicists are trying to understand. It seems that the very existence of close-in EGPs is a consequence of planet-disk interaction and migration, not *in situ* formation.

The mass of an EGP is just one parameter. Just as important to its general structure and even more important in determining the character of its outer atmosphere is the orbital distance of an EGP from its primary. To date, EGP semimajor axes cover the range, 0.038 AU to $\sim$ 5.5 AU, a range that is expected to expand outward as detection techniques and instrumentation continue to improve. Orbital eccentricities are near zero for close-in objects, as expected due to the tidal dissipation of their orbits. But for EGPs at larger orbital distances, eccentricities are spread from $\sim$ 0.03 to 0.9. The most eccentric EGP, HD 80606b, has an eccentricity of 0.927!

The central stars around which planets have been found range from main sequence spectral types F7 to K2. which is in part a function of the target lists of the radial-velocity searches. The stellar metallicities vary significantly as well. with [Fe/H] ranging from ~ -0.6 to +0.4; the majority are above solar metallicity ([Fe/H] = 0).

The modeling of EGP atmospheres is important for at least two major reasons. From the theorist's perspective. a physical understanding of EGPs is itself a worthy endeavor. Since the emergent spectra of EGPs are determined largely by the outer atmospheres of these objects. when the colors and. ultimately. the spectra of EGPs are measured. theoretical atmospheres will be essential in the interpretation of the data. and, hence. to our knowledge of the physical nature of EGPs. From an observer's perspective—and this is the more pressing of the two perspectives—theoretical spectral models are important to EGP spectral searches and imaging. Observers need to know which regions of the spectrum provide the greatest chance for detection, while avoiding those regions in which attempts are likely to be futile. So even at this very early stage, observation and theory are working together.

A host of exciting ground-based and space-based missions for the detection. characterization. and imaging of EGPs are well underway or under serious consideration, many of which I will review in Chapter 9. Ground-based interferometric endeavors include astrometry with the Very Large Telescope Interferometer (VLTI; Paresce 2001), astrometry and differential phase methods with the Keck Interferometer (van Belle & Vasisht 1998; Akeson & Swain 2000), and nulling interferometry with the Large Binocular Telescope Interferometer (LBTI; Hinz 2001). Ground-based differential direct imaging with ARIES on the MMT (Freed et al. 2002) and with TRIDENT (Marois 2002) will attempt to "subtract out" starlight by differencing images in two or more narrow bands in which only the planetary spectrum is expected to differ substantially. Such imaging techniques may work well in conjunction with adaptive optics systems on large ground-based telescopes.

Masses of new EGPs will be revealed when new transits are detected by the many ground-based programs in operation, such as STARE (Brown & Charbonneau 1999), OGLE (Udalski et al. 2002), TEMPEST (Baliber & Cochran 2001), and many others. Space-based instruments, such as Kepler (Koch et al. 1998), MOST (Matthews et al. 2001), COROT (Antonello & Ruiz), and MONS (Christensen-Dalsgaard 2000) will be able to detect transits with very high photometric precision. Additionally, such sensitive instruments should be able to discern reflected light from EGPs that do *not* transit their primaries, depending upon the details of the planetary phase functions. The eventual microarcsecond astrometry of the Space Interferometry Mission (SIM; Unwin & Shao 2000) could reveal the orbital inclinations and, hence, the masses of virtually all known EGPs within the next decade. Perhaps of even greater import are space-based coronagraphic imaging missions, which may include *Eclipse* (Trauger et al. 2000; Trauger et al. 2001), the Jovian Planet Finder (JPF; Clampin et al. 2001), the Extra-Solar Planet Imager (ESPI; Melnick et al. 2001), ECLIPSE, and NIRcam on the Next Generation Space Telescope (NGST; Rieke et al. 2002). Such advanced instruments are specifically designed for high-contrast imaging and/or spectrophotometry of EGPs. These missions should provide fundamental EGP atmospheric data, which in combination with theoretical models is certain to forward our understanding of these systems.

1.1. Atmospheres of EGPs

Despite the different formation scenarios of brown dwarfs and EGPs. their atmospheres share many attributes. Both are composed primarily of molecular hydrogen and helium gas. with a mix of heavier elements. mostly in molecular form. Furthermore. their atmospheric temperatures and densities can be comparable. despite notable differences in their temperature-pressure (T-P) profiles. and both EGPs and brown dwarfs are mostly convective. with an outer atmospheric radiative zone. Condensates. from silicates and iron grains to water clouds are expected to exist in a large subset of EGPs and brown dwarfs.

While there are many similarities with brown dwarfs. external stellar irradiation can have an overwhelming influence on EGP atmospheres. particularly for the very close-in objects. while most brown dwarfs (including those in binary systems) experience little or no external radiation. At the very least. the heating of an EGP atmosphere by such irradiation alters its equilibrium chemical composition and. hence. its emergent spectrum. Furthermore. the spectrum of an EGP will differ from that of a brown dwarf due to the reflection of starlight by condensates in its outer atmosphere and/or due to Rayleigh scattering, phenomenona largely responsible for the visible and near-infrared spectra of the giant (and other) planets of our Solar System. While one cannot cleanly split the emergent spectrum of an EGP into reflected light and emitted light, due to multiple scattering, absorption and re-emission. the vast majority of the flux in the visible region for an EGP of moderate to large orbital distance is reflected star light. EGPs just are not hot enough to emit large thermal fluxes in this region of the spectrum.

Early investigations of EGP atmospheres and spectra neglected thermal emission and concentrated on albedo and reflection spectra for a range of EGP compositions. using planar radiative transfer codes. Marley et al. (1999) used T-P profiles of isolated brown dwarfs. while Sudarsky et al. (2000) used both isolated and more nearly isothermal profiles to bracket the effects of compositional differences on the albedo and reflection spectra of EGPs. Albedo and reflection models provide useful spectral information for the full range of EGPs. although they are most accurate for objects at moderate to large orbital distances.

The move toward fully self-consistent atmosphere models of close-in EGPs was begun by Seager & Sasselov (1999) and Goukenleuque et al. (2000) using modified planar stellar atmosphere codes. With incoming fluxes at both boundaries (the outer due to the central star and the inner due to the internal luminosity of the EGP). the T-P profile is adjusted iteratively until the net flux at every depth zone is the same (or nearly so). Relative to a brown dwarf atmosphere of similar temperature. the resulting profile is more isothermal due to outer atmospheric heating by the incident stellar flux. Seager & Sasselov explored the differences between cloud-free and dusty atmospheres and used basic equilibrium gas abundances without the alkali metals. A similar approach was taken by Goukenleque et al. , except that their deep silicate cloud layer acted as a reflecting layer at the lower boundary; radiative processes within and below the cloud were not considered.

Additional self-consistent modeling of EGPs was completed by Seager. Whitney. and Sasselov (2000; hereafter SWS) and Barman, Hauschildt. and Allard (2001: hereafter BHA). SWS used a planar atmosphere code to model close-in EGPs. as in their previous work. but they also produced theoretical optical photometric light curves and polarization curves using phase functions from their separate 3-D Monte Carlo calculations. The effects of various condensates and particle sizes on the variability were investigated. BHA used a planar atmosphere code to model a range of EGP orbital distances from generic close-in objects to those at 1 AU. Both cloud-free and dusty atmospheric compositions were explored. Both groups assumed condensate layers with infinite scale heights (i.e. extending vertically to the lowest pressures of their models). Such models provide upper limits to the effects of condensates on the emergent spectra of EGPs, and along with the cloud-free models, they likely bracket the actual emergent spectra.

Unlike many stars, the temperatures in the outer atmospheres of EGPs and brown dwarfs generally are not high enough to ionize atoms or molecules thermally. However, the ultraviolet irradiation of EGPs by their central stars can excite or ionize atomic and molecular species directly from their ground states. Of particular importance in EGP atmospheres are the alkali metals, sodium and potassium, which are abundant in close-in EGPs. In brown dwarfs, the presence of these atoms in neutral form results in very strong resonance line absorption responsible for much of the character of the visible emergent spectra (Burrows et al. 2000; Burrows et al. 2002; Tsuji et al. 1999). Such absorption is also expected in hot EGPs, where the abundances of sodium and potassium are also quite substantial, although the degree of absorption could be reduced slightly due to the ionization of these atoms in the outermost atmosphere, since their ionization potentials are so low.

Unlike brown dwarfs, whose temperatures are not expected to vary significantly as a function of latitude or longitude, EGPs have a day side and a night side. Hence, an EGP atmospheric T-P profile may be a strong function of the angle from the substellar point, particularly for slow-rotating or close-in objects. This dependence surely will be a function of the planet's rotational period, although a proper understanding would require a radiative-hydrodynamic treatment, since winds will transport material from the higher-temperature day side to the night side of the planet. While such complex meteorology is beyond the scope of the present work, it is possible to compute the equilibrium temperature of the planet, the temperature it would have in the absence of an intrinsic luminosity, based on a few parameters: the stellar luminosity (L_*), the Bond albedo of the planet (A_B), and the orbital distance of the planet (a). The result is:

$$T_{\rm eq} = \left[\frac{(1 - A_B)L_*}{16\pi\sigma a^2 f}\right]^{1/4} \tag{1.1}$$

where σ is the Stefan-Boltzmann constant and the factor f is equal to unity for re-emission by the planet over its entire surface or equal to 0.5 for re-emission from only the illuminated hemisphere. This factor may tend toward unity for a planet that is rotating very quickly if the heat is redistributed well. For a slow rotator, this factor might be closer to 0.5 since re-radiation from the day side would be significantly greater than that from the night side. Note that for massive and/or young EGPs with sufficiently large orbital distances, $T_{\rm eff} > T_{\rm eq}$ because of their significant internal fluxes (where $T_{\rm eff}$ refers to $(F/\sigma)^{1/4}$ for an object in *isolation*).

1.2. An In-Depth Study of EGP Systems

The present work is a detailed study of EGP atmospheres and spectra, including individual models representative of the full range of systems known today. Using a self-consistent planar atmosphere code (Hubeny & Lanz 1995) along with the latest atomic and molecular cross sections, cloud models, Mie theory treatment of grain scattering and absorption, and incident stellar fluxes (Kurucz 1994), I produce an extensive set of theoretical EGP atmosphere models and emergent spectra.

The emergent spectra of EGPs strongly depend upon their outer atmospheric chemical compositions, which in turn depend upon the run of temperature and pressure with atmospheric depth. Because of qualitative similarities in the compositions and spectra of objects within several broad temperature ranges, EGPs fall naturally into groups, or composition classes, a major conclusion of this work. Such a classification scheme, however preliminary, brings a degree of order to the rich variety of EGP systems known to exist today.

A "Jovian" class of EGPs (Class I) exists at low temperatures ($\lesssim$ 150 K). Such planets are characterized by tropospheric ammonia clouds and strong gaseous methane absorption. Somewhat warmer Class II, or "water class" EGPs are affected by condensed H_2O, as well as water and methane vapor. When the outer atmosphere of an EGP is too hot for water to condense, radiation generally penetrates more deeply. In these objects, designated Class III, "clear" or "gaseous," due to a lack of condensation in their outer atmospheres, ro-vibrational molecular absorption is very strong. In those EGPs with exceedingly small orbital distance and outer atmospheric temperatures in excess of $\sim$ 900 K (Class IV), strongly pressure broadened resonance lines of sodium and potassium are expected to dominate the visible spectrum, while molecular absorption in the infrared remains strong. The very hot Class V EGPs orbit even closer to their primaries ($\sim$ 0.05 AU) than Class IV EGPs. These extremely close-in "roasters" are hot enough and/or have a low enough surface gravity that silicate and/or iron clouds condense high in the outer atmosphere and can have substantial effects on the emergent spectrum.

I begin in Chapter 2 with the basics of atmosphere modeling, including a discussion of numerical techniques and constraints. In Chapter 3, I review some basic equilibrium chemistry and explore the compositions of EGPs and brown dwarfs, discussing gas-phase species as well as condensates. I also present a simple ionization model for close-in EGPs. Chapter 4 delves into the actual atomic and gaseous opacities and their relevance in high-temperature and low-temperature EGPs. In Chapter 5, a discussion of Mie theory and the opacities of condensates is presented. Additionally, I compare condensate opacities with those of the gas-phase opacities in EGP atmospheres.

Chapter 6 begins my presentation of EGP model atmospheres and spectra. In particular, this chapter defines and describes the five different classes of EGPs, from the cold Class I Jovian-types to the hot "roasters" with orbital periods of only a few days. Chapter 7 is an extensive presentation of a number of prominent EGP systems. Atmosphere models and emergent spectra are provided for every such system. Planet-to-star flux ratios, of central importance to any campaign aiming to detect EGPs directly, are provided for most of these systems as well. As an important testbed for the theory of giant planet atmospheres, Jupiter provides us with important constraints on composition, T-P structure, etc. So I end this chapter with an in-depth discussion of Jupiter's atmosphere and I compare models of Jupiter's geometric albedo spectrum with that obtained observationally. In Chapter 8, the effects on emergent EGP spectra of varying key parameters such as surface gravity, cloud particle sizes, orbital distance, ionization depth, etc. are modeled. I conclude with Chapter 9, a discussion of current and future ground-based and space-based missions to detect and characterize EGPs. Where appropriate, I investigate the sensitivities of these instruments in the context of my theoretical models in order gain an understanding of which systems are most likely to be studied successfully.

2 NUMERICAL MODELING OF EXTRASOLAR GIANT PLANETS (EGPS) AND BROWN DWARFS

Numerical atmosphere modeling entails the combination of a radiative transfer technique with atmospheric structure and boundary constraints. Because the atmospheric temperature-pressure structure is almost always strongly coupled to the transfer of radiation, most methods converge on a self-consistent solution through an iterative process. The minimum requirements for a converged model include the satisfaction of hydrostatic equilibrium and a constant net flux of radiation throughout the atmosphere (constant to within some very small fraction, such as 0.1%). Often, additional constraints must be met, such as a requirement that the temperature at every pressure depth zone not vary by more than some minuscule fraction from the previous iteration.

There is a rich history of stellar atmosphere modeling, and these same basic techniques are used for brown dwarfs and EGPs. But unlike most stars, save the latest M-dwarfs, the outer atmospheres of substellar objects commonly contain condensed species, such as grains in relatively hot objects or water or ammonia clouds in cool EGPs. The usual treatment of the scattering of radiation in stellar atmospheres (by the Feautrier method and some other radiative transfer techniques) assumes forward-backward scattering symmetry (and often simply isotropic scattering), but condensates in brown dwarfs and EGPs typically scatter strongly in the forward direction. Relative to isotropic scattering, forward scattering reduces the albedo of an atmosphere, because on average more scattering events are required for a photon to emerge from the atmosphere before being absorbed by some species. A strictly proper treatment of the transfer of radiation in these objects must allow for such scattering asymmetry, although a useful approximation that allows one to maintain symmetric scattering numerically is used by most researchers: the asymmetry in the scattering of radiation is accounted for by reducing the actual scattering cross section by $1 - g$, where g signifies the averaged cosine of the scattering angle. In an optically thick medium, this so-called "transport cross section" mimics the effects of asymmetric scattering.

Because the outer atmospheres of brown dwarfs and EGPs are thin compared with the radii of these objects, I use a planar geometry for modeling both isolated and irradiated objects. A one-dimensional planar atmosphere code is the simplest means for the self-consistent modeling of EGPs, and virtually every consistent EGP atmosphere study to date has made use of such geometry. However, a 2-D or 3-D spherical atmosphere code would be more appropriate simply because, in reality, the incident radiation does not impinge evenly on the surface of an EGP. Unlike an isolated brown dwarf, it is likely that the atmospheric temperature-pressure structure of an EGP will vary substantially as a function of latitude and longitude. While a planar code cannot account for such variation, an approximate means of accounting for the different amounts of external flux received by a planet along its surface is to take a suitable average. No such adjustment would be necessary if it were a plane that was being irradiated. In that case, the total energy per second received by the plane would simply be $\pi R^2 F$, where F is the incident flux and R is the radius of the plane (or disk). If this same flux were received instead by a hemisphere, the energy would be distributed unevenly over an area of $2\pi R^2$. In this case, the average energy received per unit area would be $F/2$, not F. When using a planar code, one can account for this difference by weighting the incident flux by a factor of 1/2. Finally, if we want the average energy per second per unit area received by the full sphere (i.e. giving equal weighting to the night side of the planet), the adjustment is $F/4$. Such "redistribution" over the full sphere may be appropriate for a very fast rotator. Unless stated otherwise, in this work I choose to redistribute the incident energy over the front hemisphere of the planet only. However, some researches have chosen to redistribute over the full sphere, while others have chosen not to redistribute at all. I will point out these differences when comparing my models with others' results.

2.1. Feautrier Method

The Feautrier method (Mihalas 1978) is perhaps the most common approach to radiative transfer in stellar atmospheres, and it is used for my isolated brown dwarf models as well. This planar, second-order technique is a "two-stream" approach, treating an inward- and outward-directed radiation field (as a function of $\mu = \cos\theta$).

The fundamental transfer equation, separated into upward (I^+) and downward (I^-) components, is given by

$$\mu \frac{\partial I^+(\mu)}{\partial \tau} = I^+(\mu) - S(\mu), \tag{2.1}$$

and

$$-\mu \frac{\partial I^-(\mu)}{\partial \tau} = I^-(\mu) - S(\mu), \tag{2.2}$$

where I is a function of frequency and atmospheric depth as well, though I've dropped these subscripts here for clarity.

Using the symmetric and antisymmetric averages (the Feautrier variables),

$$u(\mu) = \frac{1}{2}[I^+(\mu) + I^-(\mu)], \tag{2.3}$$

and

$$v(\mu) = \frac{1}{2}[I^+(\mu) - I^-(\mu)], \tag{2.4}$$

two first-order equations are constructed, the first by adding eqs. (2.1) and (2.2), which yields

$$\mu\frac{\partial v(\mu)}{\partial\tau} = u(\mu) - S(\mu), \tag{2.5}$$

and the second by subtracting them, which gives

$$\mu\frac{\partial u(\mu)}{\partial\tau} = v(\mu). \tag{2.6}$$

By substituting eq. (2.6) into eq. (2.5), our desired second-order differential equation is obtained:

$$\mu^2\frac{\partial^2 u(\mu)}{\partial\tau^2} = u(\mu) - S(\mu). \tag{2.7}$$

The source function is given by

$$S(\mu) = S^T + \frac{1}{2}\sigma\int_{-1}^{1} R(\mu,\mu')I(\mu')d\mu', \tag{2.8}$$

where $R(\mu,\mu')$ is the azimuth-independent angular redistribution function (azimuthal symmetry is assumed) and σ is the single-scattering albedo, $\sigma = \sigma_{scat}/\sigma_{ext}$ (where σ_{scat} is the scattering cross section and σ_{ext} is the extinction cross section). S^T, the thermal part of the source function, is given by $(1-\sigma)B$, where B signifies the Planck function.

2.2. True Asymmetric Feautrier Method

A straightforward extension of the Feautrier technique that allows for true asymmetric scattering can be derived by separating the source funtion into upward-

and downward-propagating rays (Mihalas 1980; Milkey et al. 1975). Such an approach is quite suitable for atmospheres with ices or grains, but a drawback is the difficulty in integrating the asymmetric redistribution of radiation into a fully self-consistent atmosphere code. I use this method to model Jupiter's albedo spectrum given atmospheric details from the Galileo probe (see §7.7).

Dropping frequency and depth subscripts for clarity, the upward and downward components of the transfer equation are

$$\mu \frac{\partial I^+(\mu)}{\partial \tau} = I^+(\mu) - S^+(\mu) - S^T \tag{2.9}$$

and

$$-\mu \frac{\partial I^-(\mu)}{\partial \tau} = I^-(\mu) - S^-(\mu) - S^T, \tag{2.10}$$

where the scattering components of the source function are given by

$$S^+(\mu) = \frac{1}{2}\sigma \int_0^1 \left[R(\mu, \mu')I^+(\mu') + R(\mu, -\mu')I^-(\mu')\right] d\mu' \tag{2.11}$$

and

$$S^-(\mu) = \frac{1}{2}\sigma \int_0^1 \left[R(-\mu, \mu')I^+(\mu') + R(-\mu, -\mu')I^-(\mu')\right] d\mu'. \tag{2.12}$$

Forming symmetric and antisymmetric averages, and using the Feautrier variables, $u = \frac{1}{2}(I^+ + I^-)$ and $v = \frac{1}{2}(I^+ - I^-)$, eqs. (2.9) and (2.10) are rewritten as

$$\mu \frac{\partial v(\mu)}{\partial \tau} = u(\mu) - \frac{1}{2}\left[S^+(\mu) + S^-(\mu)\right] - S^T \tag{2.13}$$

and

$$\mu \frac{\partial u(\mu)}{\partial \tau} = v(\mu) - \frac{1}{2}\left[S^+(\mu) - S^-(\mu)\right]. \tag{2.14}$$

Since $R(\mu, \mu')$ depends only upon the angle between μ and μ', the following symmetries exist:

$$R(\mu, \mu') = R(-\mu, -\mu') \tag{2.15}$$

$$R(-\mu, \mu') = R(\mu, -\mu'). \tag{2.16}$$

With the definitions. $R^+(\mu, \mu') = R(\mu, \mu') + R(-\mu, \mu')$ and $R^-(\mu, \mu') = R(\mu, \mu') - R(-\mu, \mu')$, eqs. (2.13) and (2.14) become

$$\mu \frac{\partial v}{\partial \tau} = u - \frac{1}{2}\sigma \int_0^1 R^+(\mu, \mu') u(\mu') d\mu' - S^T \tag{2.17}$$

and

$$\mu \frac{\partial u}{\partial \tau} = v - \frac{1}{2}\sigma \int_0^1 R^-(\mu, \mu') v(\mu') d\mu'. \tag{2.18}$$

In order to test the asymmetric Feautrier code, I compared the resulting spherical albedos for uniform atmosphere models with those derived employing both Monte Carlo and analytic techniques. Van de Hulst (1974) derived a solution for the spherical albedo of a planet covered with a semi-infinite homogeneous cloud layer. Given a single-scattering albedo of σ ($= \sigma_{scat}/\sigma_{ext}$) and a scattering asymmetry factor of $g =< \cos\theta >$ (the average cosine of the scattering angle), van de Hulst's expression for the spherical albedo is

$$A_s \approx \frac{(1 - 0.139s)(1 - s)}{1 + 1.170s}, \tag{2.19}$$

where

$$s = \left[\frac{1 - \sigma}{1 - \sigma g}\right]^{1/2}. \tag{2.20}$$

Figure 2.1 shows the spherical albedo (see §7.7) of a homogeneous, semi-infinite atmosphere as a function of scattering asymmetry factor and single scattering albedo. Along with van de Hulst's semi-analytic curves are my asymmetric Feautrier results, as well as those from a Monte Carlo model (Sudarsky et al. 2000) using a Henyey-Greenstein scattering phase function,

$$p(\theta) = \frac{1 - g^2}{(1 + g^2 - 2g\cos\theta)^{3/2}}. \tag{2.21}$$

For nearly all values of g and σ, the agreement is very good, differing by under 1%. There are slightly larger variations when both g and σ approach unity due to the finite number of angles and depth zones used in our numerical models, but in actual planetary or EGP atmospheres, this corner of parameter space is rarely realized.

2.3. Discontinuous Finite Element Method

The Feautrier method is appropriate for hot EGPs at large orbital radii and isolated brown dwarfs, but when the incoming intensity at the upper boundary of an EGP overwhelms the source function by many orders of magnitude, a method that solves directly for the specific intensity appears to be numerically favorable. The discontinuous finite element (DFE) method, described by Castor et al. (1992), is quite suitable. In the present work, this is the method used for all EGP models. The technique exploits step discontinuities in the intensity at each depth zone, as is summarized below.

Unlike the Feautrier method, the DFE method treats inward- and outward-propagating rays separately. Following Castor et al. , considering a given frequency and angle, the optical depth (τ_ν) along a given ray is equal to t_ν/μ, where t_ν is the vertical optical depth. The optical depth between two discretized depth zones is assumed to be a simple linear function of optical depth. Hence (dropping the frequency subscripts for clarity),

$$I(\tau) \simeq I_d^a u_d^a(\tau) + I_{d+1}^b u_{d+1}^b(\tau), \tag{2.22}$$

where τ is within τ_d and τ_{d+1}, I_d^a represents the intensity at the top of the step discontinuity, I_d^b at the bottom, and u^a and u^b are given by

$$u_d^a(\tau) = \frac{\tau_{d+1} - \tau}{\Delta\tau_{d+1/2}} \tag{2.23}$$

and

$$u_{d+1}^b(\tau) = \frac{\tau - \tau_d}{\Delta\tau_{d+1/2}}, \tag{2.24}$$

where $\Delta\tau_{d+1/2} = \tau_{d+1} - \tau_d$. A system of equations for I_d^a and I_d^b is obtained by substituting eq. (2.22) into the transfer equation, then forming two projections by multiplying first by u_d^a, then by u_{d+1}^b. After integrating from $\tau_d - \epsilon$ to $\tau_{d+1} - \epsilon$ (because terms with δ functions arise due to the step discontinuities), taking the limit $\epsilon \to 0$, and enough algebra, the resulting equations are:

$$\frac{I_{d+1}^b + I_d^a - 2I_d^b}{\Delta\tau_{d+1/2}} = \frac{2}{3}(S_d - I_d^a) + \frac{1}{3}(S_{d+1} - I_{d+1}^b) \tag{2.25}$$

and

$$\frac{I_{d+1}^b - I_d^a}{\Delta\tau_{d+1/2}} = \frac{1}{3}(S_d - I_d^a) + \frac{2}{3}(S_{d+1} - I_{d+1}^b). \tag{2.26}$$

The $S - I$ terms of this system have the coefficients given by the matrix,

$$\begin{pmatrix} \frac{2}{3} & \frac{1}{3} \\ \frac{1}{3} & \frac{2}{3} \end{pmatrix}. \tag{2.27}$$

Castor et al. find that the numerical stability of the system is improved when this matrix is replaced by the unit matrix. So equations 2.25 and 2.26 take the simpler form,

$$\frac{I_{d+1}^b + I_d^a - 2I_d^b}{\Delta\tau_{d+1/2}} = S_d - I_d^a \tag{2.28}$$

and

$$\frac{I_{d+1}^b - I_d^a}{\Delta\tau_{d+1/2}} = S_{d+1} - I_{d+1}^b. \tag{2.29}$$

Elimination of I_d^a from equations 2.28 and 2.29 yields the relation for I_d^b:

$$(\Delta\tau_{d+1/2}^2 + 2\Delta\tau_{d+1/2} + 2)I_{d+1}^b - 2I_d^b = \Delta\tau_{d+1/2}S_d + \Delta\tau_{d+1/2}(\Delta\tau_{d+1/2} + 1)S_{d+1}, \tag{2.30}$$

and the relation for I_d^a then is

$$(\Delta\tau_{d+1/2}^2 + 2\Delta\tau_{d+1/2} + 2)I_d^a - 2(\Delta\tau_{d+1/2} + 1)I_d^b = \Delta\tau_{d+1/2}(\Delta\tau_{d+1/2} + 1)S_d - \Delta\tau_{d+1/2}S_{d+1}. \tag{2.31}$$

The final specific intensity at a given depth zone is then formed as a linear combination of I_d^a and I_d^b.

$$I_d = \frac{I_d^b \Delta\tau_{d+1/2} + I_d^a \Delta\tau_{d-1/2}}{\Delta\tau_{d+1/2} + \Delta\tau_{d-1/2}}. \tag{2.32}$$

Castor et al. show that this method results in the same order of accuracy as the Feautrier method (second order), provided that the optical depth increments vary smoothly.

As pointed out by Ivan Hubeny (private communication), one must be cognizant of the fact that the above derivation assumes that the optical depth increases along each given ray of interest. In the context of plane parallel atmospheres, where optical depth increases downward, the optical depth decreases along an outgoing ray. So equations 2.3 and 2.31 must be solved separately for the incoming and outgoing intensities. In the outgoing ray case, one may either reverse the entire grid of depth indices, or rewrite equations 2.3 and 2.31 so that the quantities at depth point $d+1$ are replaced by those at depth d, and vice-versa.

2.4. Direct Solution of the Transfer Equation

Under most circumstances, an iterative approach to solving the transfer equation is necessary because the atmospheric temperature/pressure structure is strongly coupled to the absorption and emission of radiation. However, in the rare case where a T-P profile has been obtained observationally (*e.g.* Jupiter), one may choose to solve the transfer equation directly.

Consider the system of first-order equations of the asymmetric Feautrier method (§2.2). This system is discretized for numerical computation by replacing the derivatives with difference quotients, and by substituting Gaussian quadrature sums for the integrals. The principal equations then become

$$\mu_i \frac{v_{d,i} - v_{d-1,i}}{\Delta\tau_d} = u_{d,i} - \frac{1}{2}\sigma \sum_j \omega_j R^+(\mu_i, \mu_j) u_{d,j} - S_d^T \tag{2.33}$$

and

$$\mu_i \frac{u_{d+1,i} - u_{d,i}}{\Delta\tau_{d+\frac{1}{2}}} = v_{d,i} - \frac{1}{2}\sigma \sum_j \omega_j R^-(\mu_i, \mu_j) v_{d,j} \, . \tag{2.34}$$

where d signifies a given depth zone ($d = 1, \ldots, D$), and i and j signify angular bins ($i, j = 1, \ldots, N$). $\Delta\tau_{d+\frac{1}{2}}$ equals $\tau_{d+1} - \tau_d$ and $\Delta\tau_d$ equals $\frac{1}{2}(\Delta\tau_{d+\frac{1}{2}} + \Delta\tau_{d-\frac{1}{2}})$. To achieve numerical stability, $\Delta\tau$ is staggered by half a zone in eq. (2.34) relative to eq. (2.33). The ω_j are the Gaussian weights.

The upper boundary conditions are given by the relations, $u_{1,i} - v_{1,i} = I_i^-$ and

$$\mu_i \frac{u_{2,i} - u_{1,i}}{\Delta\tau_{\frac{1}{2}}} = u_{1,i} - I_i^- - \frac{1}{2}\sigma \sum_j \omega_j \left[u_{1,j} - I_j^-\right] R^-(\mu_i, \mu_j) \, . \tag{2.35}$$

where I_i^- and I_j^- signify the incident intensity as a function of angle at the surface. The lower boundary conditions are given by $u_{D,i} + v_{D,i} = I_i^+$ and

$$\mu_i \frac{u_{D,i} - u_{D-1,i}}{\Delta\tau_{D-\frac{1}{2}}} = I_i^+ - u_{D,i} - \frac{1}{2}\sigma \sum_j \omega_j \left[I_j^+ - u_{D,j}\right] R^-(\mu_i, \mu_j) \, . \tag{2.36}$$

where I_i^+ and I_j^+ signify the outward-traveling intensity at the base of the atmosphere

The system of equations can be represented by angle matrices ($\mathbf{A}_d, \mathbf{B}_d, \mathbf{C}_d, \ldots$) and column vectors ($\mathbf{u}_d$ and $\mathbf{v}_d$) such that equations (2.33) and (2.34) can be written as

$$\mathbf{A}_d \mathbf{v}_{d-1} + \mathbf{B}_d \mathbf{u}_d + \mathbf{C}_d \mathbf{v}_d = 0 \tag{2.37}$$

and

$$\mathbf{D}_d\mathbf{u}_d + \mathbf{E}_d\mathbf{v}_d + \mathbf{F}_d\mathbf{v}_{d+1} = 0. \tag{2.38}$$

Given D depth zones and N angles, the system results in a block matrix containing $[2 \times D]^2$ submatrices, each of order N. Implementing the boundary conditions described above, this system is solved directly via LU decomposition and substitution.

2.5. Achieving Radiative Equilibrium Via Accelerated Lambda Iteration

In order for an atmosphere model to achieve convergence, it must be in radiative equilibrium. The temperature-density structure is adjusted so that at every depth zone, the net flux throughout the atmosphere is a constant determined by the inner boundary condition. Arriving at the correct structure is nontrivial given the global nature of the problem, the temperature and pressure dependences of the opacities, the onset of convective transport, etc., but the Accelerated Lambda Iteration (ALI) method of Rybicki & Hummer (1991) is an efficient iterative technique for achieving convergence. Below is a brief summary of the method used to arrive at a self-consistent atmosphere model.

Radiative equilibrium requires that the absorption and thermal emission of radiation are equal at every atmospheric depth zone. Hence,

$$\int_0^\infty (\kappa_\nu B_\nu - \kappa_\nu J\nu)\mathrm{d}\nu = 0, \tag{2.39}$$

where B is the Planck function and J is the mean intensity. Additionally, a constraint on the value of the flux itself is given by the constraint,

$$\int_0^\infty \frac{\partial K_\nu}{\partial \tau_\nu}\mathrm{d}\nu = H_0, \tag{2.40}$$

where K_ν is the second moment of the intensity and $H_0 = \sigma T_{\rm eff}^4/4\pi$ is the prescribed inner boundary flux. Rewritten in dimensionless form, and linearized with respect to temperature and density, a combination of these two constraints assures that any converged model is in radiative equilibrium.

Since the temperature and density corrections required to reach radiative equilibrium are coupled to J, an iterative procedure is required. The formal solution of the transfer equation can be written as $J = \Lambda[S]$, where S is the source function and Λ is a matrix operator (the Lambda matrix) that acts on the source function to produce the mean intensity. Unfortunately, we do not know the form of the Lambda matrix, but an approximate form, the so-called approximate Lambda matrix (Λ^*) can be derived from the matrix elements of the Feautrier or DFE schemes (Rybicki & Hummer 1991; Hubeny 1992). Λ^* is usually in the form of a diagonal matrix to treat the local coupling of the source function with intensity directly, leaving the coupling of more distant zones to the iterative process. Rewriting the full Lambda operator in terms of Λ^*, a process known as operator splitting or "the method of deferred corrections," $\Lambda = \Lambda^* + (\Lambda - \Lambda^*)$. The iterative solution to the transfer equation can then be written,

$$J^i = \Lambda^*[S^i] + J^{i-1} - \Lambda^*[S^{i-1}], \tag{2.41}$$

where J^{i-1} has been substituted for $\Lambda[S^{i-1}]$ and i refers to the iteration number. The iterative procedure for arriving at an atmosphere in radiative equilibrium first entails solving the transfer equations, given an initial model temperature-density structure, which may simply be based upon the Milne approximation for a gray atmosphere. The $J^{i-1} - \Lambda^*[S^{i-1}]$ terms are determined, and the temperature and density corrections are made in each zone, bringing the atmosphere closer to radiative equilbrium (if all goes well). Based on the updated temperature-density structure, new values for the source function and opacities are determined as functions of depth and frequency, and the $\Lambda^*[S^i]$ terms are computed. The transfer equations are solved again, and the entire process is repeated. The iterative temperature and density corrections result in a diminution of the difference between the $\Lambda^*[S^i]$ and $\Lambda^*[S^{i-1}]$ terms until, ultimately, the difference approaches zero.

In regions of high opacity, where radiative transport is insufficient for the transport of energy, a steep temperature gradient results in convection. As in most atmospheric modeling, a simple mixing-length treatment of convection is utilized in the present work. Such a treatment assumes that the convective elements are rising and falling bubbles. This convective flux (see below) must be taken into account so that the sum of the radiative and convective fluxes (the true total net flux) in each zone throughout the atmosphere is constant.

Generally, convection does not occur in the thin outer atmosphere, but deeper down at high pressure. Specifically, a region will be convective if the actual temperature gradient is of greater magnitude than the adiabatic gradient, which is the change in temperature with respect to pressure that an outward moving bubble would follow under the condition of no radiative losses. As described in detail in Kurucz (1970), the convective flux is given by

$$F_{conv} = \frac{1}{2}\left(\frac{l}{h}\right)\rho c_p T v_{conv}\left[\left(\frac{\mathrm{d}\ \ln T}{\mathrm{d}\ \ln P}\right)_{actual} - \left(\frac{\mathrm{d}\ \ln T}{\mathrm{d}\ \ln P}\right)_{bubble}\right]. \tag{2.42}$$

where (l/h), the ratio of the mixing length to the pressure scale height, is the mixing length parameter (set to unity for my fiducial models), c_p is the specific heat at constant pressure, and v_{conv} is the convective velocity.

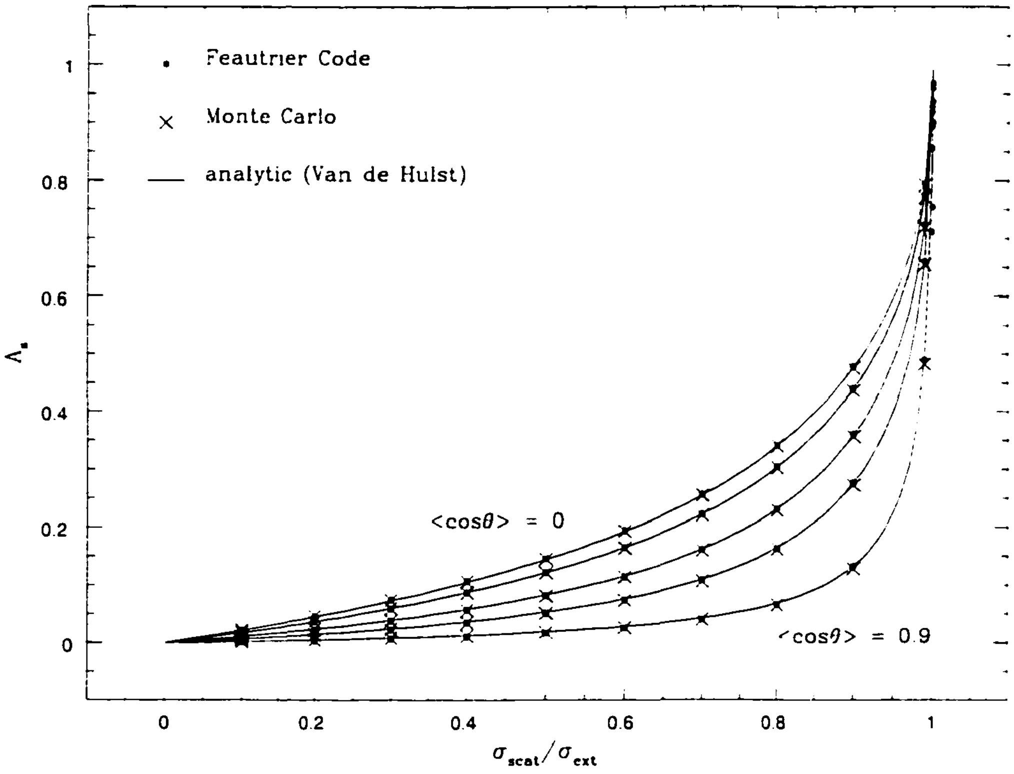

Figure 2.1 Comparison of Asymmetric Feautrier code results to Monte Carlo and analytic solutions for deep, homogeneous atmosphere. The spherical albedo is plotted as a function of the single-scattering albedo ($= \sigma_{scat}/\sigma_{ext}$) and the average value of the cosine of the scattering angle ($g = < \cos\theta >$).

3 ATMOSPHERIC COMPOSITION

The emergent spectra of EGPs are determined mainly by their outer atmospheric chemical compositions. But unlike stars, whose atmospheres are dominated by gaseous species (grain formation occurs only in the coolest M dwarfs) most EGPs also contain condensed species that contribute substantially to the opacities. Some condensates, such as water ice or iron grains, are formed homogeneously (i.e. from a single species), while the formation of others such as forsterite or gehlenite is heterogeneous, resulting in the depletion of several gas-phase species. The largely unknown meteorology in EGP atmospheres and condensate sedimentation, or "rain-out," makes the depth-dependent composition modeling of EGPs a difficult task.

Any method useful in determining compositions of EGP atmospheres must be capable of treating the gaseous, liquid, and solid phase species simultaneously. Additionally, the rain-out of species must be handled appropriately, because the removal of a given species to deeper layers by such sedimentation can alter chemical reactions drastically. I use results from the chemical equilibrium code of Burrows and Sharp (1999), which includes a prescription to account for the rain-out of species in a gravitational field. My fiducial models assume an Anders and Grevesse (1989) solar composition of 27 elements (H, He, Li, C, N, O, F, Ne, Na, Mg, Al, Si, P, S, Cl, Ar, K, Ca, Ti, V, Cr, Mn, Fe, Co, Ni, Rb, Cs), resulting in approximately

300 molecular gas-phase species and over 100 condensates. From this large set of species, only some have the requisite abundances to have significant effects on the emergent spectra and/or temperature-pressure (T-P) structure.

3.1. Chemical Abundances in EGPs and Brown Dwarfs

The equilibrium gas-phase and condensed-phase abundances of species at a given pressure, temperature, and elemental composition are obtained by minimizing the total free energy of the system (Burrows & Sharp 1999). The abundances of most species are highly dependent on temperature, as well as moderately dependent on pressure. As an example, consider the balance of CO and methane, the dominant equilibrium forms of carbon, which are governed by the reaction,

$$CO + 3H_2 \longleftrightarrow H_2O + CH_4. \tag{3.1}$$

For exothermic reactions, such as this one, an increase in temperature at a given pressure favors the reactants, so equilibrium favors CO over CH_4 with increasing temperature. But at increased pressure (for a fixed temperature), the side of the reaction with less molecules is favored (Le Chatelier's Principle), which results in a greater CH_4 abundance at the expense of CO. The analogous reaction that governs N_2 and NH_3 abundances, the dominant equilibrium forms of nitrogen, is

$$N_2 + 3H_2 \longleftrightarrow 2NH_3. \tag{3.2}$$

So at high temperatures, N_2 is favored, but the equilibrium shifts toward NH_3 with increasing pressure. Figure 3.1 depicts the equal abundance boundaries for CO-CH_4 and for N_2-NH_3 in temperature-pressure space. Upward and to the right of these curves in T-P space, the abundances move strongly in favor of N_2 and CO, and downward and to the left in favor of NH_3 and CH_4.

At the temperatures and pressures of brown dwarfs and EGPs. H_2O is the main reservoir of oxygen and is the third most abundant species, behind H_2 and He. The H_2O abundance is reduced somewhat at high atmospheric temperatures because CO competes for oxygen (Eq. 3.1) and because silicates form.

TiO and VO, important molecular species in the atmospheres of M dwarfs, form at temperatures greater than ~1700-2000 K in brown dwarf atmospheres, as do CrH and FeH. The alkali metals persist to much lower temperatures (~ 1000 K), and sodium and potassium are particularly important both in brown dwarfs and the hotter of the EGP classes. Lithium, rubidium, and cesium are present as well, albeit in lower abundance. Sulfur appears in the form of H_2S at low-to-moderate abundance over a large range in temperature and pressure, while phosphorous is in the form of PH_3.

3.2. Composition Profiles

The pressure and temperature dependences of the gas-phase abundances become clear upon examination of the number fractions of major species in the atmosphere of an EGP or brown dwarf. Figure 3.2 is a plot of a number of gas-phase mixing ratios as a function of atmospheric pressure for an EGP in close orbit around its primary, while Figure 3.3 depicts these abundances for an isolated brown dwarf of similar temperature, $T_{\rm eff} = 1000$ K.

With a mixing ratio of $\sim 10^{-3}$, H_2O is the 3rd most abundant species (trailing only H_2 and He) in both the EGP and brown dwarf atmospheres. Water is the dominant carrier of oxygen for the full range of pressures. The H_2 mixing ratio (not shown in the figure) for the EGP and the brown dwarf is near 0.83 throughout their atmospheres, dropping off slightly at depth, while that of He remains close to

0.16 (also not shown).

In the brown dwarf, CH_4 is clearly the primary carrier of carbon in the outer atmosphere, but a transition to the dominance of CO at depth occurs at just under 1 bar. This can be contrasted with the EGP atmosphere, where CO is dominant at very low pressures (~ 1 microbar) and at pressures greater than ~ 3 millibars, though between these regions the methane abundance is actually greater. This competition for carbon is explained by both the temperature and the pressure dependence of the equilibrium abundances, as discussed in the previous section. At high temperatures and at low pressures, carbon is favored, and at a given pressure the outer atmosphere of the EGP is hotter than that of the brown dwarf due to irradiation by its primary. Hence, the CO abundance is greater. Deep in the atmosphere, at very high temperature, the CO abundances of the EGP and brown dwarf are quite similar, as expected.

The N_2 to NH_3 ratio varies far less than that of CO to CH_4 in these objects, because N_2 takes up most of the nitrogen at a much lower temperatures than CO takes up carbon. For lower temperature EGPs and brown dwarfs, the story is different, but for these objects, N_2 dominates at all pressures.

Although their abundances are quite low, sodium and potassium are strong absorbers in the visible region of the spectrum. For both the EGP and the brown dwarf, the Na and K abundances are negligible in the outermost atmosphere, but at depths of a few tenths of a bar in pressure, the mixing ratios of both rise rapidly in the EGP. This occurs at deeper pressures (~ 1 bar) in the brown dwarf. Again, the difference is due to the fact that the atmosphere of the EGP is hotter at low pressures than that of the brown dwarf. For those EGPs that orbit their stars most closely (~ 0.05 AU), the alkali metal abundances become significant at even lower pressures.

The abundances of cool EGPs are far different than those of the hot. close-in objects. Figure 3.4 is a plot of a number of gas-phase mixing ratios as a function of atmospheric pressure for a cool EGP ($T_{eq} \sim 200$ K). CH_4, H_2O ($\gtrsim 1$ bar), and NH_3 abundances are high and nearly constant, while CO and N_2 abundances are very low throughout the atmosphere. The alkali metals are altogether absent. Note that the temperature is low enough in the outer atmosphere of a distant/old EGP for water to condense, which explains the drop in its gas-phase abundance for pressures under ~ 1 bar, as seen in Figure 3.4.

3.3. Condensation and Rainout

The condensation and gravitational settling of species results in compositions that differ significantly from those of a true equilibrium scenario. Condensation sequesters most of the heavier elements, such as silicon, magnesium, calcium, aluminum, and iron, in compounds that settle, or rain out, leaving the upper atmosphere depleted of species that would otherwise contribute to the molecular chemistry. Condensates are very important in their own right as well, often providing substantial absorption and scattering opacity in the visible and infrared spectral regions (see §5.4).

Some of the more refractory species expected to exist in EGP (and brown dwarf) atmospheres are calcium-aluminum compounds, such as $Ca_2Al_2SiO_7$ (gehlenite), and aluminum oxides, such as Al_2O_3 (corundum). Since both calcium and aluminum are less abundant than silicon or oxygen, the formation and gravitational settling of these condensates should consume most of the calcium and aluminum, thereby depleting the upper atmosphere of these metals. The atmospheric temperature and pressure at which this occurs depends on the details of the particular T-P profile. For a given mass, the T-P profile of an irradiated object (vs. an isolated object) will tend to intersect with the condensation curve of the refractory species at a lower temperature and pressure, so the condensate will settle higher (at lower pressure) in the atmosphere.

Another refractory species, TiO, can condense into the calcium titanates ($Ca_3Ti_2O_7$, $Ca_4Ti_3O_{10}$: Lodders 2002) and/or into titanium oxides (Ti_2O_3, Ti_3O_5, Ti_4O_7) in EGP atmospheres. Iron is expected to condense mainly in a homogeneous manner rather than as FeS or some other heterogeneous species, because the condensation temperature for pure iron is quite high (~1500-2300 K, depending significantly on pressure). In contrast, the homogeneous condensation of VO is unlikely because vanadium condenses into solid solution with titanium-bearing condensates (Lodders 2002).

The silicates are somewhat less refractory, so in general, they will appear higher in the atmosphere (*i.e.* at lower temperature and pressure). The exact composition of the silicates is unknown, although some common species include $MgSiO_3$ (enstatite) and Mg_2SiO_4 (forsterite). Of these two possibilites, forsterite is more likely to exist in EGP and brown dwarf atmospheres because it has a higher condensation temperature and so will consume most of the magnesium, the limiting element. And although Mg_2AlO_4 (magnesium-aluminum spinel) condenses at even higher temperatures, it is unlikely to form in abundance because most of the aluminum will be consumed by the formation of corundum and/or other aluminum compounds. In brown dwarf and giant planet atmospheres, forsterite will condense within the ~ 1500-2000 K range, depending upon atmospheric pressure. I should mention that forsterite and enstatite are only two species in the olivine ($Mg_xFe_{1-x}SiO_3$) and pyroxene ($Mg_{2x}Fe_{2-2x}SiO_4$) sequences, respectively. The optical properties of other such species have been explored by Dorschner et al. (1995). If iron has not been fully removed by homogeneous condensation and rain out—and it is unlikely that homogeneous condensation will consume all the iron—then some of these iron-bearing species are likely to form.

At cooler temperatures (~700-1100 K), sulfide and chloride condensates are expected to sequester the alkali metals. Sodium will end up in Na_2S and/or NaCl (Lodders 1999), while potassium is likely to be in the form of KCl. Due to the low abundances of the alkalis, thick clouds are unlikely, but "cirrus-like" layers are certainly possible.

At lower temperatures, H_2O will condense homogeneously for atmospheric temperatures below ~ 200-250 K. Hence, many EGPs at large orbital distances will contain water clouds, as will cool brown dwarfs. Even if only a small fraction of H_2O condenses, as governed by the degree of supersaturation (Cooper et al. 2002), the high abundance of H_2O and its large reflectivity in ice or liquid form indicates that condensed H_2O is important to the emergent spectra of EGPs.

At very low temperatures (~ 150-200 K), NH_3 and NH_4SH condense. NH_4SH condenses at somewhat higher temperatures than ammonia, so a layer of this heterogeneous material is expected to appear between a water cloud and an ammonia cloud in cold EGPs. Such is the case for the standard model of Jupiter (see §7.7). However, I do not model an NH_4SH layer because the optical constants for this material over a broad wavelength range are not available.

3.4. Gravitational Settling Versus True Equilibrium

The presence of a gravitational field affects the abundances (or even the very existence) of several species relative to that of a true equilibrium scenario. The removal of condensates by gravitational settling, or rain-out, after their formation results in a different equilibrium than the true equilibrium case, where the condensates would continue to react chemically with the gas-phase species.

Importantly, the alkali metal abundances are higher in a rain-out scenario than they are in the true equilibrium case. In the true equilibrium case, $NaAlSi_3O_8$ (high albite) and $KAlSi_3O_8$ (high sanidine) can condense, lowering the gas-phase abundance of sodium and potassium (Burrows & Sharp 1999). But in the more realistic rain-out scenario, the aluminum is consumed by other species that condense at higher temperature, such as $Ca_2Al_2SiO_7$ (gehlenite). Gravitational settling then removes the aluminum from the upper atmosphere, thereby inhibiting the formation of sodium- and potassium-bearing condensates.

Another important species, iron condenses and settles gravitationally. This prevents the formation of FeS, which would otherwise form at low temperature. As a result, sulfur is mainly in the form of H_2S for most EGPs and brown dwarfs, although NH_4SH can form in the outer atmospheres of low-temperature objects.

The abundances of many other condensates and gas-phase species under a true equilibrium scenario are discussed by Burrows and Sharp (1999). In this work, I assume their rain-out abundances for my entire model set, since this approach is most realistic.

3.5. Photoionization of Alkali Metals

In the outer atmosphere of a close-in EGP, ultraviolet irradiation from the central star will photoionize any species with a sufficiently low ionization threshold. Most notable are the alkali metals, sodium and potassium. When in their neutral form, the resonance lines of these metals can result in deep, broad optical absorption (Burrows et al. 2000; Tsuji et al. 1999; Sudarsky et al. 2000). Such strong absorption may be reduced if the outer atmospheric sodium and potassium atoms are substantially ionized, an effect that will be particularly important in the case of the transit radius or transmission spectrum (Seager & Sasselov 2000) of a Class V EGP that transits its primary, such as the HD 209458 system. The depth in the atmosphere to which ionization occurs depends on several variables, including the amount of ultraviolet stellar flux, the star-planet distance, the planet's gravity, its composition, and the presence of high clouds or non-equilibrium species that can absorb ultraviolet radiation. An approximate calculation of the ionization depth at the subsolar point in the planet's atmosphere is straightforward, as this is simply the planar analog to an H II region.

Let us consider the ionization of sodium gas in the outer atmosphere of an EGP. The number of ionizing photons per second per unit area at the planet's orbital distance is given by

$$N = \frac{1}{4\pi a^2} \int_{\nu_1}^{\nu_2} \frac{L_\nu \mathrm{d}\nu}{h\nu}, \tag{3.3}$$

where L_ν is the stellar luminosity per unit frequency interval, a is the orbital distance of the planet, ν_1 is the ionization threshold frequency of sodium (from its ground state), and ν_2 is the frequency above which ultraviolet photons are no longer transparent to H_2 or other abundant species capable of absorbing high-energy photons (thereby shielding the neutral sodium at higher frequencies).

In equilibrium, the number of ionizations per second, per unit volume must equal the number of recombinations. Assuming that two-body radiative recombinations dominate,

$$\mathcal{N} = \int_0^l n_i(l) n_e(l) \alpha(T(l)) \mathrm{d}l, \tag{3.4}$$

where l is the depth (in units of length) measured from the top of the gaseous planetary atmosphere, n_i is the number density of sodium ions, n_e is the number density of electrons, and $\alpha(T(l))$ is the volume recombination coefficient. Using hydrostatic equilibrium and the ideal gas law, Eq. (3.4) is rewritten as

$$\mathcal{N} = \frac{1}{kg} \int_0^P T\alpha(T(P)) f(P)^2 (n_e/n_i) \mu(P)^{-1} P \mathrm{d}P, \tag{3.5}$$

where P is the atmospheric pressure, g is the surface gravity, $f(P)$ is the mixing ratio of sodium atoms, k is Boltzmann's constant, and $\mu(P)$ is the mean molecular weight. The ratio of free electrons to sodium ions, (n_e/n_i), will be a function of pressure depth if free electrons originate from species other than sodium, such as potassium or H_2. For a simple back-of-the-envelope calculation, one can assume that $(n_e/n_i) = 1$ and ignore the pressure and temperature dependences of the other variables to obtain:

$$P \sim \left[\frac{2kTg\mu\mathcal{N}}{\alpha f^2} \right]^{1/2}. \tag{3.6}$$

For $T = 1000$ K, $f = 3 \times 10^{-6}$, $\alpha = 1.3 \times 10^{-12}$ cm^3 s^{-1} (Verner & Ferland 1996), and $\mathcal{N} = 3 \times 10^{17}$ ionizing photons cm^{-2} s^{-1}, $P \approx 5$ mbar. Such an analytic calculation is of limited use for an actual EGP atmosphere calculation, mainly because the volume recombination coefficient and mixing ratio of sodium are strong functions of atmospheric depth.

In a more rigorous approach, I make use of both two- and three-body recombination processes, because at ion concentrations in the 10^{10} - 10^{12} cm^{-3} range and above, three body recombinations can be significant (Motley & Jassby

1970). I use the temperature-dependent two-body recombination rates of Verner & Ferland (1996) and the three-body rates from Gudzenko et al. (1974). With the addition of three-body recombinations, Eq. (3.4) is augmented:

$$N = \int_0^l \left[n_i(l)n_e(l)\alpha(T(l)) + n_i(l)n_e(l)^2\beta(T(l))\right] \mathrm{d}l. \tag{3.7}$$

The three-body recombination coefficient, $\beta(T(l))$, is a rather steep function of temperature, scaling roughly as $T^{-9/2}$ (Gudzenko et al. 1974). Rewriting this equation in a fashion similar to Eq. (3.5) yields

$$N = \int_0^P \left[\frac{T(P)\alpha(T(P))f(P)^2(n_e/n_i)P}{kg\mu(P)} + \frac{T(P)^{-2}\beta(T(P))f(P)^3(n_e/n_i)^2P^2}{k^2g\mu(P)}\right] \mathrm{d}P. \tag{3.8}$$

Clearly, the pressure depth of ionization will be a function of angle in the planetary atmosphere, with the night side remaining largely un-ionized except along some of the limb. The integrals of Eq. (3.8) can be calculated numerically in spherical geometry by using an additional factor of $(r^2 - R^2\cos^2\theta)^{-1/2}r$ along with a change of the independent variable from P to r, the distance from the center of the planet. R is the radius of the planet, and θ is the angle of incidence of the ionizing radiation relative to the normal at the planet's "surface" (at R). Figure (3.5) shows the results of a numerical calculation for the ionization of sodium in the atmosphere of a close-in Class IV "roaster" as a function of angle from the subsolar point (ϕ, the central angle). Note that the limb of the planet is ionized to several degrees on the night side. This particular calculation ignored the free electrons produced by potassium and molecular hydrogen. A Kurucz model stellar spectrum (Kurucz 1994) was scaled to simulate the incident flux from a G0V star at 0.045 AU, and I set ν_2 to 2.708×10^{15} Hz, the frequency below which H_2 essentially is transparent to ultraviolet radiation (Draine 2000).

In fact, in a recent theoretical study of the transit radius of HD 209458b

(Fortney et al. 2002), the above calculation is used as a guide to the ionization depth of sodium in the planet's atmosphere. To lowest order, the observations of HD 209458b in the vicinity of the sodium resonance doublet (Charbonneau et al. 2002) can be reproduced with this ionization model. It should be noted, however, that other recombination processes, such as charge transfer-reactions (Plane 1991; Helmer & Plane 1992), may be at least as important as the recombination rates used above. In §8.5, I explore the effects of alkali photoionization on the emergent spectra of close-in EGPs.

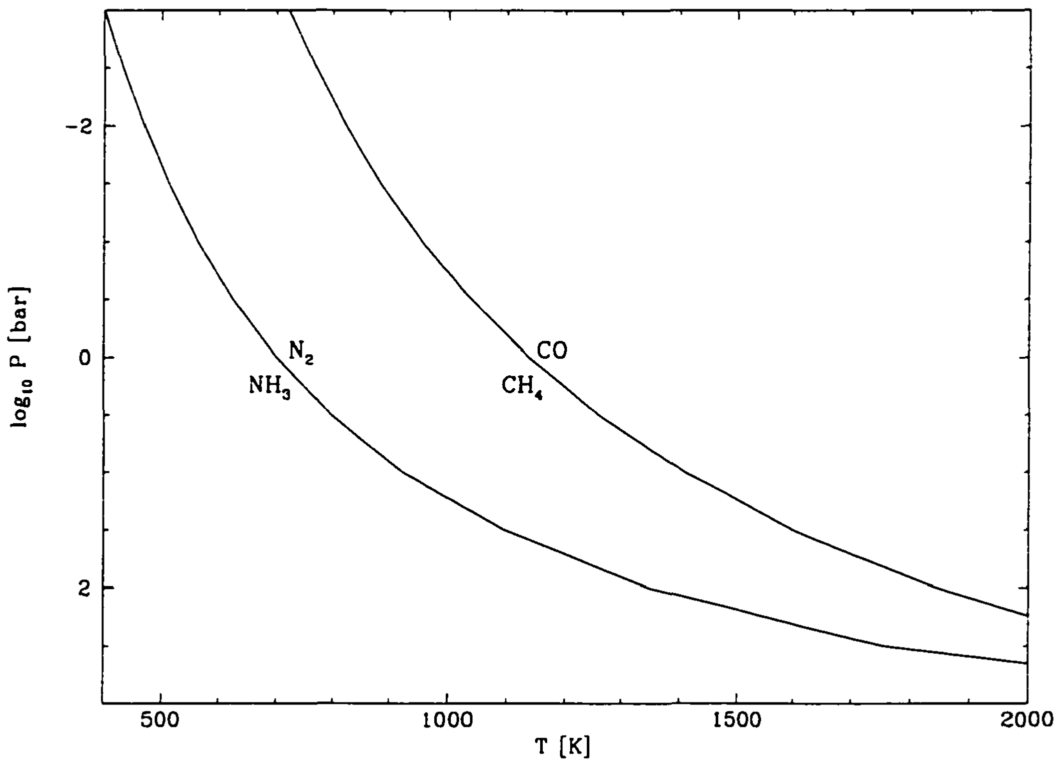

Figure 3.1 Equal abundance boundaries for CO-CH_4 and for N_2-NH_3 in temperature-pressure space. Upward and to the right of these curves in T-P space, the abundances move strongly in favor of N_2 and CO, and downward and to the left in favor of NH_3 and CH_4.

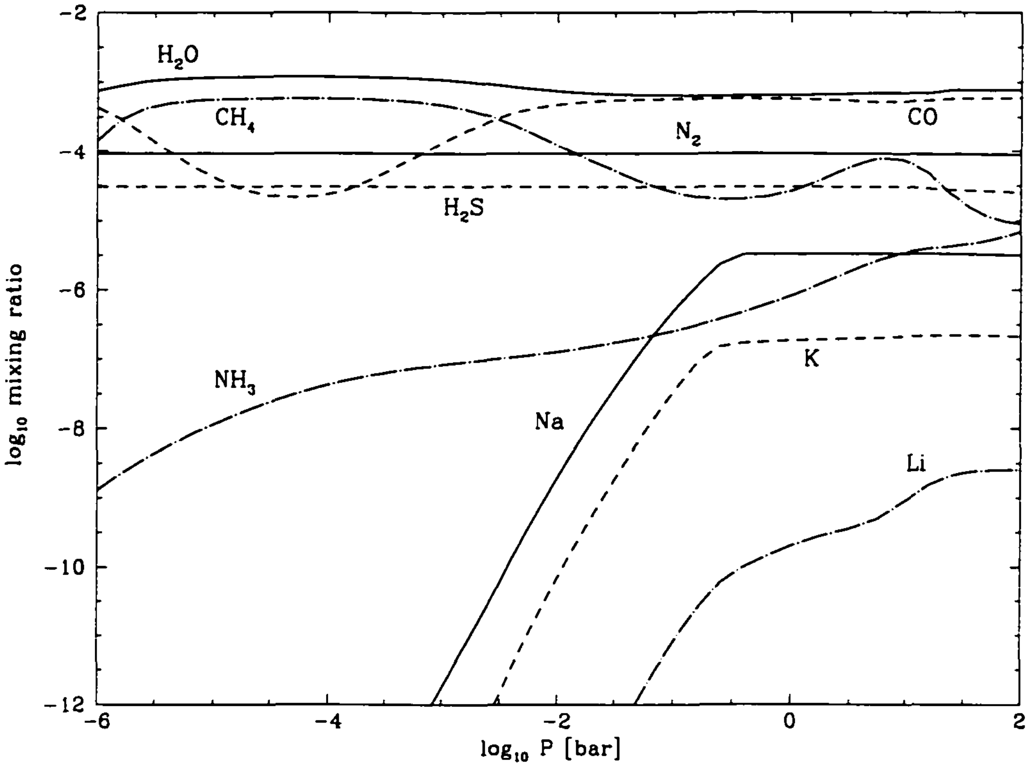

Figure 3.2 Plot of gas-phase number fractions in the atmosphere of a close-in EGP (55 Cancri b). Due to the scale of the plot, H_2 (~ 0.83) and helium (~ 0.16) are not shown.

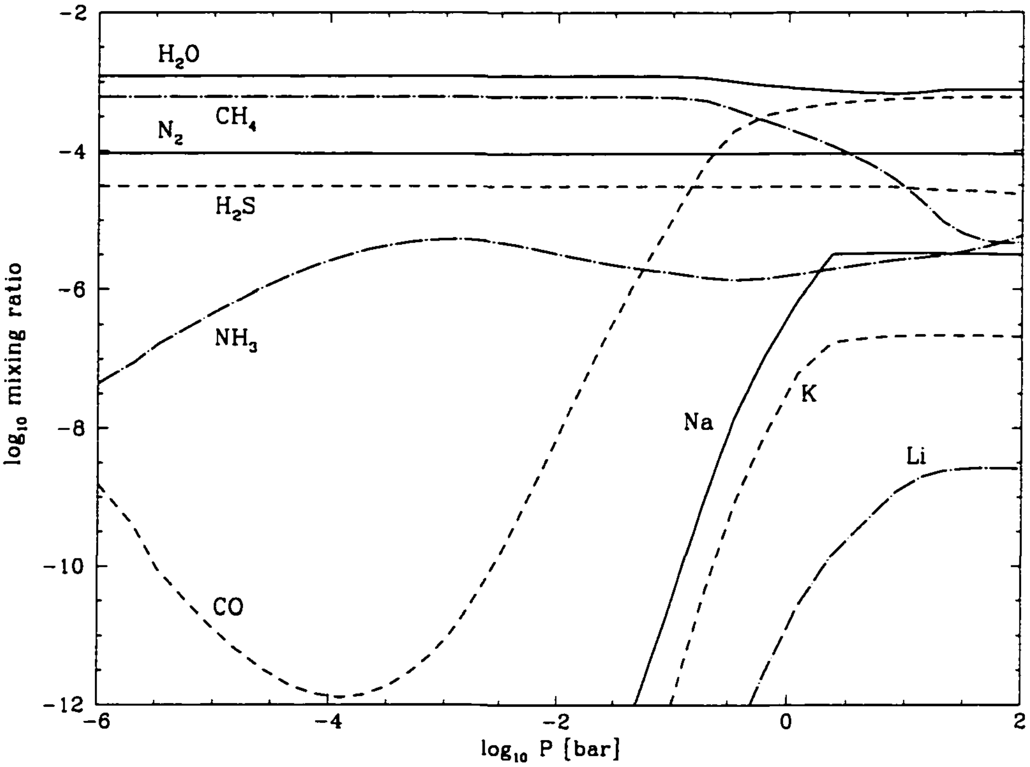

Figure 3.3 Plot of gas-phase number fractions in the atmosphere of a brown dwarf with T_{eff}= 1000 K. Due to the scale of the plot, H_2 (~ 0.83) and helium (~ 0.16) are not shown.

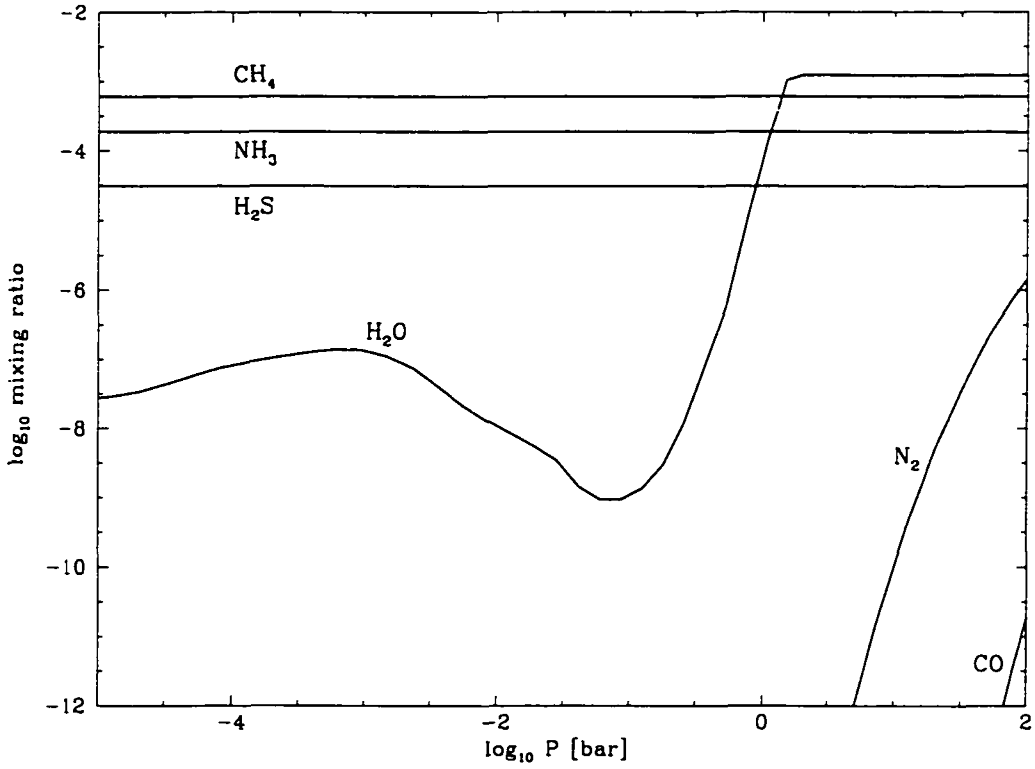

Figure 3.4 Plot of gas-phase number fractions in the atmosphere of a cool EGP (Teq ~ 200 K). Due to the scale of the plot, H_2 (~ 0.83) and helium (~ 0.16) are not shown.

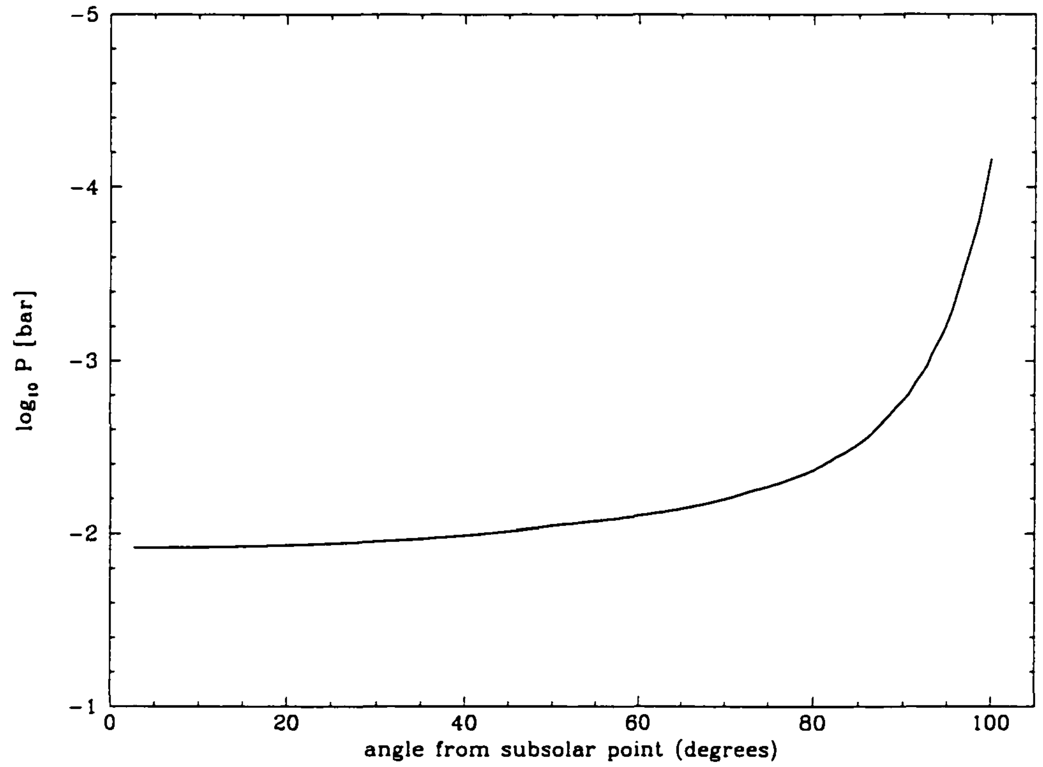

Figure 3.5 Pressure depth of sodium ionization versus angle from the substellar point in the atmosphere of a close-in EGP. A planet in a 0.045 AU orbit around a G0V star (a scaled Kurucz model) was assumed. See text for details.

4 ATOMIC AND MOLECULAR SCATTERING AND ABSORPTION

Gaseous opacities are primarily responsible in the formation of EGP and brown dwarf spectra. Unlike most stars, where H^- opacity, electron scattering, and/or a relative lack of molecular species results in a reasonably smooth continuum interspersed with many atomic lines, large scale variations with wavelength (due to molecular bands) are seen in the spectra of brown dwarfs and are expected in most EGPs as well. Even though the atmospheres of these gas giants are composed mainly of hydrogen (H_2) and helium, the $\sim$ few percent of heavier elements produce the largest effects.

4.1. Molecular Absorption

In the visible and infrared, molecular absorption is due mainly to ro-vibrational transitions, which are a very strong function of wavelength. My temperature- and pressure- dependent gaseous opacities are obtained from a variety of sources, a combination of theoretical and experimental data as referenced in Burrows et al. (1997). Additionally, for this study, the CH_4 opacity was extended continuously into the visible wavelength region using the data of Strong et al. (1993) and a methane absorption spectrum from Karkoschka (1994). These two data sets were then extrapolated in temperature and pressure by scaling with existing temperature and pressure dependent near-infrared CH_4 data (Burrows et al. 1997 and references therein).

Gas-phase molecular species common in the atmospheres of EGPs and brown dwarfs include H_2, H_2O, CH_4, CO, N_2, NH_3, H_2S, PH_3, TiO, VO, CrH, FeH, and some lower abundance molecules. Figures 4.1 and 4.2 portray some molecular opacities of particular importance to EGP atmospheres. At a temperature of 1600 K and pressure of 1 bar, Figure 4.1 depicts the opacities in cm^2 per molecule for water, methane, and CO. At this same pressure and a temperature of 200 K, a regime relevant to cool EGPs, Figure 4.2 shows the opacities for water, methane, and ammonia. Clearly, these species can be important opacity sources over a broad range of wavelengths. (Note that ammonia can absorb at visible wavelengths as well, but these opacities are not present in the available ammonia database. However, water and methane are more optically active in the visible.) Figures 4.3 and 4.4, analogous to Figures 4.3 and 4.4, show the opacities further into the infrared, out to 30 μm.

Even when no permanent dipole moment exists, such as with the H_2 molecule, high gas pressures in EGP atmospheres can induce temporary dipole moments via collisions. This Collision Induced Absorption (CIA) is responsible for broad H_2-H_2 (and H_2-He) absorption bands in the gas giants of our Solar System (Zheng & Borysow 1995; Trafton 1967), likely to exist in many EGPs as well. CIA should be especially important in cloud-free gaseous objects, where incident radiation is absorbed deep in the atmosphere at many wavelengths. Figure 4.5 shows the H_2-H_2 CIA opacity as a function of wavelength for a variety of temperatures and pressures. At relatively low temperatures, broad H_2-H_2 CIA bands peak at $\sim$ 0.8, 1.2, 2.4, and 15 μm. At higher temperatures, the CIA opacity becomes somewhat more uniform with wavelength. As pressure increases, the cross section per molecule increases at all wavelengths.

4.2. Atomic Species

Important atomic species include He, Li, Na, K, Rb, and Cs. Most other elements either form into gas- or solid-phase molecules or are too low in abundance to have significant effects on the T-P structure or emergent spectra. As a noble gas, helium contributes to the opacity only via H_2-He CIA, but the story with the alkali metals is far different. Strong pressure-broadened lines of neutral sodium and potassium are expected to dominate the visible spectra of the close-in Class IV and V EGPs. Figure 4.6 depicts the LTE (local thermodynamic equilibrium) absorption cross sections per atom of Na, K, Li, Rb, and Cs. The prominent resonance doublet of sodium appears at 5890/5896 Å, while that of potassium occurs at 7665/7699 Å. Due to their lower abundances, Li, Rb, and Cs will not have nearly the effect on the emergent spectra of EGPs as Na and K, but as in brown dwarfs, their lines will be present.

4.3. Total Gaseous Absorption Opacities

The total gaseous absorption opacities are calculated by weighting the atomic and molecular opacity of each species by its equilibrium abundance, all as a function of temperature and pressure. The resulting product is a large opacity table within which interpolation can yield the frequency-dependent total opacity at any point in the EGP or brown dwarf atmosphere.

Because both the gaseous abundances and their opacities can vary substantially with temperature and pressure, the spectral region that dominates the opacity will differ for objects of different temperature. As an illustration of this fact, Figure 4.7

shows the P = 1 bar total gas opacity for two very different temperatures, 200 K and 1600 K. For a hot atmosphere, the visible region is overwhelmed by the sodium and potassium resonance lines, yet for a cool atmosphere, the visible is canvassed by weaker methane absorption. These visible opacities (in $\mathrm{cm}^2\ \mathrm{gram}^{-1}$) differ by up to several orders of magnitude, but there are regions in the infrared where the opacity of the cool atmosphere is greater than that of the hot atmosphere, due mainly to methane and ammonia.

Such differences in the dominant opacity regions are often true of a single object at various atmospheric depths. That is, the outgoing flux at depth may escape through certain opacity windows that are closed off higher in the atmosphere, at lower pressure and temperature. Coherence in frequency will be lost upon absorption and re-emission, and the bulk of the outgoing flux ultimately will find its way out of the object between the peaks in opacity.

4.4. Rayleigh Scattering

Rayleigh scattering is a conservative scattering process by atoms and molecules. Although strong in the ultraviolet/blue, the scattering cross sections quickly fade toward the red region of the spectrum ($\propto \lambda^{-4}$). Rayleigh scattering has little effect on the spectra of isolated brown dwarfs, but irradiated EGPs reflect a fraction of the incident intensity in the ultraviolet/blue. (See §8.1 for a study of this effect.)

The Rayleigh scattering cross sections are derived from polarizabilities, which are in turn derived from refractive indices. The refractive indices are readily available at 5893 Å (Weast 1983) and are assumed not to vary strongly with wavelength. The Rayleigh cross sections are derived via,

$$\sigma_{Ray} = \frac{8}{3}\pi k^4 \left(\frac{n-1}{2\pi L_0}\right)^2 . \tag{4.1}$$

where k is the wavenumber $(2\pi/\lambda)$ and L_0 is Loschmidt's number, the number of molecules per cubic centimeter at STP $(= 2.687\times10^{19})$.

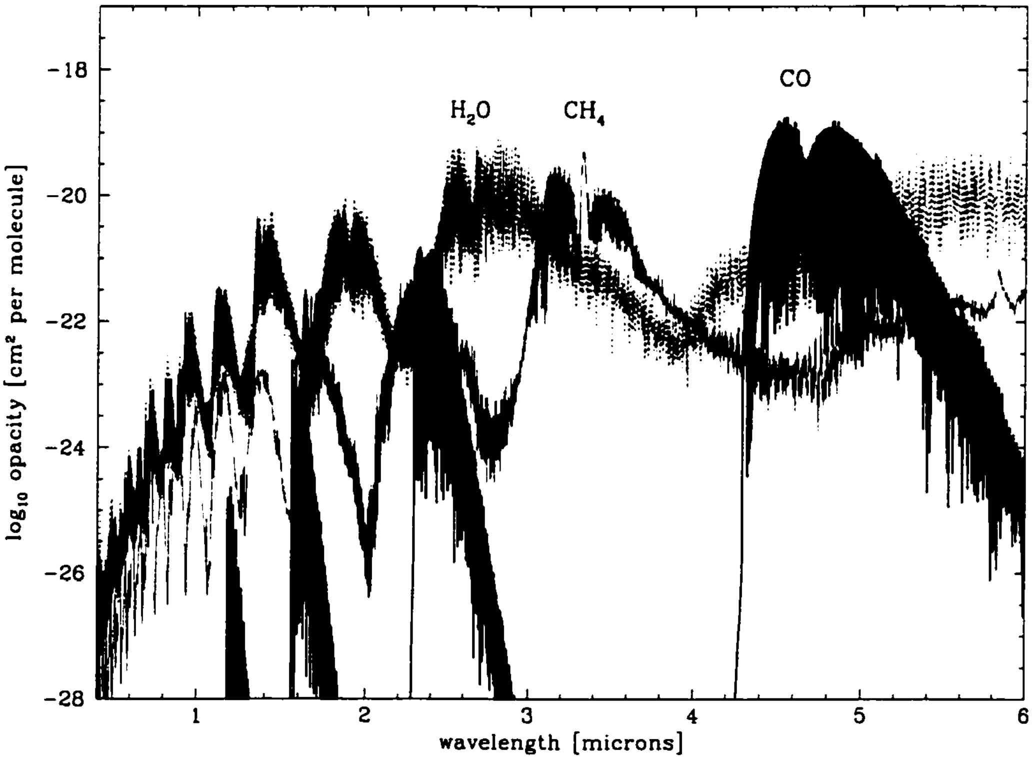

Figure 4.1 Water, methane, and CO absorption cross sections at T = 1600 K, P = 1 bar. Note that these opacities have not been weighted by the molecular abundances.

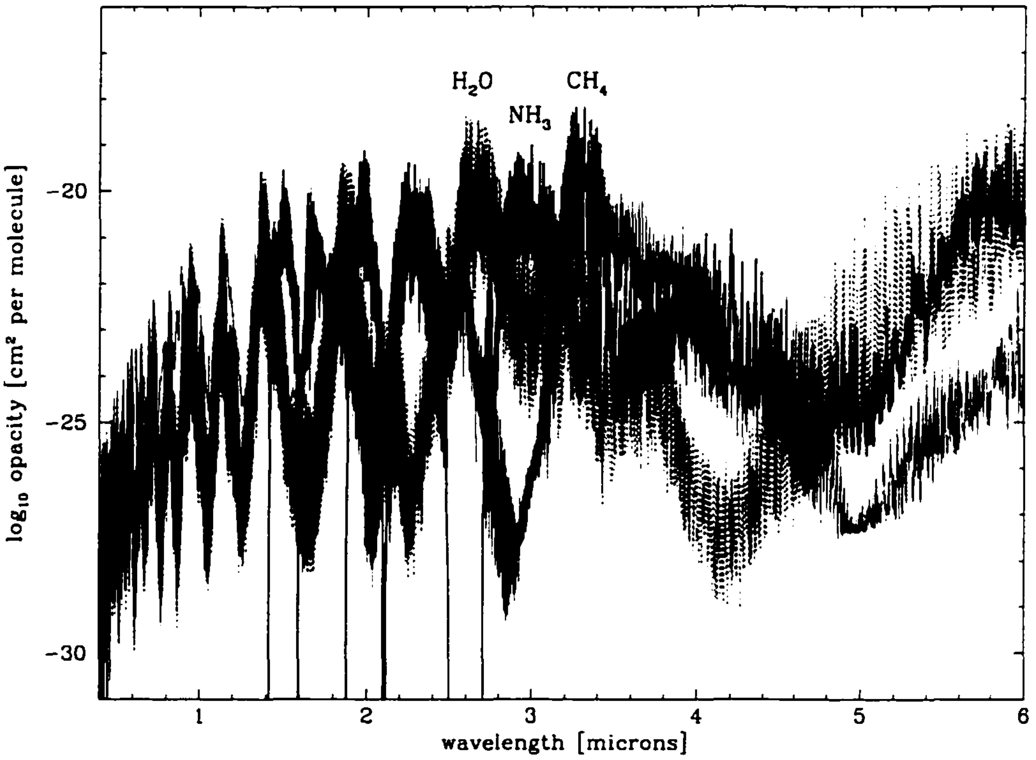

Figure 4.2 Water, methane, and ammonia absorption cross sections at T = 200 K, P = 1 bar. Note that these opacities have not been weighted by the molecular abundances.

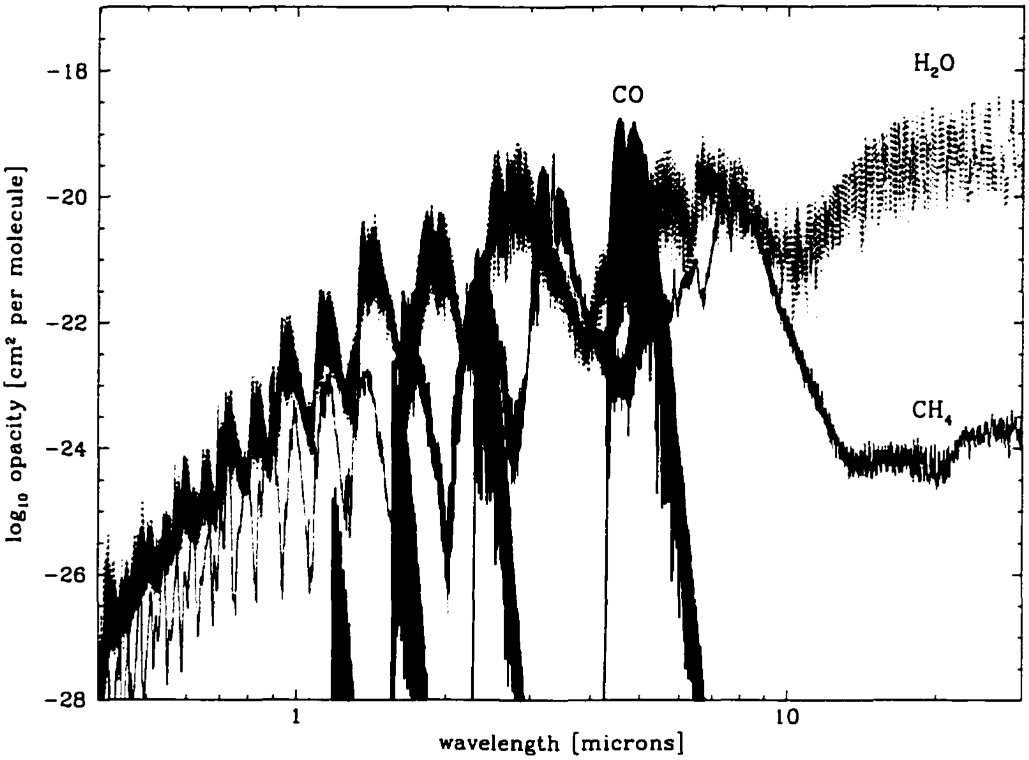

Figure 4.3 Water, methane, and CO absorption cross sections at T = 1600 K, P = 1 bar (out to 30 μm). This plot is an extended version of Figure 4.1.

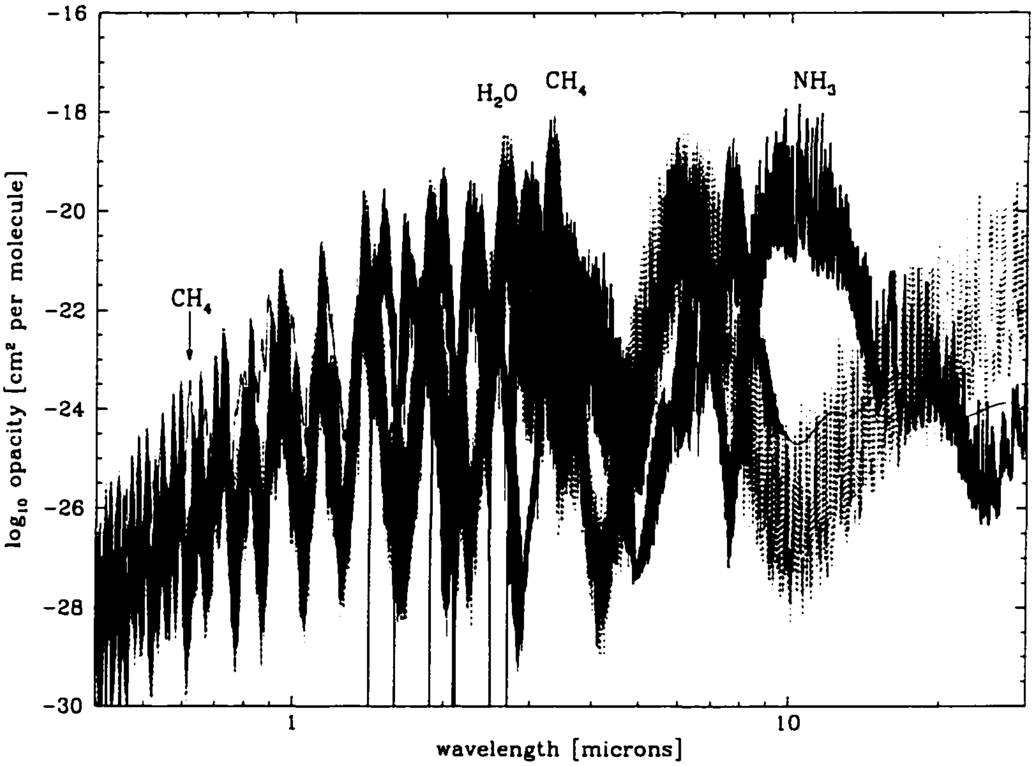

Figure 4.4 Water, methane, and ammonia absorption cross sections at T = 200 K, P = 1 bar (out to 30 μm). This plot is an extended version of Figure 4.2.

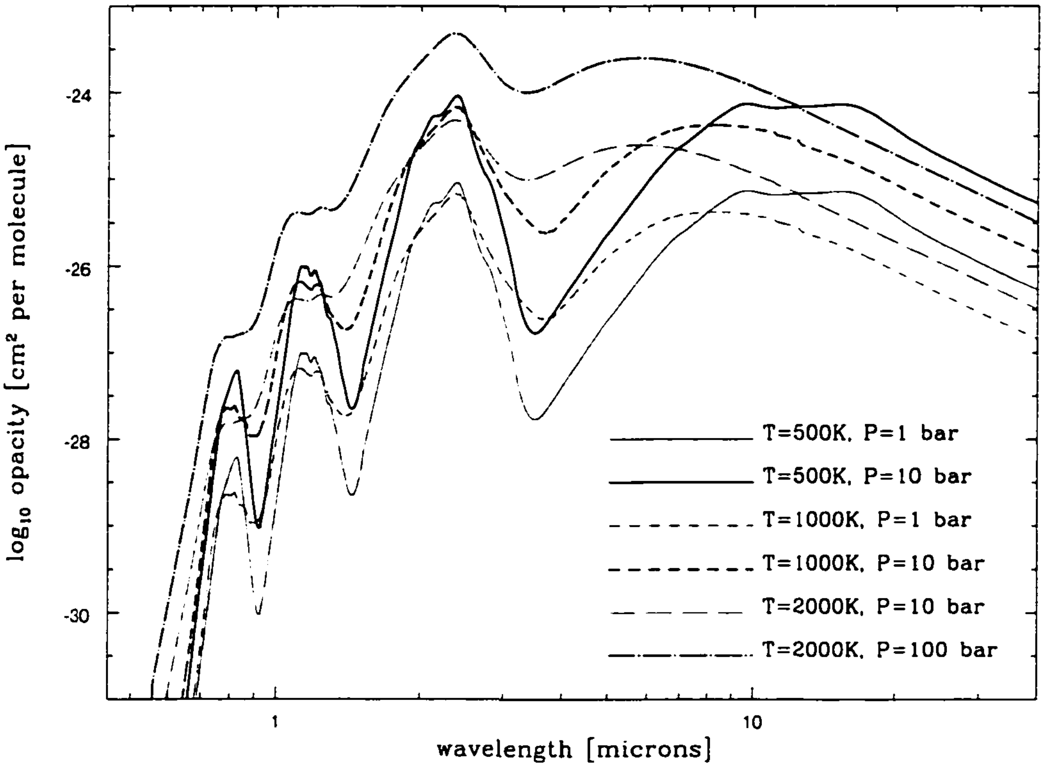

Figure 4.5 H_2-H_2 collision-induced absorption (CIA) cross sections at various temperatures and pressures.

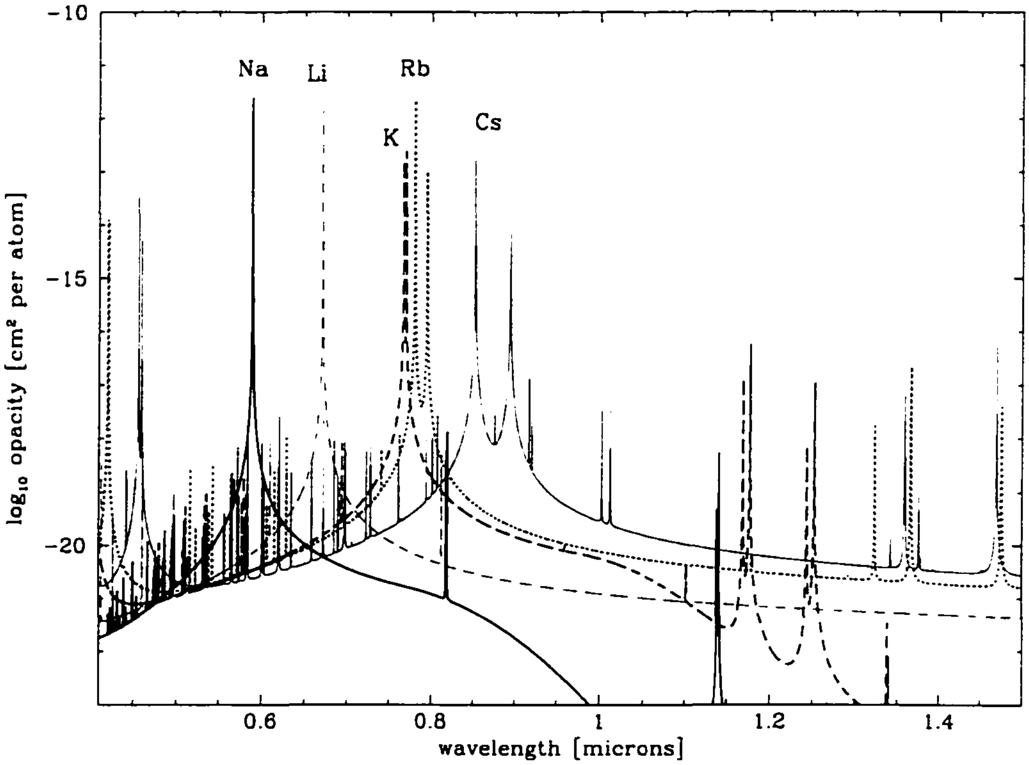

Figure 4.6 LTE absorption cross sections of the alkali metals, lithium, sodium, potassium, rubidium, and cesium. The strong pressure-broadened resonance lines of sodium and potassium are expected to dominate the visible spectra of hot EGPs. In comparison, lithium, rubidium, and cesium have lower abundances in the outer atmospheres of hot EGPs.

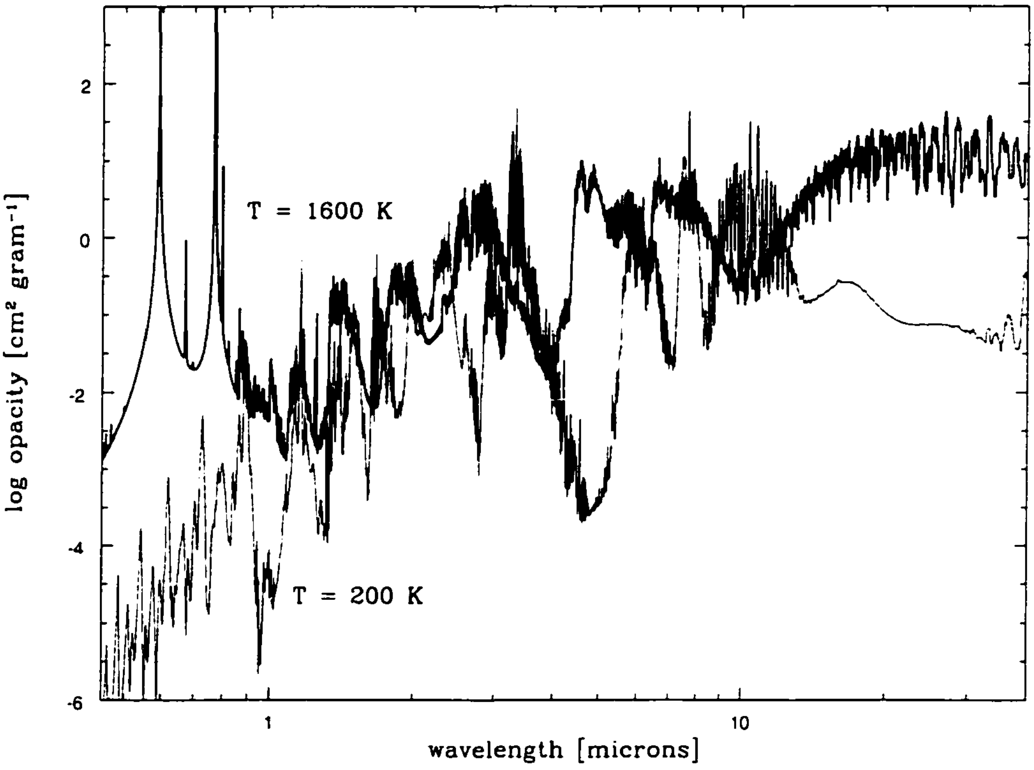

Figure 4.7 Depiction of the differences in total, abundance-weighted gaseous opacities in hot and cold EGP atmospheres at P = 1 bar. The opacity in the visible region of a hot atmosphere is up to several orders of magnitude larger than that of a relatively cold atmosphere. In contrast, there are regions in the infrared where the total opacity of the cold atmosphere is greater.

5 MIE THEORY AND OPTICAL PROPERTIES OF CONDENSATES

Condensed species in substellar objects range from ammonia ice in low temperature EGPs to silcate, iron, and aluminum compounds at high temperatures. Some of the condensates relevant to EGP atmospheres include NH_3 ($\lesssim$ 150–200 K), NH_4SH ($\lesssim$ 200 K), H_2O ($\lesssim$ 250–300 K), low-abundance sulfides and chlorides ($\lesssim$ 700–1100 K), silicates such as Mg_2SiO_4 and/or $MgSiO_3$ ($\lesssim$ 1600–2000 K), iron or iron-rich compounds ($\lesssim$ 1700–2200 K), and aluminum or calcium compounds ($\lesssim$ 1700–2200+ K). Additionally, photochemical processes in the upper atmosphere due to irradiation by a central star can produce non-equilibrium condensates. Stratospheric hazes may be composed of polyacetylene (Bar-Nun et al. 1988) and other aerosols. Chromophores, those non-equilibrium species which cause the coloration of Jupiter and Saturn, might include P_4 (Noy et al. 1981) or organic species similar to Titan tholin (Khare & Sagan 1984). Brown Dwarf atmospheres can contain a similar host of silicate, iron, and aluminum compounds. However, only the lowest temperature T-Dwarfs will contain condensed water, since the temperatures are simply too high in most objects. Due to the absence of ultraviolet irradiation, isolated brown dwarfs are not expected to contain significant levels of photochemical products.

Condensates can have large effects on the emergent spectra of EGPs and brown dwarfs. The optical properties of most condensates are relatively featureless in comparison with molecular bands and atomic lines. Hence, the presence of condensates tends to "gray" the spectrum by shallowing the troughs and shortening the spectral peaks, providing opacity at the wavelengths at which the radiation would otherwise escape. In EGPs, condensates are the principal source of scattering of incident irradiation, and if located in the outer atmosphere, their presence increases the reflected light in the visible and near-infrared region of the spectrum. One exception is the presence of non-equilibrium photochemical species with absorptive optical properties in the UV/blue, a region of the spectrum that in the absence of these species can be quite reflective due to the Rayleigh scattering of incident radiation.

Of course, those condensates that are higher in the atmosphere generally will have a greater effect on emergent spectra than those that reside more deeply, unless the high condensed layer is very optically thin. The presence and location of a particular condensed species is determined largely by an object's T-P profile, and by the tendency of the condensate to settle (to "rain out" due to the gravitational field) at a depth in the atmosphere near the region where the T-P profile crosses the condensation curve. Hence, a given low-temperature EGP atmosphere ($T_{eq} \lesssim$ 150 K) might consist of an ammonia cloud deck high in the troposphere and a water cloud deck somewhat deeper, with purely gaseous regions above, beneath, and between the clouds. Similarly, a higher-temperature atmosphere (~1200 K) might consist of a tropospheric silicate cloud deck above a deeper iron cloud deck. Depending upon the wavelength region and the amount of condensate in the upper cloud, the presence of deeper clouds may or may not have a recognizable effect on the emergent spectrum. If for all wavelengths the cloud deck resides at $\tau_\lambda \gg 1$, there will be little effect on the emergent spectrum.

5.1. Mie Theory

The scattering and absorption of electromagnetic radiation by condensed species in planetary and brown dwarf atmospheres is a very complex problem. The scattering properties of ices, grains, and droplets of various sizes, shapes, and compositions cannot be described accurately by simple means. Most often, these scattering properties are approximated by Mie Theory, which describes the solution of Maxwell's equations inside and outside a homogeneous sphere with a given complex refractive index. A full description of Mie Theory is quite lengthy, so here I present only the computational method and relevant equations.

As per van de Hulst (1957), the scattering and extinction coefficients are

$$Q_{sca} = \frac{\sigma_{scat}}{\pi a^2} = \frac{2}{x^2} \sum_{n=1}^{\infty} (2n+1)[\mid a_n \mid^2 + \mid b_n \mid^2] \tag{5.1}$$

and

$$Q_{ext} = \frac{\sigma_{ext}}{\pi a^2} = \frac{2}{x^2} \sum_{n=1}^{\infty} (2n+1) Re(a_n + b_n), \tag{5.2}$$

where a is the particle radius, x is the size parameter ($= 2\pi a/\lambda$), and a_n and b_n are the Mie coefficients. As per Deirmendjian (1969), for numerical computation these coefficients can be expressed in terms of the complex index of refraction, $m = n_{real} - i n_{imag}$, and Bessel functions of fractional order:

$$a_n = \frac{\left[\frac{A_n(mx)}{m} + \frac{n}{x}\right] J_{n+\frac{1}{2}}(x) - J_{n-\frac{1}{2}}(x)}{\left[\frac{A_n(mx)}{m} + \frac{n}{x}\right] \left[J_{n+\frac{1}{2}}(x) + (-1)^n i J_{-n-\frac{1}{2}}(x)\right] - J_{n-\frac{1}{2}}(x) + (-1)^n i J_{-n+\frac{1}{2}}(x)} \tag{5.3}$$

and

$$b_n = \frac{\left[m A_n(mx) + \frac{n}{x}\right] J_{n+\frac{1}{2}}(x) - J_{n-\frac{1}{2}}(x)}{\left[m A_n(mx) + \frac{n}{x}\right] \left[J_{n+\frac{1}{2}}(x) + (-1)^n i J_{-n-\frac{1}{2}}(x)\right] - J_{n-\frac{1}{2}}(x) + (-1)^n i J_{-n+\frac{1}{2}}(x)}, \tag{5.4}$$

where

$$A_n(mx) = \frac{J_{n-\frac{1}{2}}(mx)}{J_{n+\frac{1}{2}}(mx)} - \frac{n}{mx}. \tag{5.5}$$

The scattering asymmetry factor, $g = <\cos\theta>$, is obtained by taking the first moment of the normalized scattering phase function, $p(\theta)$:

$$g = \frac{1}{2}\int_{-1}^{1} p(\theta)\cos\theta d(\cos\theta), \tag{5.6}$$

which can be expressed in terms of the Mie coefficients as

$$g = \frac{4}{x^2 Q_{sca}} \sum_{n=1}^{\infty} \left[\frac{n(n+2)}{n+1} Re(a_n a_{n+1}^* + b_n b_{n+1}^*) + \frac{2n+1}{n(n+1)} Re(a_n b_n^*) \right]. \tag{5.7}$$

where the asterisks signify complex conjugation.

The infinite sums in Eqs. (5.1), (5.2), and (5.7) are truncated between 50 and 200 terms depending on the value of the size parameter. Large size parameters require more terms in order to produce accurate asymmetry factors and scattering and extinction coefficients. For size parameters larger than ~ 75, variations in Q_{ext}, Q_{sca} and g are much reduced. I use an asymptotic form of the Mie equations for large x outlined fully by Irvine (1964) to find the limits of the scattering coefficients and asymmetry factors. (The extinction coefficient, Q_{ext}, simply approaches 2.0.) Interpolation between the full Mie theory results and these asymptotic limits yields the coefficients for large size parameters. However, inherent assumptions in the asymptotic form of the Mie equations render them inadequate for the computation of the scattering coefficients in the weak-absorption limit ($n_{imag} \lesssim 10^{-3}$), in which case I use the geometric optics approximation (Bohren & Huffman 1983),

$$Q_{sca} = 2 - \frac{8}{3}\frac{n_{imag}}{n_{real}} \left[n_{real}^3 - \left(n_{real}^2 - 1\right)^{3/2} \right] x. \tag{5.8}$$

Figure 5.1 shows the Mie theory results for the visible and near-infrared extinction and scattering coefficients of H_2O ice spheres of radii 0.5, 5, and 50 μm.

The major oscillations in Q_{ext} (and Q_{sca}) as a function of wavelength are due to interference between diffracted and directly transmitted light. The magnitude of Q_{ext} tends to be largest when the wavelength is of the same order as the particle size. A finer rippled structure, due to internal reflection and surface waves, is also prominent where the wavelength and particle size are of the same order. These minor oscillations are very rarely observed in nature because they are washed out both by a distribution of particle sizes and because particle shapes deviate from spheres. In fact, a distribution of particle sizes can wash out the major oscillations as well.

Figure 5.2 shows the scattering asymmetry factors for 0.5 μm, 5 μm, and 50 μm H_2O ice spheres. Overall, the degree of forward scattering is greater for larger particle sizes. Indeed, as the size parameter ($x = 2\pi a/\lambda$) becomes very small, the Rayleigh scattering limit of forward-backward scattering symmetry is reached.

5.2. Optical Properties of Condensates Relevant to EGP Atmospheres

The principal condensates to which I have applied the Mie theory (roughly in order of increasing condensation temperature) include NH_3 ice, H_2O ice and liquid, chromium, $MgSiO_3$ (enstatite), Mg_2SiO_4 (forsterite), $MgAl_2O_4$ (magnesium-aluminum spinel), iron, Al_2O_3 (corundum), and $Ca_2Al_2SiO_7$ (gehlenite).

The optical constants (complex indices of refraction) for ammonia ice, H_2O ice, and H_2O liquid were obtained from Martonchik et al. (1984), Warren (1984), and Warren (1991), respectively. The constants for enstatite, magnesium-aluminum spinel, iron, and corundum were obtained from Dorschner et al. (1995), Tropf & Thomas (1990), and Gervais (1990), respectively. The indices for iron were provided by Aigen Li (private communication, 2002). Those for forsterite shortward of ~ 33 μm were taken from Scott & Duley (1996); longward of this wavelength, the indices were provided by Aigen Li. For gehlenite, the real index was taken from Burshtein et al. (1993) and an absorbance spectrum (Rossman & Taran) was used to derive the imaginary index:

$$k(\lambda) = \frac{-\lambda}{4\pi z}\log\left[\frac{I(\lambda)}{I_0(\lambda)}\right], \tag{5.9}$$

where $I_0(\lambda)$ is the incident intensity on a slab of gehlenite of thickness z, and $I(\lambda)$ is the transmitted intensity.

Figures 5.3 and 5.4 depict the real and imaginary indices of refraction for many of the condensates thought to exist in EGPs and brown dwarf atmospheres. Some of these condensates have relatively strong absorption features, which for a distribution of particle sizes is generally evident from the magnitude of the imaginary index of refraction. H_2O ice has broad absorption features at ~ 1.5, 2, and 3, and 4.5 μm. Those of water in liquid form mirror these quite well, with only small displacements, mainly to shorter wavelengths. The silicates, $MgSi_2O_4$ and $MgSiO_3$ have broad features near 10 and ~ 20 μm and at $\lesssim$ 0.2 and 0.35 μm, respectively. $MgAl_2O_4$ absorbs strongly only in the infrared, and especially around 15 and 20 μm.

Figure 5.5 shows the optical properties of ammonia ice, along with some nonequilibrium condensates that are relevant to Jupiter (and perhaps to many EGPs as well), including phosphorus (Noy et al. 1981), tholin (Khare & Sagan 1984), and polyacetylene (Bar-Nun et al. 1988). Ammonia ice, a principal condensate at low temperatures, exhibits little relative absorption in the blue and visible spectral regions. However, it can provide absorption in the infrared with particular strength near 2.0, 2.25, 3, 4.3, 6.2, 9.5 μm and elsewhere. P_4 and tholin are chromophore candidates for the coloration of Jupiter and Saturn, due to their large imaginary indices of refraction in the ultraviolet/blue and their plausibility of production. A somewhat yellowish allotrope of phosphorus, P_4 was produced in the laboratory by Noy et al. (1981) by ultraviolet irradiation of an H_2/PH_3 gaseous mixture. It is believed that this same process may be responsible for its production in Jupiter. Tholin is a dark-reddish organic solid (composed of over 75 compounds) synthesized by Khare and Sagan (1984) by irradiation of gases in a simulated Titan atmosphere. It is believed that a tholin-like solid may be produced similarly in giant planet atmospheres. Polyacetylenes, polymers of C_2H_2, were investigated by Bar-Nun et al. (1988) and likely are an optically dominant species in the photochemical stratospheric hazes of giant planets, where hydrocarbons are abundant (Edgington et al. 1998; Noll et al. 1986).

5.3. Particle Size Distributions

Cloud particle sizes are not easily modeled and are a strong function of the unknown meteorology in EGP atmospheres. Inferred particle sizes in Solar System giant planet atmospheres can guide EGP models, although they range widely from fractions of a micron to tens of microns.

I have investigated various particle size distributions. A commonly used distribution is

$$n(a) \propto \left(\frac{a}{a_0}\right)^6 \exp\left[-6\left(\frac{a}{a_0}\right)\right], \tag{5.10}$$

which reproduces the distributions in cumulus water clouds in Earth's atmosphere fairly well if the peak of the distribution is $a_0 \sim 4\mu m$ (Deirmendjian 1964).

Stratospheric aerosols—at least those in Earth's stratosphere—can be represented by the "haze" distribution (Deirmendjian 1964),

$$n(a) \propto \frac{a}{a_0} \exp\left[-2\left(\frac{a}{a_0}\right)^{1/2}\right]. \tag{5.11}$$

In the present work, I use a "cloud" distribution with various modal particle sizes. My fiducial modal particle radius for water and ammonia is 5 μm, as informed by Deirmendjian (1964) as well as measurements of the atmosphere of Jupiter. (But a "haze" distribution is used when modeling the polyacetylene distribution in Jupiter's outermost atmosphere.) For grains such as silicates and iron, my fiducial modal particle size is 10 μm, a value in broad agreement with recent cloud models for EGPs and brown dwarfs (Cooper et al. 2002; Ackerman & Marley 2001).

5.4. A Sample of the Results: Condensate vs. Gas Opacities

The wavelength-dependent scattering and absorption opacities for some of the cloud species used in my fiducial EGP models are presented in Figures 5.6 and 5.7. For comparison, total gaseous absorption opacities at the same level in the atmosphere at which the clouds resides are plotted. Figure 5.6 pertains to the atmosphere of a Class V roaster. Silicate (forsterite) and iron clouds reside near 10 mbar, where the atmospheric temperature is $\sim$ 1600 K. For both forsterite and iron, a "cloud" particle size distribution with a modal size of 10 μm is used. At a temperature of 1600 K, the dominant gaseous opacity sources are sodium, potassium, water, and CO. In the visible region, the cloud opacities overwhelm the gas-phase opacities, the only exceptions being the sodium and potassium line cores. Forsterite is a strong absorber in the visible and near infrared, while scattering due to forsterite and iron is roughly an order of magnitude weaker. In the mid-infrared ($\gtrsim$ 5 μm), the gaseous opacities dominate. Given that this comparison plot corresponds to the outer regions of the atmosphere, it is obvious that the clouds will have an effect on the visible and near-infrared spectrum of an EGP. However, the magnitude of this effect will depend largely upon the vertical extent of the cloud. Since the condensates have a limited vertical extent (on the order of a pressure scale height), and the gases do not, the presence of gases above the cloud generally will reduce the influence of the cloud on the emergent spectrum. In the case of optically thin clouds high in the atmosphere, the formation of the spectrum will also depend strongly on the deeper gaseous regions.

Figure 5.7 pertains to the atmosphere of a cooler Class II EGP. I compare the opacities due to a water (ice) cloud at 1 bar and 250 K with those of the gas-phase species. A "cloud" particle size distribution with a modal size of 5 μm is used, assuming that 10% of the total water abundance in the cloud region condensed. At a temperature of 250 K, the dominant gaseous opacity sources are water, methane, and ammonia. Scattering is the primary contribution of the condensed water in the visible and near-infrared regions. Hence, one should expect that the presence of a water cloud in an EGP atmosphere will result in reflection of incident radiation from the EGP's central star, the degree of which will depend upon the height and thickness of the cloud. I'll discuss the effects of clouds on actual EGP emergent spectra in Chapters 6 and 7.

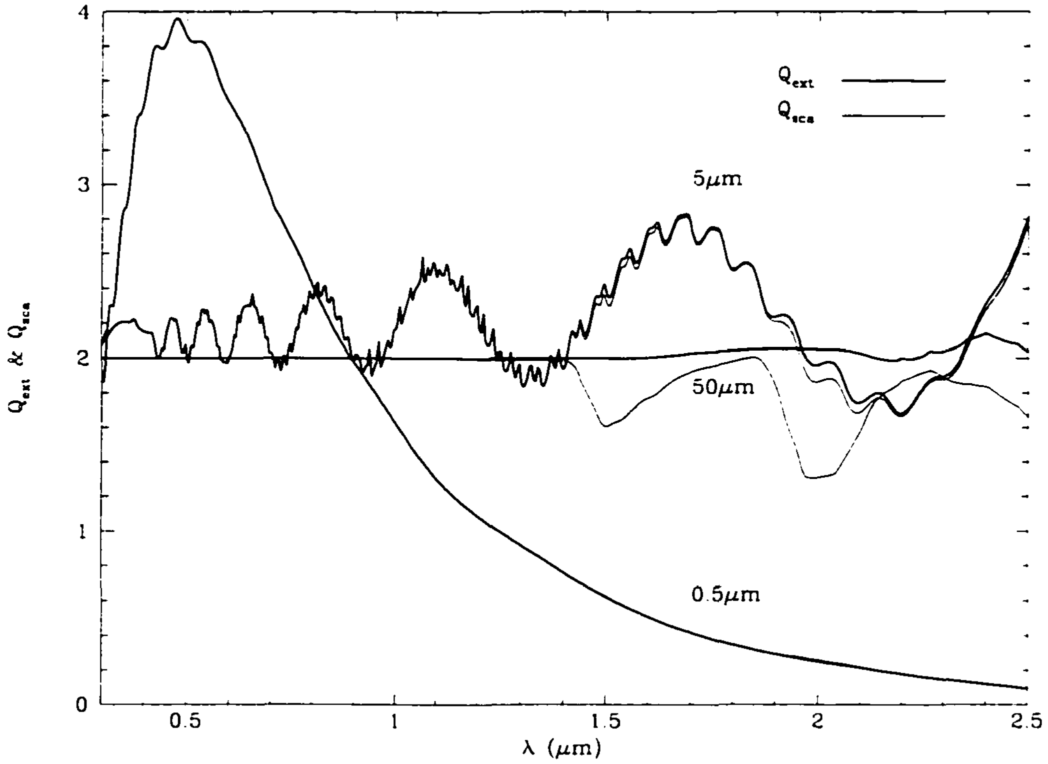

Figure 5.1 Mie theory extinction and scattering results for ice spheres of radius 0.5, 5, and 50 μm. Q_{ext} is depicted by the thick curves, and Q_{sca} by the thin curves. The degree of extinction tends to be largest when the wavelength is of the same order as the particle size.

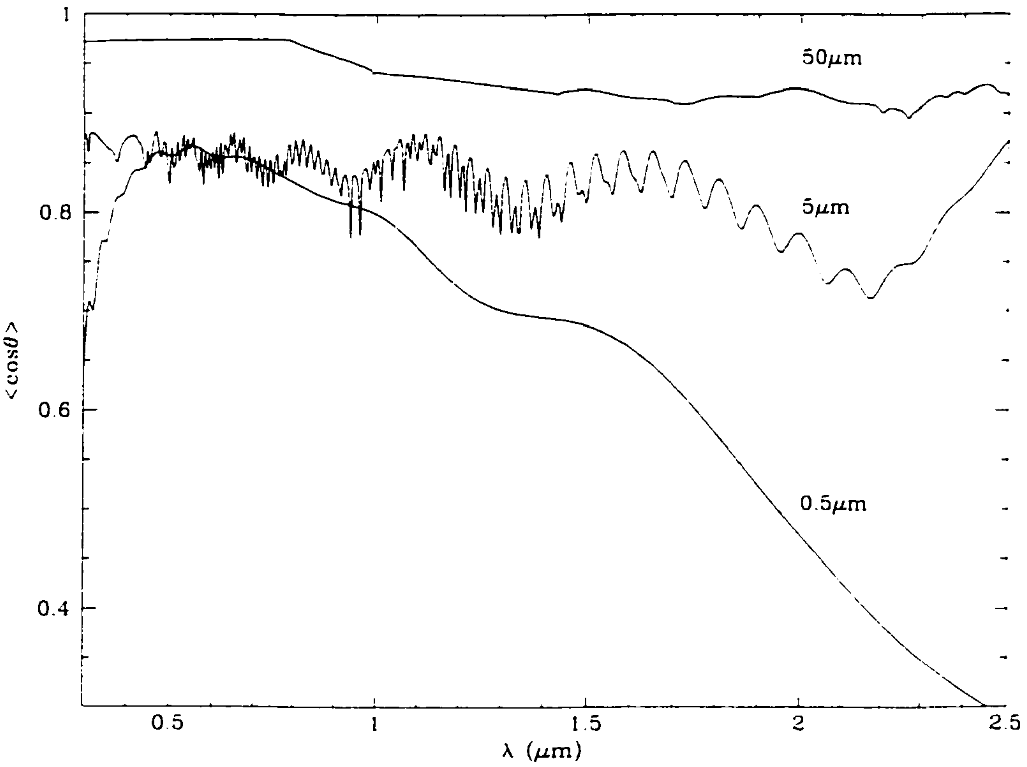

Figure 5.2 Mie theory scattering and asymmetry factor results for ice spheres of radius 0.5, 5, and 50 μm. Overall, the degree of forward scattering is greater for larger particles.

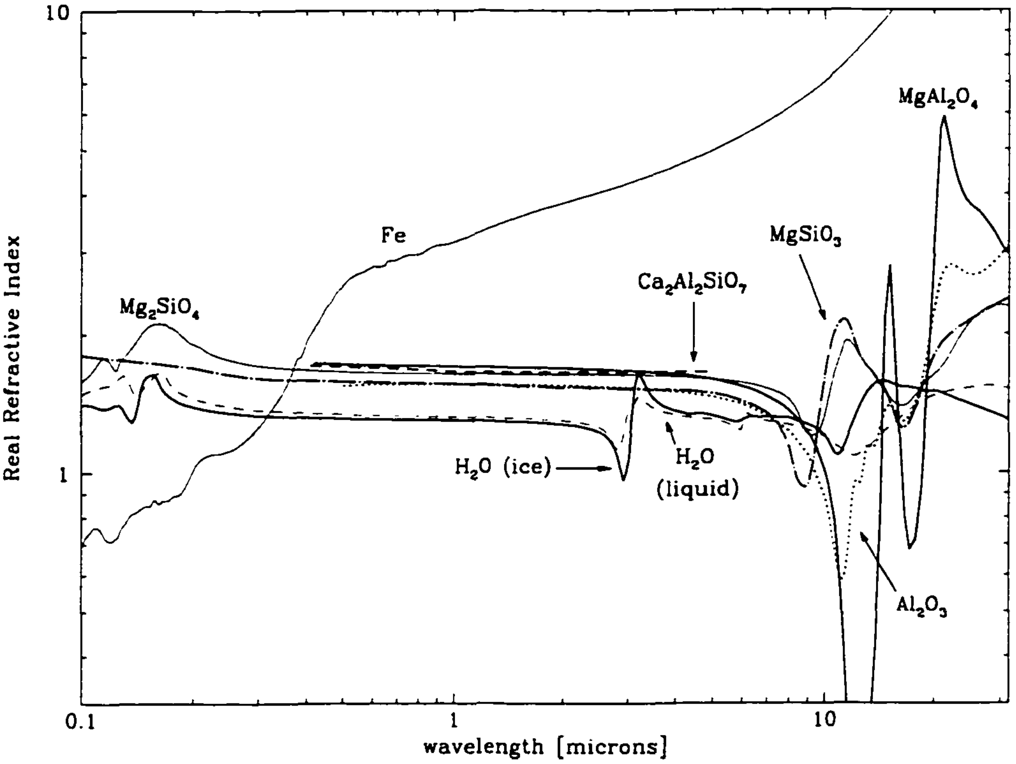

Figure 5.3 Real indices of refraction for condensates relevant to the atmospheres of EGPs.

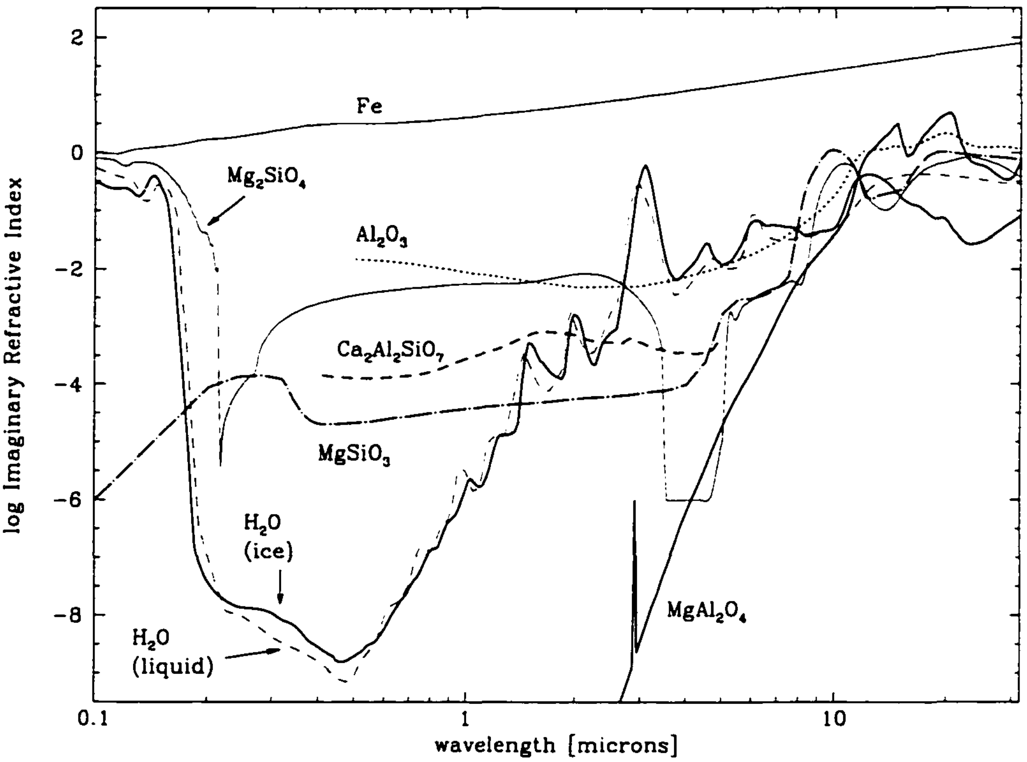

Figure 5.4 Imaginary indices of refraction for condensates relevant to the atmospheres of EGPs. Generally, for a distribution of particle sizes, absorption features are evident from the magnitude of this index.

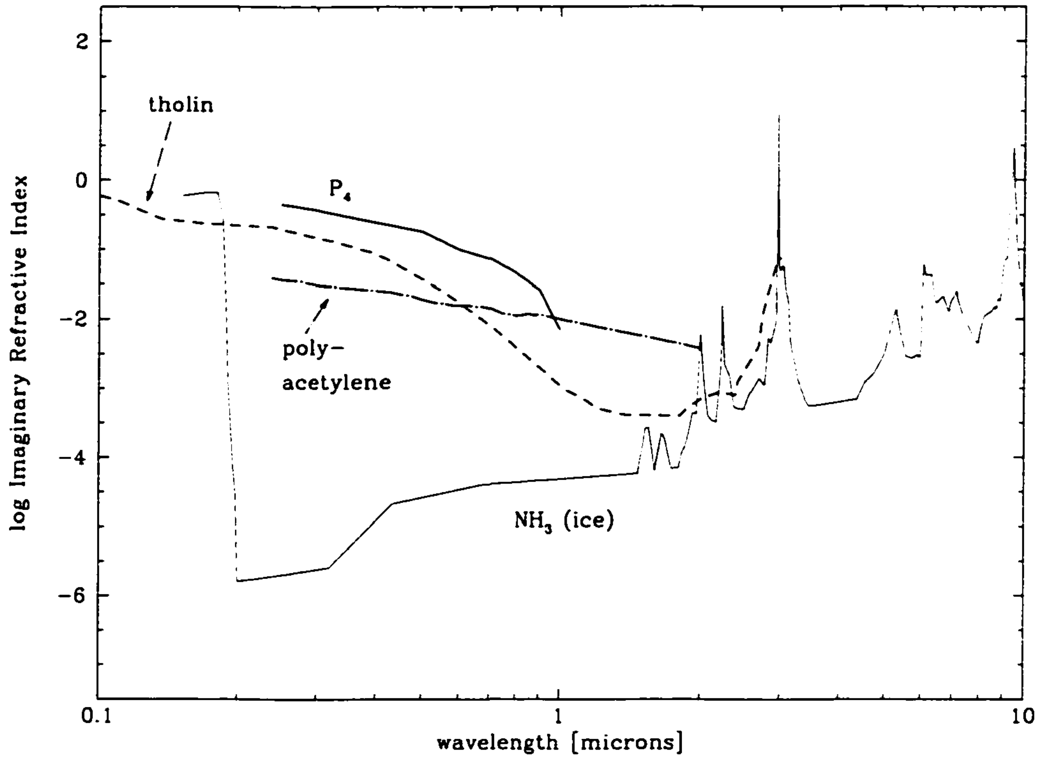

Figure 5.5 Imaginary indices of refraction for ammonia ice and candidate nonequilibrium species relevant to Jupiter, and perhaps to EGPs as well.

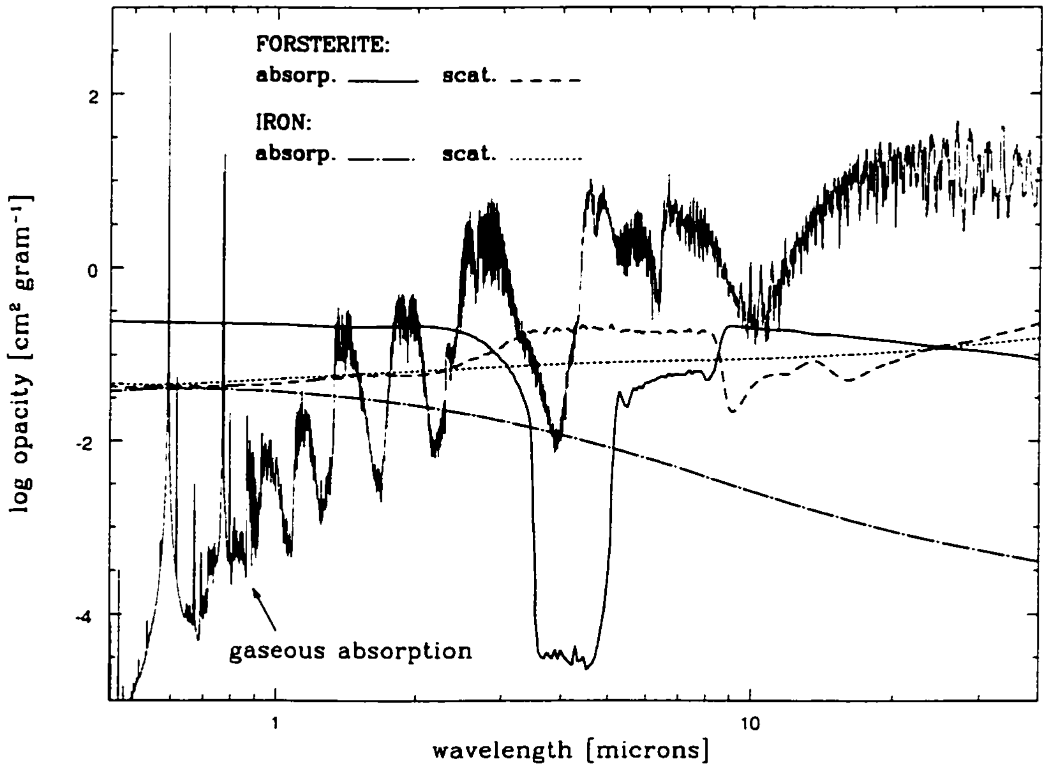

Figure 5.6 Absorption and scattering opacities of forsterite and iron compared with the total gaseous opacity at T = 1600 K, P = 10 mbar. A Deirmendjian "cloud" particle size distribution with a median size of 10 μm was used. The opacities shown are the cross sections per gram of the total atmosphere.

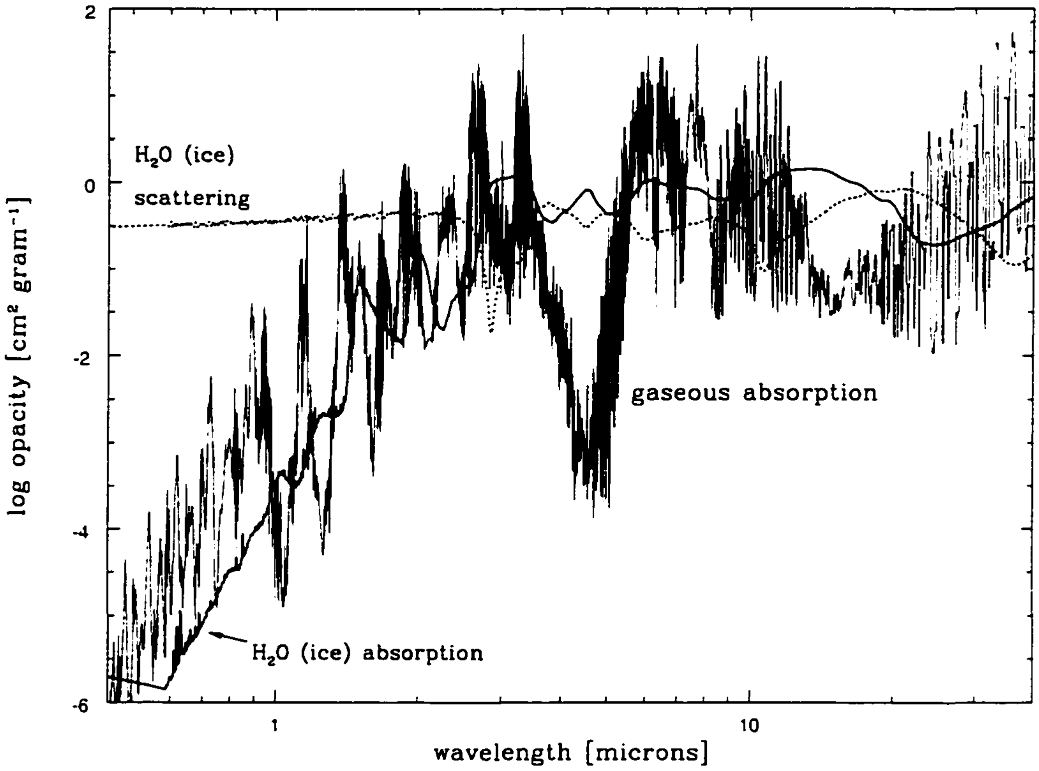

Figure 5.7 Absorption and scattering opacities of condensed water (ice) compared with the total gaseous opacity at T = 250 K, P = 1 bar. A Deirmendjian "cloud" particle size distribution with a median size of 5 μm was used, assuming that 10% of the total water abundance in the cloud region condensed. The opacities shown are the cross sections per gram of the total atmosphere.

6 CLASSES OF EXTRASOLAR GIANT PLANETS

What do extrasolar planets look like? I'll discuss and portray the atmospheric structures and emergent spectra of the EGP classes in this chapter. leaving models of specific EGP systems and parameter studies for Chapters 7 and 8.

Due to qualitative similarities in the compositions and spectra of objects within several broad effective temperature ranges. EGPs fall naturally into groups, or "composition classes." At low temperatures ($\lesssim$ 150 K) is a class of "Jovian" objects (Class I) with tropospheric ammonia clouds and strong gaseous methane absorption. Somewhat warmer Class II, or "water class" EGPs are affected by condensed H_2O. as well as water and methane vapor.

When the upper atmosphere of an EGP is too hot for water to condense, radiation generally penetrates more deeply. In these objects, designated Class III, "clear" or "gaseous," due to a lack of condensation in the upper atmosphere, the ro-vibrational molecular absorption bands of water and methane are very strong. Additionally, the resonance lines of sodium and potassium present themselves in the visible (at ~ 0.6 μm and ~ 0.77 μm, respectively) and collision-induced absorption (CIA) by H_2 molecules affects the infrared.

In those EGPs with exceedingly small orbital distance and outer atmospheric temperatures in excess of ~ 900 K (Class IV), strongly pressure-broadened resonance lines of sodium and potassium are expected to dominate the visible spectrum, while molecular absorption in the infrared remains strong. Tropospheric silicate and iron layers are expected to exist, but in all but the hottest ($\gtrsim$ 1400 K) or lowest gravity close-in EGPs (Class V), these layers are too deep to have significant effects on the emergent spectra. The very hot Class V EGPs differ in important ways from Class IV EGPs. These extremely close-in "roasters" are hot enough and/or have a low enough surface gravity that silicate and/or iron clouds condense very high in the atmosphere at pressures less than 100 millibars, in contrast to the deep clouds of Class IV objects. Hence, grains can have substantial effects on the emergent spectra of Class V roasters. Futhermore, at such high temperatures, nearly all the carbon is taken up by CO, so methane features in Class V EPGs are very weak or nonexistent.

Figure 6.1 depicts sample temperature-pressure structures for Classes I through V. Also shown are the condensation curves for the principal condensates, ammonia, water, forsterite (a representative silicate), and iron. The intersection of a T-P profile with a condensation curve indicates the approximate position of the base of a condensate cloud. (For clarity, the smooth T-P profiles of cloud-free models are shown.) The Class I profile intersects the ammonia condensation curve at roughly one bar. At greater pressures, the temperature is too high for ammonia condensation to occur. This profile also intersects the water condensation curve at nearly 10 bars, indicating the presence of water clouds at this depth. Of course, a whole variety of Class I objects with differing T-P profiles will exist, and the ammonia and water condensation curves will be intersected at different pressures for each object, but by definition, Class I EGPs have an ammonia cloud that is well above a water cloud. The warmer Class II profile crosses only the water condensation curve, indicating the existence of a water cloud in the upper atmosphere. Classes IV and V intersect the silicate and iron condensation curves, but at quite different pressures. Figure 6.1 is a general guide to the T-P structures and approximate positions of the various principal condensate clouds in the atmospheres of a full range of EGPs. However, more model-specific details are offered in Chapters 7 and 8

6.1. Jovian Class I EGPs

Class I EGPs orbit at distances of at least a few AU from their central stars. With $T_{eq} \lesssim 150$ K, the spectrum of such a cool, Jovian-like gas giant at 10 parsecs is shown in Figure 6.2. Methane and ammonia are the dominant gaseous species, because at these low temperatures, carbon is predominantly in the form of CH_4 rather than CO, and nitrogen is in NH_3, as opposed to N_2. The visible and near-infrared spectrum is comprised mostly of reflected stellar light, since such an object is far too cool to emit significant thermal radiation at short wavelengths. This reflection is provided mostly by the upper ammonia cloud, with some additional contribution in the blue due to Rayleigh scattering. Some ammonia ice absorption features are also indicated in Figure 6.2 by the $\{NH_3\}$ symbols, where the imaginary index of refraction is rather large ($\sim$ 1.5, 1.65, 2, and 2.2 μm). The upper atmosphere is largely depleted of H_2O, which has condensed and settled into a cloud layer at several bars pressure. Provided that the upper ammonia cloud is optically thick (here I assumed a particle size distribution peaked at 5 microns, with a condensate abundance at 10% of the total ammonia abundance), one should not expect to see substantial effects from gaseous or condensed H_2O in the visible or near infrared emergent spectrum.

Lower abundance condensates almost certainly exist as well. These include an NH_4SH cloud at pressures between those of the ammonia and water clouds, as well as very low abundance non-equilibrium photochemical solids or liquids within and above the ammonia cloud layer. I do not include these in the general Class I model, but see §7.7 for their effects in specific Jupiter models.

In our present-day Solar System, both Jupiter and Saturn are Class I objects, but it is important to note that not all EGPs orbiting at several AU will be Class I planets. Young and/or massive objects may have high enough effective temperatures (defined as $(F/\sigma)^{1/4}$ for an object in *isolation*) that ammonia will remain in gaseous form. Therefore, those hotter objects will be Class II (or even Class III).

6.2. Water Class II EGPs

Class II EGPs generally orbit at a distances of $\sim$ 1 to 2 AU, or somewhat farther out for an object with an early-type central star. Outer atmospheric temperatures ($\lesssim$ 250 K) are below that of the water condensation curve, producing an upper tropospheric cloud layer of H_2O. Figure 6.3 shows an example spectrum of a Class II EGP. Reflection in the visible and near-infrared is provided primarily by the water cloud, which I have assumed to be comprised of a particle size distribution peaked at 5 microns. While scattering by this H_2O condensate layer elevates the emergent spectrum, the spectrum is dominated by the gaseous absorption features of water, methane, and to a lesser extent, ammonia. Among the gaseous water absorption features, one may discern condensate absorption features at $\sim$ 1.5, 2, and 3.05 microns, depending in part upon the thickness of the clouds.

6.3. Gaseous Class III EGPs

Class III EGPs are too warm to contain condensed H_2O, but are too cool for silicate or iron grains to exist in their outer atmospheres. In the absence of principle condensates, I label this class as the "gaseous" or "clear" class. Typically orbiting at distances less than about 1 AU, such objects have equilibrium temperatures between $\sim$ 350 K and 800 K. Although an isolated object with $T_{eq} \sim 350$ K is likely to contain water clouds, stellar irradiation keeps the temperature of a Class III EGP high enough that its profile never reaches the condensation curve.

A purely gaseous EGP is expected to have a very low albedo. Rayleigh scattering does have an impact in the blue and visible regions of the spectrum, but the majority of the spectrum is made up almost entirely of absorption and emission. Figure 6.4 shows an example spectrum of a Class III EGP. Gaseous water and methane absorption are strong, while ammonia absorption is weakening compared with Class II. The alkali metals, particularly the sodium and potassium resonance lines at $\sim$ 0.6 μm and $\sim$ 0.77 μm, respectively, appear with modest intensity. Due to the absence of clouds, the incident radiation penetrates deeply between the near-infrared ro-vibrational absorption bands. Here, collision-induced absorption (CIA) by H_2, a continuum absorption that is strong near $\sim$ 0.8, 1.2, 2.4 μm, and longward, keeps the flux peaks lower than they would be otherwise.

The slope of the visible spectrum is a combined consequence of the λ^{-4} dependence of Rayleigh scattering and the incident stellar spectrum. The later the stellar spectral type, the flatter the slope will be if the spectral energy distribution of the star falls off rapidly with decreasing wavelength.

It is worth mentioning that low-abundance sulfide or chloride condensates could exist in the troposphere at a few bars pressure or less. Based on theoretical abundances, thick clouds are very unlikely, but even a cirrus-like layer could provide significant reflection, reducing the deep absorption troughs seen in Figure 6.4.

Figure 6.5 provides a comparison of the T-P structure of a Class III model with that of a cloud-free brown dwarf of the same effective temperature and gravity. As expected, the EGP profile is more isothermal in the outer atmosphere, while it is somewhat cooler than the brown dwarf deeper in the atmosphere. Figure 6.6 depicts the emergent spectra associated with these profiles out to 30 μm. By construction, both integrated emergent fluxes are identical, but the individual spectral energy distributions differ significantly.

Most striking is the visible region. Here, Rayleigh scattering of the incident radiation keeps the EGP flux high relative to that of the brown dwarf. Only modest sodium and potassium lines appear in the EGP spectrum, compared with very strong lines for the brown dwarf. This fact is not due to a dominance of Rayleigh scattering cross sections; the alkali cross sections are actually much larger. Rather, the equilibrium abundances of the alkalis are very low in the outermost atmospheres of both the EGP and the brown dwarf. The alkali absorption in a brown dwarf of this effective temperature occurs at pressures of $\gtrsim$ 1 bar, but the strong impinging radiation on the EGP in the visible region is reflected by Rayleigh scattering higher in the atmosphere, producing emergent flux in the visible, before this pressure region is well probed. So although alkali absorption occurs in both objects at moderate pressures, strong alkali absorption is seen only in the emergent spectrum of the brown dwarf. This is not the case if the outer atmosphere is at higher temperature, as we will see with Class IV objects (§6.4).

In the near-infrared, the peak-to-trough variations in the molecular absorption are greater in the brown dwarf than the EGP, which is expected due to the more isothermal profile of the EGP. In the case of the brown dwarf, more flux escapes in the *Z*, *J*, and to a lesser degree, the *H* band. But beyond the *K* band, the EGP infrared flux is somewhat higher.

6.4. Close-In Class IV EGPs

The close-in Class IV EGPs are those orbiting their stars well within the distance at which Mercury orbits the Sun. Many are roughly 0.1-0.2 AU from their central stars, or even closer for late-type stars. Giant planets at such small orbital distances are quite exotic by the standards of our Solar System, and their spectra are as well. With atmospheric temperatures in the 1000 K range, the alkali metal abundances increase substantially and CO takes up much of the carbon in the low-pressure outer atmosphere.

Figure 6.7 shows a Class IV EGP spectrum. Perhaps most striking is the strong absorption due to the sodium (0.6 μm) and potassium (0.77 μm) resonance lines. These lines are strongly pressure-broadened and clearly dominate the visible spectral region. Also present are the lithium ($\sim$ 0.67 μm), rubidium ($\sim$ 0.78, 0.795 μm; not labeled), and cesium doublets ($\sim$ 0.85, 0.895 μm; not labeled).

CO absorption is very strong in the 4.4-5.0 micron region, as well as at $\sim$ 2.3 μm. This comes at the expense of methane, which competes for carbon. However, methane absorption is still visible, particularly the 3.3-μm ν_3 fundamental feature. Although methane absorption is weaker, water absorption remains very strong, and, as for Class III objects, H_2 CIA absorption affects the near-infrared. At these high temperatures, N_2 takes up most of the nitrogen, so ammonia abundances are very low.

Silicate and iron clouds do form, but too deeply ($\gtrsim$ 10 bars) to affect the emergent spectrum significantly. Figure 6.8 shows the effect of a silicate cloud on the T-P profile. Despite the changes in the T-P structure at depth, the emergent spectrum is nearly identical to the cloud-free model. Both spectra are shown in Figure 6.9.

The very strong alkali absorption shown here is likely an upper limit since the neutral alkali abundances could be reduced somewhat by ionizing ultraviolet flux (see §3.5 and §8.5) or scattering by low-abundance, nonequilibrium photochemical products. In any event, strong alkali lines are expected to be prominent features of close-in Class IV EGPs.

6.5. Class V Roasters

The hottest of all EGPs are the extremely close-in Class V EGPs, or "roasters." These objects orbit their stars around 0.05 AU. The first EGP discovered, 51 Pegasi b, is good example of a roaster. Many of these objects have equilibrium temperatures that rival hot brown dwarfs ($\gtrsim$ 1400 K). Silicate and iron clouds can form quite high in the atmospheres of these EGPs, especially for low-mass, low-gravity roasters, and they have significant effects on the emergent spectra.

Figure 6.10 shows the emergent spectrum of a Class V roaster. Like Class IV EGPs, Class V objects have strong alkali metal absorption lines, although their strengths can be reduced somewhat due to reflection by condensates at altitude, and/or if the outer atmosphere becomes close to isothermal. Water and CO absorption remain strong, but unlike Class IV objects, where some methane absorption is seen, methane features in the visible and near infrared are either very weak or nonexistent, even at the 3.3-μm fundamental.

The presence of high clouds in Class V EGPs results in smaller wavelength-dependent flux variations relative to Class IV EGPs. This is mainly a result of cloud opacity blocking the flux windows between the molecular absorption features, thereby reducing the flux peaks. As a result, the absorption troughs are not as deep, since some of the blocked flux escapes in these spectral regions. Additionally, clouds reflect some of the incident stellar radiation, increasing the incident flux where the scattering opacity is high, a phenomenon that tends to be more noticeable in the vicinity of the gaseous absorption troughs.

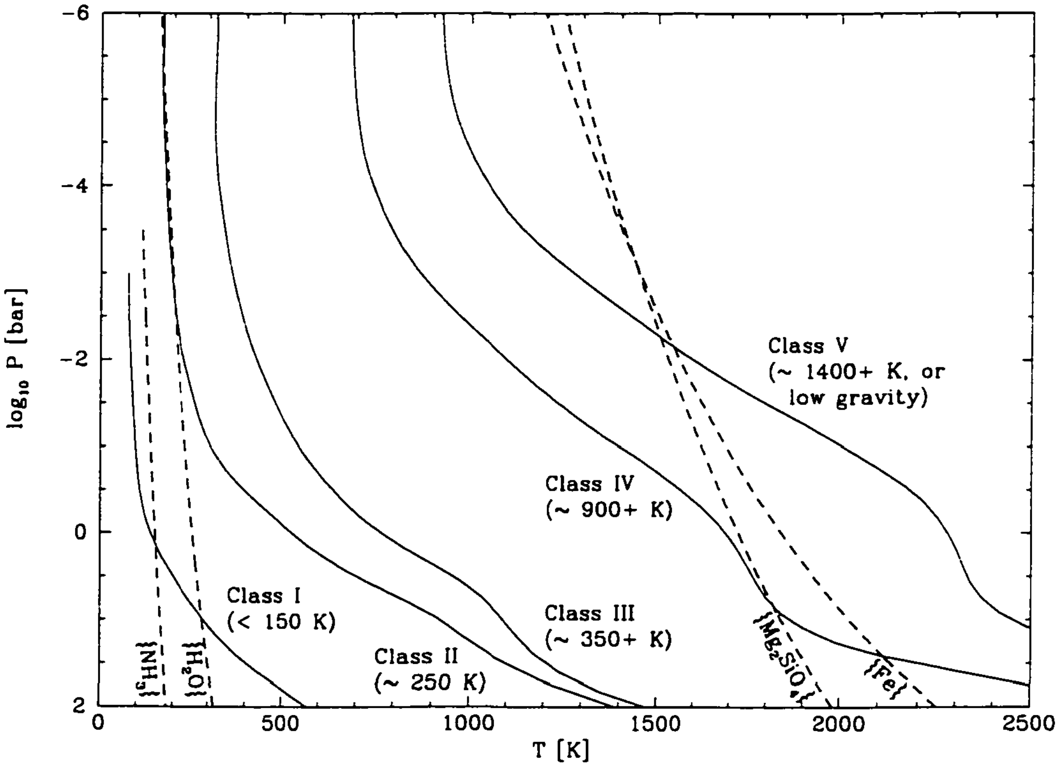

Figure 6.1 Temperature-Pressure (T-P) profiles of EGPs over the full range in effective temperature. The profiles shown represent the different EGP classes. The corresponding emergent spectra are depicted in Figures 6.2, 6.3, 6.4, 6.7, and 6.10. Condensation curves for four high-abundance condensates (ammonia, water, a silicate, and iron) are also shown. The intersection of these curves with the T-P profiles indicates the positions of cloud bases. (For clarity, cloud-free T-P profiles are shown here.)

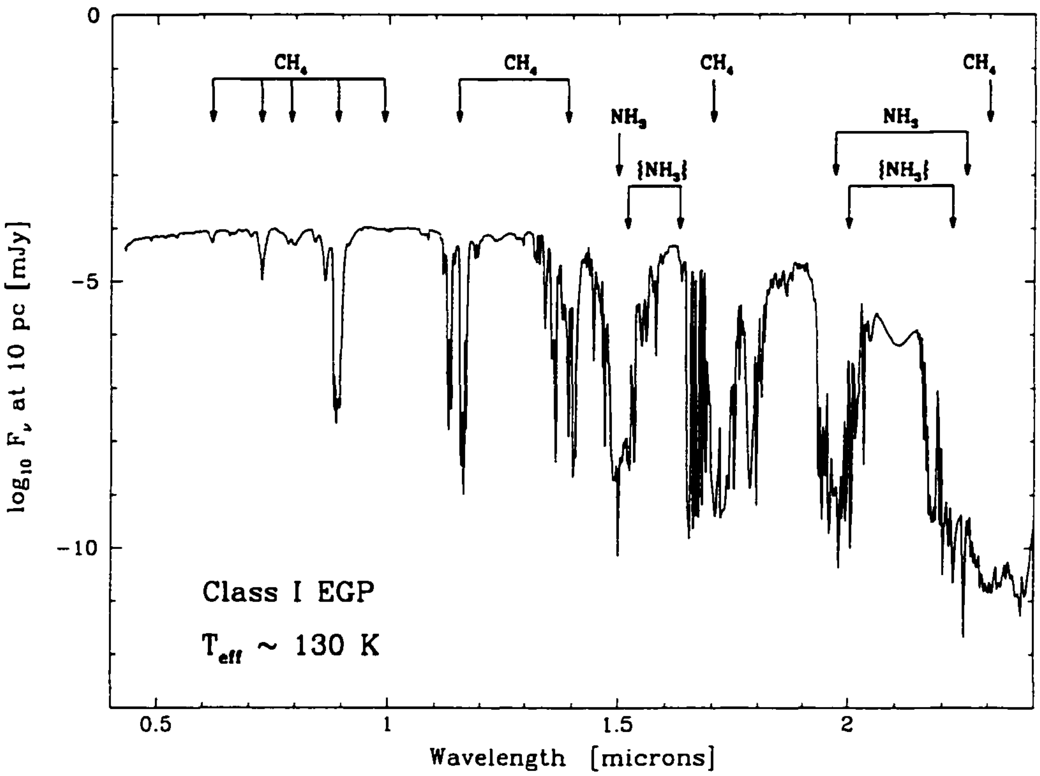

Figure 6.2 Emergent spectrum of a Class I ("Jovian": $\sim$ 5 AU) EGP. The temperature in the outer atmosphere is cold enough ($\lesssim$ 150 K) that ammonia condenses into ice, which provides significant reflection. The upper troposphere is depleted of water, which is condensed into a cloud layer at a pressure of a few-to-several bars. Methane and ammonia absorption dominate the visible and near-infrared spectrum. Note that '$\{NH_3\}$' indicates a feature of condensed ammonia, while 'NH_3' indicates that of gaseous ammonia.

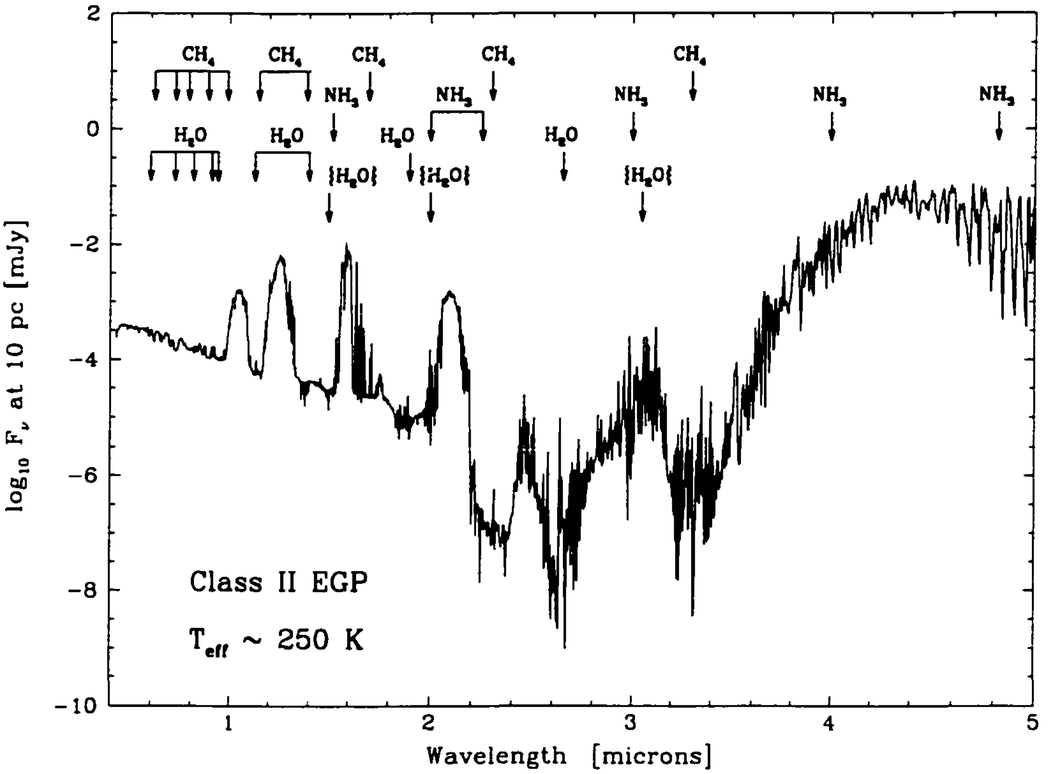

Figure 6.3 Emergent spectrum of a Class II ("water class"; ~ 1-2 AU) EGP. A water cloud resides in the upper troposphere, but the temperature at every pressure is hot enough that ammonia remains in gaseous form. Reflection by water keeps the emergent flux higher than it would otherwise be in the visible and near-infrared. Gaseous absorption by methane, water, and ammonia produce strong spectral features. Note that '{H_2O}' indicates a feature of condensed water, while 'H_2O' indicates that of gaseous water.

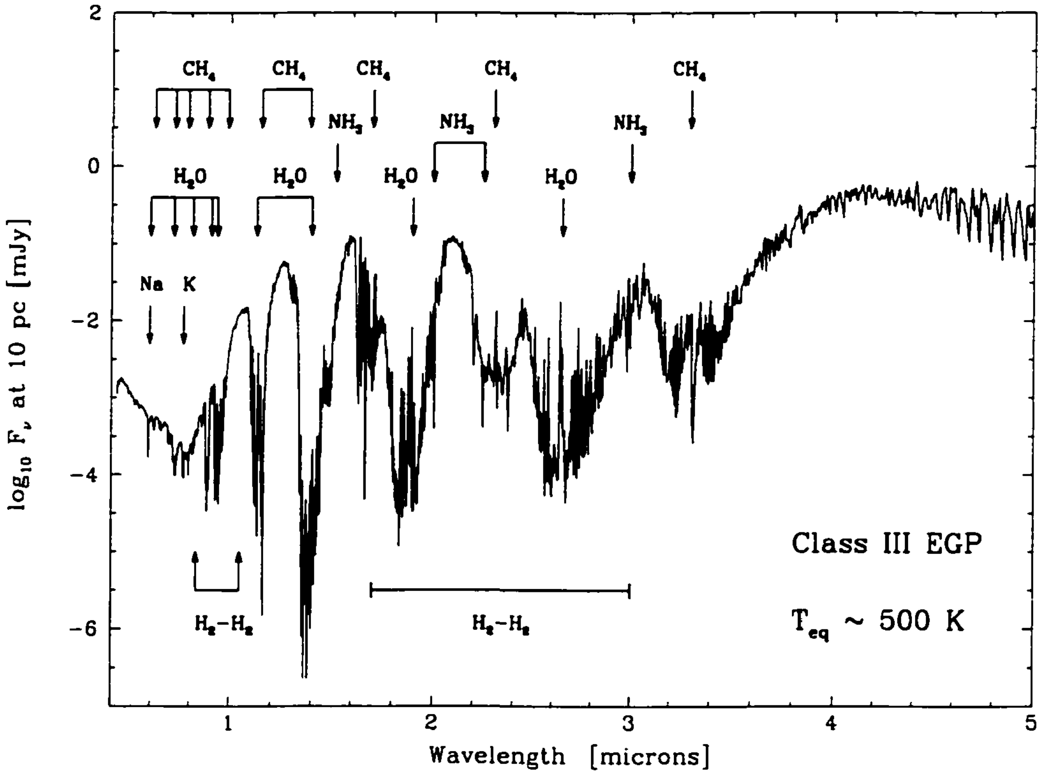

Figure 6.4 Emergent spectrum of a Class III ("clear"; ~ 0.5 AU) EGP. These objects are too warm for water to condense, but too cold for a silicate layer to appear in the upper troposphere. In the absence of any high-abundance, principal condensates, the ro-vibrational molecular absorption features are very strong. Of particular importance are absorption by gaseous water, methane, and molecular hydrogen (collision-induced). Additionally, alkali metal lines appear in the visible.

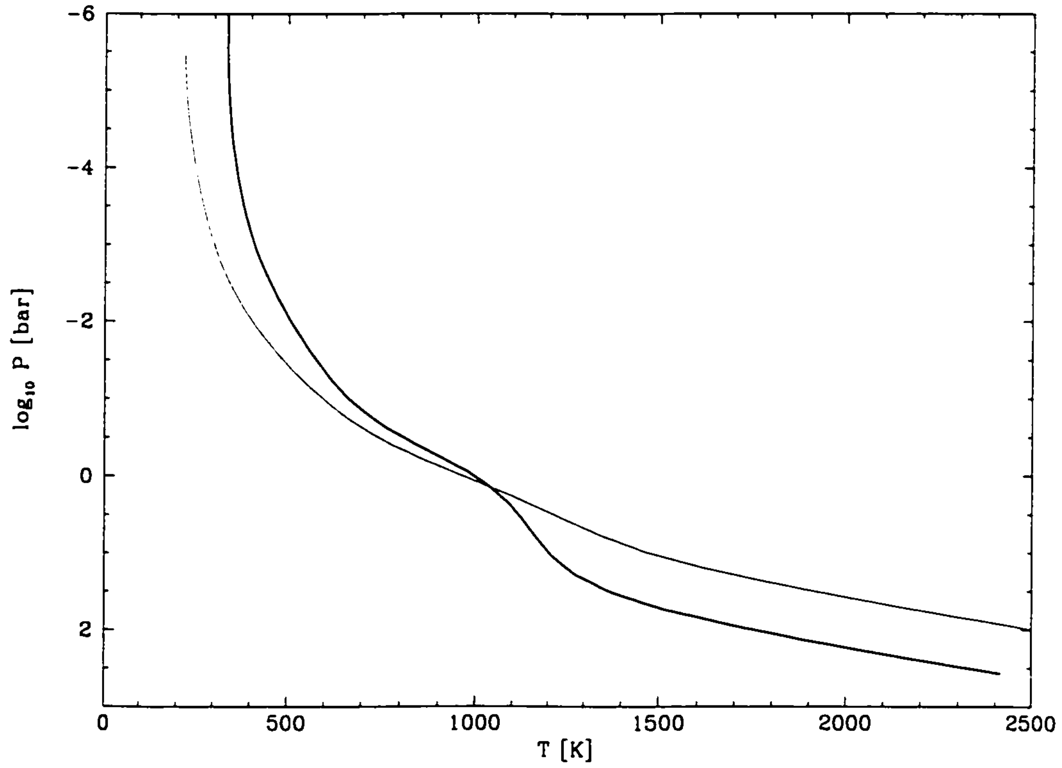

Figure 6.5 Comparison of the T-P structure of a Class III EGP (thick curve) with that of a brown dwarf (thin curve) with the same surface gravity and total integrated emergent flux. The outer atmosphere of the EGP is more isothermal due to irradiation by the primary.

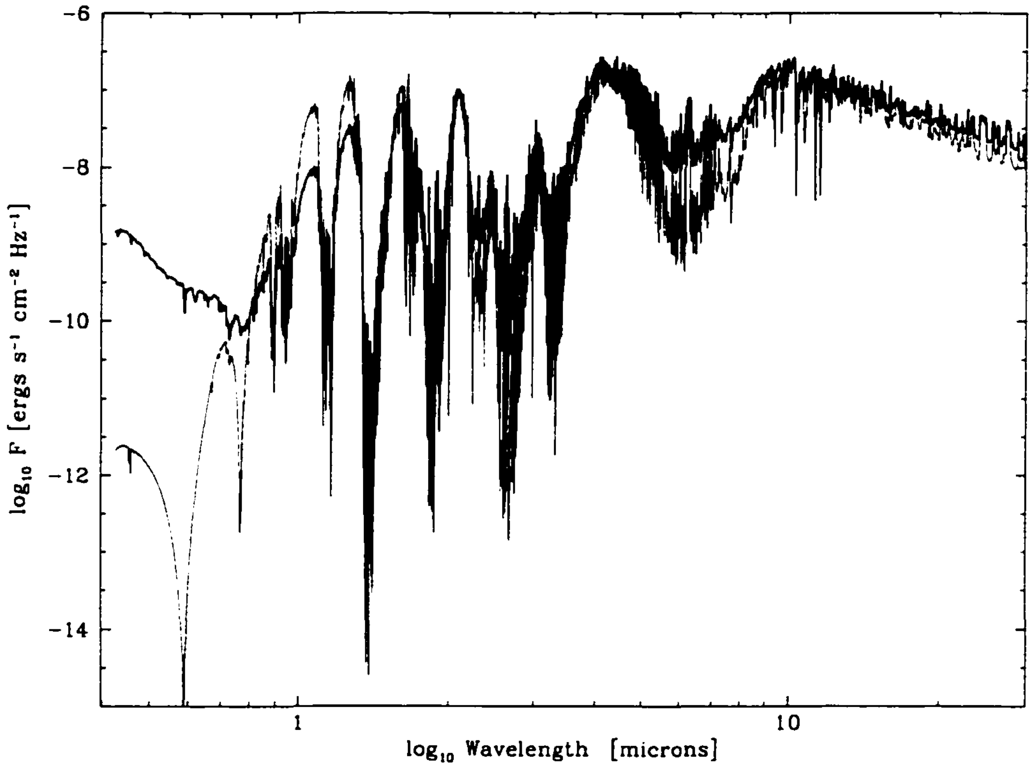

Figure 6.6 Comparison of the emergent spectrum of a Class III EGP (thick curve) with that of a cloud-free brown dwarf (thin curve) of the same effective temperature and surface gravity. By construction, the integrated emergent fluxes are identical, but the spectral energy distributions differ significantly. (Fluxes shown are at the objects' surfaces.)

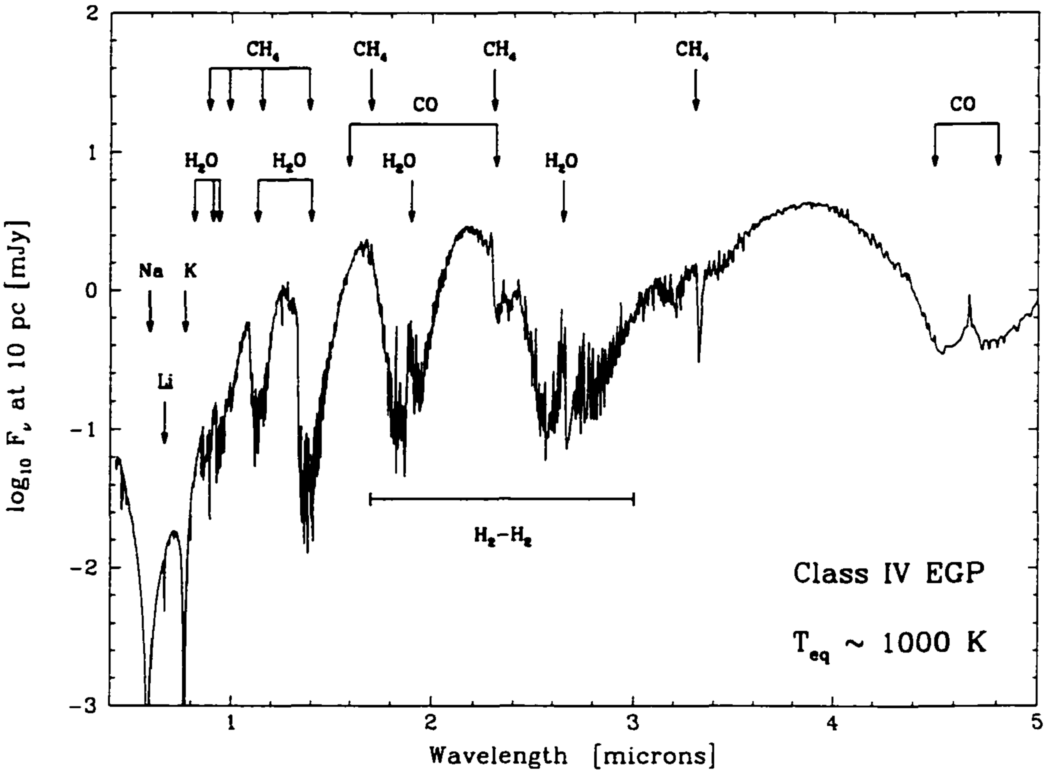

Figure 6.7 Emergent spectrum of a Class IV EGP ($\sim$ 0.1 AU). The visible spectrum is dominated by strong pressure-broadened sodium and potassium resonance lines, while gaseous water, methane, and carbon monoxide absorption are strong in the infrared. Silicate and iron clouds exist at depth, but they have no significant effects on the visible or near-infrared emergent spectra.

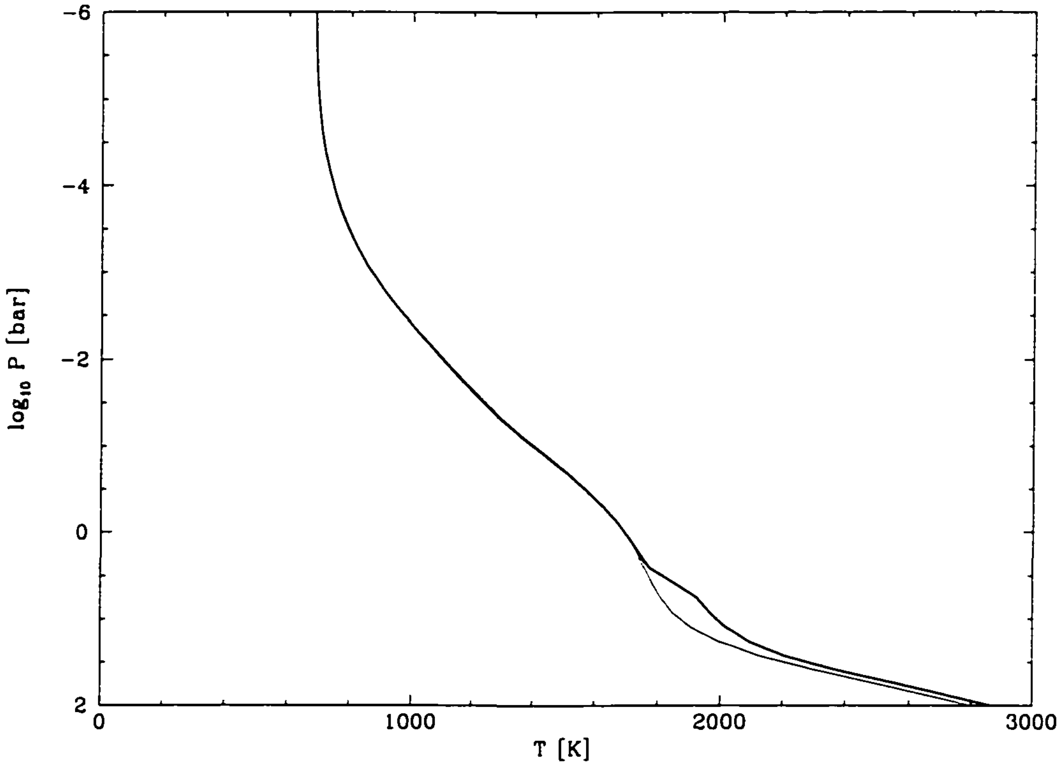

Figure 6.8 Effect of a deep silicate cloud on the T-P structure of a Class IV EGP. The resulting T-P profile (thick curve) differs from that of a cloud-free model (thin curve), but only at depth.

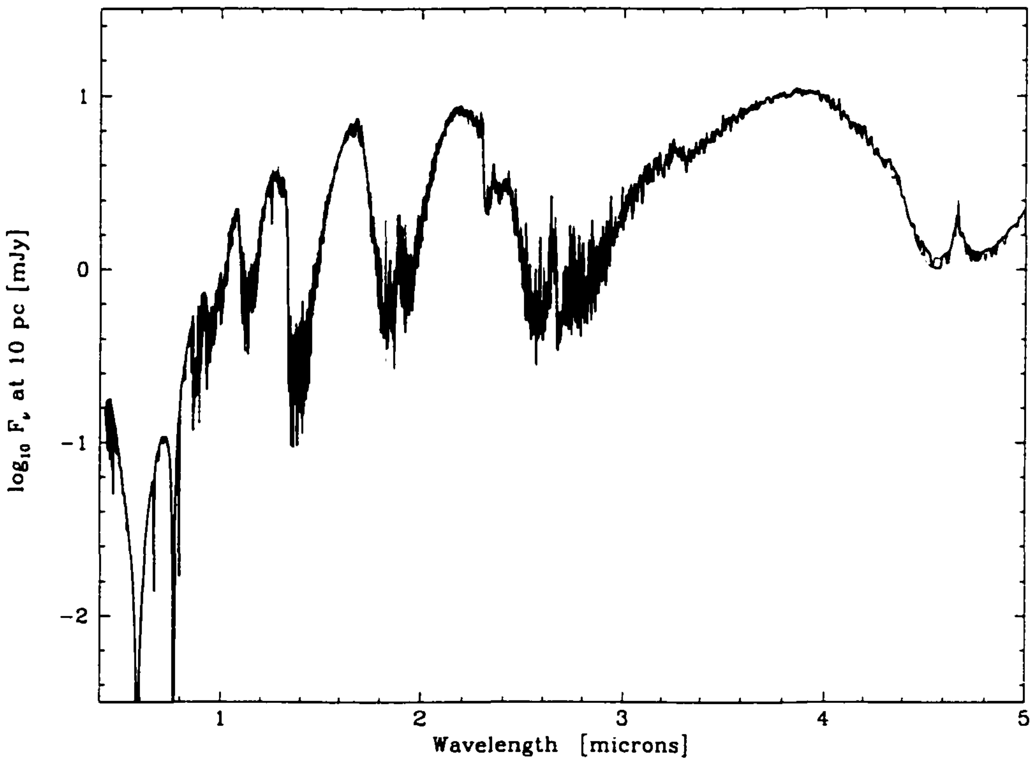

Figure 6.9 Emergent spectrum of a Class IV EGP with its deep silicate cloud (thick curve) relative to that of a cloud-free model (thin curve). Silicate clouds in Class IV EGPs form too deeply to have significant effects on their emergent spectra.

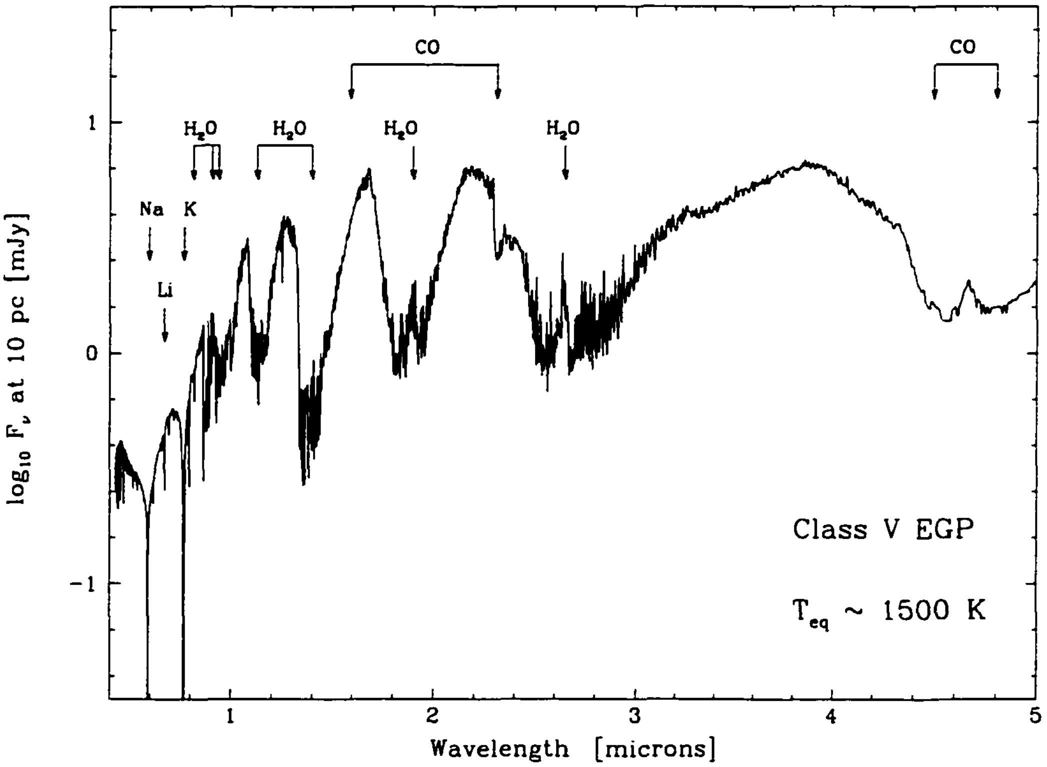

Figure 6.10 Emergent spectrum of a Class V EGP (a "roaster"; ~ 0.05 AU). Like Class IV objects, these EGPs have strong alkali lines, but scattering and absorption by silicate and iron grains high in the atmosphere alter the character of the spectrum. Furthermore, nearly all of the carbon resides in carbon monoxide, so methane features are very weak or nonexistent.

7 SPECIFIC EGP MODELS

Models of specific EGP systems will prove to be invaluable both to inform observational attempts and in the interpretation of the resulting data. Like any subfield of astrophysics, the accuracy and improvement of EGP models will in part depend upon the availability of observational data in order to constrain the rich variety of consistent theoretical models that are possible. At this early stage, assumptions must be made with respect to metallicities, gravities, inner boundary fluxes, cloud scale heights, cloud particle sizes, etc. When modeling a specific EGP system with some well-measured parameters (semimajor axis, stellar spectral type, etc.), I choose one set of values based on the available data, but in Chapter 8 I also explore the effects on the emergent spectra and T-P structures with variation in some of these parameters. As mentioned in Chapter 2, some aspects, such as cloud patchiness and atmospheric winds are not tackled in the current modeling effort.

To date, there are roughly 100 known EGPs. I model a representative sample of these that encompasses a full range of EGP atmospheric temperatures. A broad set of Kurucz model stellar spectra (Kurucz 1994) is utilized to simulate the central stellar spectrum for each planetary system modeled. These spectra were scaled and normalized according to available effective temperatures and gravities of the actual stars (Santos et al. 2001; Ryan 2001).

For the purpose of modeling the atmospheres and emergent spectra of these objects, the mass and age determine the intrinsic luminosity and, hence, the inner boundary flux. Unfortunately, we do not know the actual planetary masses or the ages of most of the systems discovered to date. We do know the minimum planetary masses, as given by the radial velocity method (M$\sin i$), but we do not know the orbital inclination (i) for most systems. Only with a transit (*e.g.* HD 209458b) or an astrometric measurement (*e.g.* ϵ Eridani, preliminary) can we discern the inclination and mass. The ages are difficult as well. Detailed spectroscopy of the central star may result in an estimated age, but such work has yet to be completed for most systems. The inner boundary is of little consequence to the emergent spectra of closely orbiting EGPs so long as the flux corresponds to $T_{\rm eff} \lesssim 500$ K, but it can be quite important in the modeling of planets with larger orbital distances. I use M$\sin i$ and, where available, estimates of the primary's age along with evolutionary models (Burrows et al. 1997) as guides to my chosen inner boundary fluxes. In all cases, I'll state what inner boundary condition was used. Chapter 8 contains a study of the effects of the inner boundary flux on the emergent spectra.

While I do not tackle the complex photochemistry of nonequilibrium species that are likely produced by the ultraviolet irradiation of molecules in the outermost atmospheres of EGPs, I do explore the effects of some such candidate products based on the optical properties of species that were derived experimentally in an attempt to explain the colors of Jupiter and Saturn (Noy et al. 1981; Khare & Sagan 1984; Bar-Nun et al. 1988). Both gaseous and condensed species likely are produced, but the condensates generally will have greater effects on the emergent spectra of EGPs. As in the atmosphere of Jupiter, stratospheric hazes and tropospheric chromophores, or impurities within and above the principal cloud layers, can alter the emergent spectra substantially, particularly in the ultraviolet and blue regions of the spectrum (even if present in relatively small amounts). In §7.7, I detail these effects on Jupiter's albedo spectrum.

7.1. The Upsilon Andromeda System

The Upsilon Andromeda system (Butler et al. 1999) is currently known to be comprised of three EGPs in orbit around an F7 main sequence star of distance $\sim$ 16.5 parsecs. The innermost planet (υ And b) has an $M\sin i$ of $0.71M_J$ and is in a roughly circular orbit ($e \sim 0.03$) about its primary at only 0.059 AU. υ And c is somewhat more massive ($M\sin i = 2.11\ M_J$) and has an elliptical orbit ($e \sim 0.2$) with a semimajor axis of 0.83 AU. With $M\sin i = 4.61M_J$, υ And d is even more massive and has a semimajor axis of 2.50 AU. It has a significant eccentricity of $\sim$ 0.4, so its periastron is actually 1.5 AU and its apastron is 3.5 AU. Since we do not currently know the inclinations of their orbits, we know only the minimum masses of these planets. However, if we assume that the orbits are roughly coplanar, as indicated by our own solar system and theory of planet formation, the ratios of the $M\sin i$ are also the ratios of the planetary masses.

The emergent model spectra for the planets in the Upsilon Andromeda system, along with an estimated spectrum of the primary (a scaled Kurucz model stellar spectrum), are shown in Figure 7.1. An accompanying plot, Figure 7.2, depicts the T-P profiles of these planets.

υ And b is a Class V "roaster" with silicate and iron clouds high in the atmosphere. Using the models of Cooper et al. (2002) as a guide, I choose a cloud particle size distribution that is peaked at 10 microns for both forsterite and iron. Each of these clouds has a vertical extent of one pressure scale height. The iron cloud base resides at $\sim$ 20 mbar, while the forsterite condenses at slightly lower pressures (~10 mbar). Given the prescribed vertical extents of these clouds, they overlap spatially. At pressures where the condensation curves of forsterite and iron are relatively close, as in this case, one might reasonably argue that a number of species from the olivine sequence, in addition to forsterite, could form (as discussed in §3.3). For this fiducial model of υ And b, I do not include such species. The mixing ratio of the condensed forsterite is set equal to the elemental mixing ratio of magnesium ($\sim 3.2 \times 10^{-5}$). Similarly for the iron cloud, the condensate is assumed to consume all the iron (mixing ratio $\sim 5.4 \times 10^{-5}$).

Figure 7.3 is a comparison of a cloud-free version of υ And b (thin curve) with that of my fiducial model (thick curve). Both models have a lower boundary flux equal to that of an isolated object with $T_{\rm eff}$= 500 K and a surface gravity of 3×10^3 cm s^{-2}. The primary effect of removing the clouds is a somewhat lower temperature in the outer atmosphere ($P \lesssim 0.1$ bar) and a slightly hotter atmosphere deeper ($P \gtrsim 0.1$ bar). At large depth, in the convective region ($P \gtrsim 50$ bars), these high clouds appear to have essentially no effect. A comparison of the fiducial spectrum (thick curve) and cloud-free spectrum (thin curve) is depicted in Figure 7.4. The removal of the clouds results in a wider variation from peak to trough throughout most of the spectrum. This is expected to be the case because condensates produce a relatively gray extinction in comparison with strongly wavelength-dependent gaseous absorption. In this same vein, removal of the clouds also deepens the sodium resonance line somewhat.

While the presence of clouds in υ And b (and other roasters) has significant effects on the T-P structure and emergent spectra relative to cloud-free models, these effects are not so drastic as those predicted in hot EGPs by some researchers, such as Barman, Hauschildt, & Allard (2001; hereafter BHA). The main differences are the vertical extent of the clouds and the cloud particle sizes. My clouds have a finite scale height like those observed in Earth's atmosphere and in the atmospheres of other planets in our Solar System. BHA use a "dusty" model in which the condensates extend to the lowest pressure of their atmosphere model, an assumption that was also made by Seager, Whitney, & Sasselov (2000). Furthermore, BHA assume that a large number of condensates form at these very low pressures, including (in addition to forsterite and iron) enstatite, spinel, diopside, akermanite, and others. As detailed in §3.3, some of these species should not form because one or more of their elements will be consumed by a condensate that forms at higher temperature). Furthermore, gravitational settling should prevent any such species from remaining suspended at such low pressures ($\sim$ 1-10 microbars). BHA do suggest that the nature of their spatial treatment of clouds provides an upper limit to the effect of clouds in EGP atmospheres.

The other difference between my cloud layers and those of BHA is approximately two orders of magnitude in the cloud particle sizes. BHA assume an interstellar size distribution, while I use some model results from Cooper et al. (2002) as guide to my chosen fiducial median sizes (10 μm). This choice of particle size is also supported broadly by other recent cloud modeling work (Ackerman & Marley 2001). While the scattering and absorption cross sections as functions of particle size need to be explored by Mie theory (see Chapter 5), a simple geometric argument quickly illuminates the lowest-order changes in opacity: the cross section of a particle of radius a scales as a^2, while its volume scales as a^3. Hence, for a given amount of condensate material, the total opacity will vary roughly as a^{-1}. Due to the strongly wavelength-dependent details of Mie theory, it turns out that this is a very rough approximation, but it is clear that decreasing the particle size by two orders of magnitude can increase the cloud opacity substantially (unless the particles become so small that the Rayleigh scattering limit is approached).

υ And c is a Class III EGP. That is, no principal condensates are expected to appear in its outer atmospherele. Since it is more massive than υ And b, I have chosen a higher surface gravity of 10^4 cm s^{-2}. Using evolutionary models (Burrows et al. 1997) as a guide, I have chosen an inner boundary flux to be equivalent to that of an isolated of object with T_{eff}= 200 K. Its much larger orbital distance and lack of condensates to reflect incident radiation result in a spectrum that is a few-to-several orders of magnitude lower than that of υ And b. However, in the 4-5 μm region, a lack of opacity reduces this difference to only 1-2 dex.

υ And d contains condensed H_2O in the outer atmosphere, and so it is a Class II EGP. It's M$\sin i$ is roughly twice that of υ And c, so I have chosen a surface gravity of 2×10^4 cm s^{-2} and a lower boundary flux of T_{eff}= 250 K. Its semimajor axis is three times that of υ And c, yet its flux at Earth is actually larger at some wavelengths shortward of 2 microns. This due to the fact that scattering by the condensate reduces the depths of the molecular absorption features. In the windows between these features, υ And c still has the higher flux. The rather large eccentricity ($e \sim 0.4$) of υ And d means that its atmospheric temperature will vary from periastron to apastron. At periastron, it is likely that its outer atmospheric temperature will be too high for water to condense, rendering υ And d a Class III object, like υ And c. At apastron, the water clouds of my fiducial model will reside somewhat deeper and will have a greater column depth (i.e. thicker clouds).

Of interest in any observational campaign in which direct detection is desired, Figure 7.5 shows the visible and near-infrared phase averaged contrast between the planetary and stellar fluxes for υ And b, c, and d. This quantity is an average for the planetary flux emerging into all solid angles divided by the stellar flux (uniform in solid angle) at the same distance from the system. In each case, a planetary radius equal to that of Jupiter is assumed. For υ And b, the planet-to-star flux ratio is greater near 4 μm, where it approaches 3×10^{-4}. For comparison, it is worse than 10^{-5} throughout the visible. For υ And c and d, the planet-to-star flux ratio is greatest in the $\sim$ 4.1 to 4.8 μm range, where it is $\sim 10^{-5}$ and 3×10^{-6}, respectively. Elsewhere, it is below 10^{-6} (below 10^{-8} throughout most of the visible). Since these numbers are based on a phase-averaged ratio, they are a bit pessimistic compared with what one would expect to observe at full phase, which could improve the ratios by over a factor of two, depending upon the details of the planetary phase function (Seager et al. 2000).

7.2. The Transiting Planet, HD 209458b

HD 209458b was discovered by the usual radial velocity method (Henry et al. 2000; Mazeh et al. 2000) to have an orbital distance of only 0.045 AU ($e \approx 0$) about a G0V star, but subsequent dramatic photometry (Charbonneau et al. 2000; Henry et al. 2000) revealed that it transits its primary. At the time of this writing, HD 209458b is still the only transiting EGP certain to exist (there are several candidates currently under analysis). But such an event should not be a very rare occurrence, at least for Class V roasters. A transit will be observed if the inclination of a planet's orbit is greater than $\cos^{-1}[(R_* + R_p)/a]$, where R_* is the stellar radius, R_p is the planetary radius, and a is the orbital distance of the planet. Depending on the details of the system, a transit should be observed for roasters with orbital inclinations greater than $\sim$ 84 degrees. Assuming a random distribution of orbital inclinations, a transit should occur for approximately 10% of these systems. This prediction is based upon the fact that the probability of a given orientation per solid angle is constant. So the integrated probability for a system being between 0 and i degrees (P[0°,i]) is just 1-cos$i$, while P[i,90°] = cos$i$, and cos(84°) $\simeq$ 0.1. Of course, such a fortunate orientation immediately reveals the mass of the planet. A good estimate of the radius of the planet can be obtained from the photometric transit depth, since the percentage decrease in the stellar flux is approximately given by $(R_p/R_*)^2$. (A more detailed analysis may take account of the ingress and egress.) Given the mass and radius of the planet, its surface gravity is inferred. With a mass of $0.69\mathrm{M_J}$(Mazeh et al. 2000; Cody & Sasselov 2002) and a radius of $1.35\mathrm{R_J}$, HD 209458b has a surface gravity of $\sim$ 980 cm s^{-2}.

A Class V roaster, the atmosphere of HD 209458b is expected to have high silicate and iron clouds with bases at $\sim$ 5-10 mbar. My fiducial model has a surface gravity of 980 cm s^{-2} and an inner boundary flux corresponding to $\mathrm{T_{eff}}$= 500 K. Figure 7.6 depicts the model spectrum along with an estimated spectrum of the primary (a scaled Kurucz model). Figure 7.7 shows the T-P profile of HD 209458b, and the phase averaged planet-to-star flux ratio is depicted in Figure 7.8. As with υ And b, this ratio is largest near 4 μm, where for HD 209458b it approaches 10^{-3}. The sodium and potassium absorption keeps the ratio low in the visible, but between the resonance lines ($\sim$ 0.7 μm) the ratio is approximately 3×10^{-5}, as it is blueward of the sodium line near 0.4 μm. One caveat is that nonequilibrium photochemical products tend to absorb strongly in the ultraviolet and blue regions of the spectrum (e.g. Jupiter), so the contrast at such short wavelengths is quite uncertain for HD 209458b and other roasters.

Recent landmark observations of the HD 209458b transit by Charbonneau et al. (2002) in the vicinity of the sodium resonance doublet revealed a photometric dimming of this region of the spectrum relative to adjacent bands. This has been interpreted as the first detection of sodium in the atmosphere of an EGP (and, importantly, the first detection of an EGP atmosphere) and it is in general accord with theoretical predictions (Hubbard et al. 2001). However, the level of absorption inferred is less than one would expect from basic theoretical models assuming a solar abundance of sodium in neutral form. A few possible explanations have surfaced, including the existence of a cloud layer at very low pressure, ionization of sodium by radiation from the primary (Fortney et al. 2002), or non-LTE effects in the outermost atmosphere.

Barman et al. (2001) champion the non-LTE explanation. They hypothesize that a reduction in photon absorption in the resonance doublet of neutral sodium occurs, not because there is a lower than expected sodium abundance, but because the level populations of sodium deviate from the Saha-Boltzmann distribution. While this is a plausible explanation in principle, it requires shielding of the neutral sodium from the intense ultraviolet irradiation, which in turn requires a strong ultraviolet absorber high in the atmosphere. Without such an absorber, the incident irradiation could ionize beyond the Barman et al. outer non-LTE region, eliminating their effect. In their model, heavy metals such as Mg, Ca, and Al exist in gaseous form in the outermost atmosphere to provide the necessary shielding. Their justification of the existence of these gases at such low pressure is their particularly hot T-P profile, which is above the condensation temperatures of forsterite, enstatite, gehlenite, and other species that will consume these metals if the outer atmosphere is somewhat cooler. In fact, my fiducial model for HD 209458b is several hundred degrees Kelvin cooler in the outermost atmosphere, indicating the likelihood that the elevated temperature of the Barman et al. is produced by the same heavy metals that are providing their shielding. Using abundances that account for the condensation and rainout of such species, the outer atmosphere should be clear of these metals. In addition to my model results, work by others on close-in EGPs (Seager et al. 2000; Goukenleuque et al. 2000) does not reproduce the Barman et al. atmospheric temperatures or compositions.

A more natural explanation of the Charbonneau et al. (2002) observational result is the photoionization of sodium in the outer atmosphere of HD 209458b. As outlined in §3.5, such ionization may occur down to $\sim$ 1 mbar near the limb of the planet. Treating this problem with the correct spherical geometry, and including the opacities of the high forsterite cloud, this is deep enough in the atmosphere to account for the reduction in flux observed by Charbonneau et al. (Fortney et al. 2002).

7.3. Orbiting a Cool Star: The GJ 876 System

The GJ 876 system (a.k.a. Gliese 876; Marcy et al. 1998; Delfosse et al. 1998) is comprised of two planets orbiting at 0.13 AU and 0.21 AU about a late main sequence star of spectral type M4. The more massive and first of the two planets discovered, GJ 876 b ($M\sin i = 1.89 M_J$), has the wider orbit (with $e \approx 0.10$), while GJ 876 c ($M\sin i = 0.56 M_J$) has the more eccentric orbit ($e \approx 0.27$).

GJ 876b and c are both Class III planets because their temperatures are too cool for a silicate layer to appear in the troposphere, but too hot for H_2O to condense. The result of such a "clear" atmosphere is a strongly wavelength-dependent emergent spectrum, which is governed largely by the gaseous molecular absorption bands of water, methane, and ammonia. Given their similarities in composition, GJ 876b and c are expected to have very similar spectra. The factor of $\sim$ 3 difference in their $M\sin i$ implies somewhat different surface gravities and lower boundary fluxes, but both objects are close enough to their star that the

T-P structure in their outer atmospheres is determined more strongly by the stellar irradiation than by their intrinsic luminosities.

For GJ 876b, I use an inner boundary flux corresponding to T_{eff}= 150 K and a surface gravity of 6 × 10^3 cm s^{-2}. For GJ 876c, I use an inner boundary flux of T_{eff}= 100 K and a surface gravity 1/3 that of GJ 876 b, or 2 × 10^3 cm s^{-2}. The emergent spectra of the two planets, along with an estimated spectrum of the primary (a scaled Kurucz model stellar spectrum), are shown in Figure 7.9. An accompanying plot, Figure 7.10, depicts the planetary T-P profiles. Given their similarities in composition, GJ 876b and c are expected to have very similar emergent spectra. One caveat is that, while the T-P profile of GJ 876b never crosses the water condensation curve, it does come within ∼ 10 K of it near about 1 mbar. Given a somewhat lower incident irradiation than that of my scaled Kurucz model for GJ 876, or given an observation of GJ 876 b at apastron, some water condensation may occur in its outermost atmosphere, rendering it a Class II EGP. However, I retain the Class-III designation for my fiducial model of GJ 876 b for its given semimajor axis and any reasonable range in surface gravity or lower boundary flux.

Figure 7.11 depicts the phase-averaged planet-to-star flux ratios for GJ 876b and c. For both planets, this ratio peaks near 4.4 μm, where it reaches a value of $\sim 10^{-5}$. In contrast, in the visible region, the M-dwarf stellar flux overpowers that of either planet by a factor of at least 10^8.

7.4. 51 Pegasi b and Tau Bootes b

In 1995, Mayor & Queloz discovered the first EGP, 51 Pegasi b ($M\sin i = 0.45\ M_J$), via the radial velocity method. The discovery of such a planet around another star would alone cause a great deal of excitement in the astronomical community, but the fact that its orbital period was only 4.23 days at a minuscule 0.05 AU was nothing less than astonishing. Perhaps the fact that this planet orbited a solar-type star made the observation even more dubious to some. After all, this is a much different beast than the giant planets of the Solar System we know. Scrutiny of this and subsequent similar discoveries has come and gone. The 51 Peg b observation is not due merely to non-radial stellar pulsations (Gray 1997; Gray & Hatzes 1997), nor is the radial velocity variation due to a nearly face-on orbit of two identical stars (Black & Stepinski 2001; Stepinski & Black 2001). And although 51 Peg b remains to be detected *directly*, most everyone in the astronomical community now accepts it and the other roasters as a bona fide planets. (The transit observation of the subsequent and similar HD 209458b system convinced most researchers.)

The τ Boo system (Butler et al. 1997) gained popularity when Cameron et al. (1999) claimed a detection in reflected light near 0.48 μm. This detection was not confirmed by another group, Charbonneau et al. (2000), who constrained the albedo to be low in this region ($\lesssim$ 0.3 assuming a phase function and a highly inclined orbit). If Cameron's detection were true, τ Boo b would have to have had an albedo as high as Jupiter in this region and a troubling radius of $\sim$ $1.8\mathrm{M_J}$—troubling because such a large radius would be well out of bounds relative to theoretical models for a high gravity planet (Guillot et al. 1996; Burrows et al. 2000b). This detection was later retracted by the authors, but τ Boo b remains a particularly interesting object because, with $\mathrm{M}\sin i = 4.14\mathrm{M_J}$, it is much more massive than most of the other roasters known.

Since they orbit their primaries so closely, 51 Peg b and τ Boo b are both Class V roasters, but these systems do differ. 51 Peg b orbits a G2-2.5V Sun-like star at 0.05 AU, while τ Boo b orbits a hotter F7V star at 0.046 AU. Additionally, their projected masses differ by about a factor of 10.

As the prototype EGP, 51 Peg b has been modeled by a number of researchers (Seager & Sasselov 1998; Goukenleuque et al. 2000; BHA), and the model T-P structures and emergent spectra vary considerably. In all cases, a self-consistent planar atmosphere code is used. Perhaps the greatest difference is between the models of Goukenleuque et al. and BHA. Specifically, BHA's atmospheric temperature at P = 1 mbar is above 1650 K ("AMES-Cond" model; cloud-free), while that of the most analogous Goukenleuque et al. model is under 900 K. At P = 1 bar, the temperature of the BHA model is $\sim$ 2000 K, while that of Goukenleuque is $\sim$ 1400 K. To first order, this difference can be explained by the fact that Goukenleuque et al. redistribute the incident energy per second over the surface of the full sphere (weighting the incident flux by a factor of 1/4, as described in Chapter 2), while BHA treat only the substellar point of the planetary atmosphere (no weighting of the incident flux).

In order to investigate the dependence of the T-P structure using my own models, I ran a cloud-free 51 Peg b model with no flux weighting, one with a weighting of 1/4, and one with a weighting of 1/2. The flux weighting of 1/2 corresponds to the irradiation of the day-side hemisphere only, the default weighting used in the present work. The resulting T-P profiles are depicted in Figure 7.12. For my 1/4-weighted model, the atmospheric temperature at 1 mbar is 965 K, and at 1 bar it is 1830 K. For my unweighted model, the temperature at 1 mbar is 1390 K, and at 1 bar it is 2370 K. So for my models, this difference in the flux weighting results in a 35% difference in the temperature at 1 mbar and a 25% difference at 1 bar. The difference between the Goukenleque et al. and BHA models at 1 mbar is 60%. while at 1 bar this difference is a more modest 35%. Hence. while differences in the incident flux weighting can in part explain the T-P structure differences in the models of the various researchers. this is certainly not a complete explanation. Other less obvious differences must exist as well, such as atmospheric composition. opacities. incident flux (beyond the weighting issue). or the inner boundary condition implemented.

My fiducial model of 51 Peg b has a silicate (forsterite) cloud base at 20 mbar and an iron cloud base at 30 mbar. I assume a cloud height of one pressure scale height. an inner boundary flux of T_{eff}= 500 K, and a low surface gravity of 10^3 cm s^{-2}, due to the small M$\sin i$ ($0.45M_J$) of 51 Peg b. In order to achieve numerical convergence of the 51 Peb b model. I found it necessary to attenuate the clouds to 10% of the elemental iron and magnesium abundances. This should be taken into account when comparing the T-P structure and emergent spectrum of 51 Peg b with those of other roasters, for which such an adjustment to the condensate concentration has not been made.

Tau Boo b (Butler et al. 1997) orbits at only 0.046 AU from a hot F7 main sequence star. For my fiducial τ Boo b model. I use a surface gravity of 10^4 cm s^{-2} (an order of magnitude larger than that used for 51 Peg b) and an inner boundary flux of T_{eff}= 500 K. As can be seen in Figure 7.13. the T-P profiles of τ Boo b (both with and without clouds) and 51 Peg b are fairly similar, especially considering their very different surface gravities and primary spectral types. This can be explained quite simply: The same object orbiting a hotter star naturally would have a higher temperature at a given pressure. but on the other hand, hydrostatic equilibrium dictates that pressure increases with surface gravity. So in this case, the two effects work against each other, resulting in T-P profiles that are actually closer to each other in some regions than they would be if either the surface gravities of the two planets were the same, or if the planets orbited similar stars. Gravity and temperature also have implications for the positions of cloud decks in these and other atmospheres. A cloud deck will reside deeper in an atmosphere as surface gravity increases, but higher in an atmosphere with increasing temperature. For 51 Peg b and τ Boo b, the profiles are so close that they are coincident with the condensation curves at essentially the same pressures. As a result, these planets should condense clouds at very similar atmospheric pressures.

The atmosphere model of τ Boo b is particularly interesting because it has a convection zone at low pressures, toward the top of the forsterite cloud around 10 mbar. This is the only such model for which such a low-pressure convective region has resulted, and it persists with either fine or coarse zoning within the cloud region. The strong incident flux from the primary (F7V at 0.046 AU) in combination with the opacity of the forsterite cloud results in a steep temperature gradient and, hence, the onset of convective energy transport, as depicted by the dashed portion of the T-P profile of τ Boo in Figure 7.13. The model spectra of τ Boo b and 51 Peg b are shown in Figure 7.14, and the planet-to-star flux contrasts are depicted in Figure 7.15.

7.5. The 55 Cancri System and its New Long-Period Planet

The 55 Cancri system is made up of at least two EGPs orbiting a G8 main sequence star. The inner planet (Butler et al. 1997) has a nearly circular orbit ($e \approx 0.03$) at 0.11 AU, with M$\sin i$ = 0.84M$_J$. The recently discovered outer planet (Marcy et al. 2002) is the first EGP found to orbit its primary at a distance greater than Jupiter's distance from the Sun. This object has a semimajor axis of $\sim$ 5.5 AU, an eccentricity of 0.16, and Msin$i$ of 4.0M_J. The outer object has been designated, 55 Cancri d (rather than c), because judging by the radial velocity residuals, a third planet of sub-Jupiter mass may exist at 0.24 AU. Currently, Marcy et al. consider the existence of this third planet to be a good possibility, but not a firm detection because the additional periodicity may be due to rotating inhomogeneities on the stellar surface.

55 Cancri b is a Class IV planet. My fiducial model of this EGP assumes a surface gravity of 3×10^3 cm s^{-2} and an inner boundary flux of $T_{\rm eff}$= 500 K. A silicate cloud resides at depth, with a base at 20 bars and a vertical extent of one pressure scale height. As detailed in §6.4, this deep cloud does not have a significant effect on the emergent visible and near-infrared spectrum of 55 Cnc b.

55 Cancri d is a Class II object. One might estimate that, with an orbital distance greater than that of Jupiter and a primary cooler than our Sun, 55 Cnc d would be a Jovian-like Class I object with ammonia clouds. However, because of its large minimum mass, such a planet will be intrinsically hotter than Jupiter, even for a relatively late age (Burrows et al. 1997). Even with a conservative inner boundary flux corresponding to $T_{\rm eff}$= 150 K, the atmosphere of 55 Cnc d is too warm for ammonia to condense.

Figure 7.16 depicts the spectra of 55 Cnc b and d. An accompanying plot, Figure 7.17, shows the T-P profiles of these planets. The Class IV designation of 55 Cnc b is clear due to its strong sodium and potassium resonance features and the methane absorption at 3.3 μm. The spectrum of 55 Cnc d exhibits strong molecular absorption features in the visible and near-infrared, but a water cloud between $\sim$ 0.6 and 1.6 bars (one pressure scale height) reduces their strengths considerably. Note that this water cloud is deeper and more optically thick than that of υ And d

(§7.1) simply because the T-P profile of 55 Cnc d intersects the water condensation curve at significantly higher pressure. However, whether a water cloud is high and optically thin or relatively deep and optical thick, the basic result of an elevated visible and near-infrared spectrum holds.

Figure 7.18 shows the phase-averaged planet-to-star flux ratios for 55 Cnc b and d out to 30 microns. 55 Cnc d has an unusually large angular separation from its primary of $\sim 0.45''$, making it an enticing candidate for direct detection. A good bet may be between 4.2 and 4.8 μm, where there is little opacity and the planet-to-star flux ratio is better than 10^{-6}. Between $\sim$ 5 and 6 μm, the methane, water, and ammonia opacities strengthen, but beyond a strong methane band between $\sim$ 7 and 8 μm, the planet-to-flux ratio improves substantially. There are a number of striking differences between 55 Cnc b and d. In the visible region, the strong sodium and potassium lines of 55 Cnc b contrast with the methane-dominated spectrum of 55 Cnc d, whose continuum is provided by both Rayleigh scattering and scattering off condensed H_2O. In the near-infrared, the troughs and peaks of 55 Cnc d (due to gaseous H_2O and methane) vary more widely than those of 55 Cnc b. This effect can be explained largely by H_2O opacity differences at high and low temperatures, revealed by quick comparison of Figures 4.3 and 4.4. Additionally, the methane opacity is stronger in the lower temperature 55 Cnc d due to a higher equilibrium abundance of this molecule. Between $\sim$ 4 and 5 microns, CO opacity in 55 Cnc b closes the gaping opacity window seen in this region of the 55 Cnc d spectrum. Toward longer wavelengths, the 55 Cnc d planet-to-star flux ratio continues to increase, while that of 55 Cnc b is fairly flat.

7.6. Some Other EGPs of Interest

In addition to the systems chosen above, many more deserve specific attention due to their interesting orbital parameters, masses, primaries, and/or proximity. I model a few of these in the present work, including HD 114762b, ϵ Eridani b, and HD 83443 b.

The massive HD 114762 b (Latham et al. 1989) is often referred to as a brown dwarf, not a planet. It has a projected mass of $11 M_J$(Marcy et al. 1998), and its mass has been estimated to be as high as $145 M_J$(Han et al. 2001), which of course would make this object a low-mass star, but this result is quite controversial. Whatever its mass, HD 114762b orbits its F9V primary at a distance of $\sim$ 0.3 AU with an eccentricity of 0.335. Due to the unconstrained mass of this object (at the high end), I model HD 114762b with a range of inner boundary fluxes and surface gravities informed by evolutionary models of isolated objects (Burrows et al. 1997). Figure 7.19 depicts the visible emergent spectra for four different models of HD 114762b. From top to bottom near the Na-D line (or bottom to top near 1 μm) the inner boundary fluxes (in terms of $T_{\rm eff}$) and surface gravities of the models are 300 K, 3×10^4 cm s^{-2}; 500 K, 10^5 cm s^{-2}; 700 K, 2×10^5 cm s^{-2}; and 1000 K, 3×10^5 cm s^{-2}. Note that a transition from a Class III object to a Class IV object takes place between the last two models. I expect that HD 114762b is a Class III object unless its mass is over $\sim$ 60 M_J, in which case it clearly should be called a brown dwarf rather than a planet. The spectrum out to 5 μm of my fiducial HD 114762b model (inner boundary flux of 500 K, surface gravity of 10^5 cm s^{-2}) is shown in Figure 7.21.

Epsilon Eridani is a controversial, but potentially very important, EGP because of its wide orbit around a star that is only 3.2 parsecs away from Earth.

If it is real. its separation from its K2V primary is $\sim$ 1 arcsecond, significantly larger than that of any other system. The radial velocity detection of ϵ Eri b (Hatzes et al. 2000) is considered marginal by many, but its orbital parameters are M$\sin i$ = 0.86 M_J, a = 3.3 AU, and $e \sim 0.61$, a very eccentric orbit. This system is probably under 1 Gyr of age (Greaves et al. 1998), indicating that ϵ Eri b is quite a bit warmer than Jupiter if its mass is $\sim 1M_J$. Indeed. an astrometric study claimed a mass of 1.2 ±0.33 M_J(Gatewood 2000). Using a fiducial lower boundary flux corresponding to T_{eff}= 170 K and a gravity of 3×10^3 cm s^{-2}. ϵ Eri b is a Class II EGP. The resulting spectrum from 0.4 to 30 μm is shown in Figure 7.20. A water cloud resides at $\sim$ 1 bar pressure in ϵ Eri b's atmosphere. but given the large eccentricity of this EGP, the cloud will be higher in the atmosphere at apastron and deeper at periastron. Even at apastron, it is unlikely that the atmospheric temperature will be quite low enough for ammonia to condense. In fact, an atmosphere model for ϵ Eri b at 5.3 AU indicates that the T-P profile falls just short of the ammonia condensation curve.

HD 83443 b (Mayor et al. 2000) is a Saturn-mass (M$\sin i$ = 0.35M_J) planet with the smallest orbital distance of any EGP known to date. However, unlike most known roasters, HD 83443b orbits a later-type main sequence star (K0V). Therefore, despite its status as the most closely-orbiting roaster, it is a little cooler than its brethren. Because it is cooler, its silicate and iron clouds are somewhat deeper than in most roasters. In my fiducial model, the silicate (forsterite) cloud resides at $\sim$ 30 mbar and an iron cloud is located near 0.1 bar. I use a lower boundary flux corresponding to T_{eff}= 500 K and a gravity of 900 cm s^{-2}. Initially, due to radial velocity residuals, this system was believed to have another planet orbiting at 0.174 AU, with M$\sin i$ = 0.17M_J. However, follow-up measurements failed to reveal such a planet (Bulter et al. 2002).

Figure 7.21 depicts the visible and near-infrared spectra of HD 83443b, HD 114762b, and ϵ Eri b. The T-P profiles for each of these objects are given in Figure 7.22.

7.7. Jupiter and Jovian-Class Planets

Jupiter is important both as a testbed for the theory of giant planet atmospheres and as a representative for Class I EGPs. Accurate full-disk geometric albedo spectra of Jupiter have been obtained (Karkoschka 1994; Karkoschka 1998), and space-based and ground-based studies have provided a fair amount of information concerning Jupiter's atmosphere. I model the full-disk albedo spectrum of Jupiter in order to compare with the Karkoschka geometric albedo spectrum and the published Bond albedo of 0.343 (Hanel et al. 1981).

Before getting to the specifics of Jupiter's atmosphere, it will be useful to review the theory of albedos. While the albedo of an object refers generally to the fraction of light that the object reflects, the *geometric* albedo refers specifically to the reflectivity of the object at full phase ($\Phi = 0$, where Φ represents the object's phase angle) relative to that of a perfect Lambert disk of the same radius under the same incident flux. Since planets are essentially spheres, the factor projecting a unit surface onto a disk orthogonal to the line of sight is given by $\cos\phi\sin\theta$, where ϕ is the object's longitude (defined to be in the observer-planet-star plane) and θ is its polar angle ($\frac{\pi}{2}$ - latitude). The geometric albedo is given by integrating over the illuminated hemisphere:

$$A_g = \frac{1}{\pi I_{inc}} \int_{\phi=-\frac{\pi}{2}}^{\frac{\pi}{2}} \int_{\theta=0}^{\pi} I(\phi, \theta, \Phi = 0) \cos\phi \sin\theta d\Omega \,, \tag{7.1}$$

where I_{inc} is the incident specific intensity, πI_{inc} is the incident flux, and $I(\phi, \theta, \Phi = 0)$ is the emergent intensity. More generally, $I = I(\phi, \theta, \Phi; \phi_0, \theta_0)$, but at full phase all incident angles (ϕ_0, θ_0) are equal to the emergent ones.

The *spherical* albedo, A_s, refers to the fraction of incident light reflected by a sphere at all angles. Stated as a function of wavelength, it is obtained by integrating the reflected flux over all phase angles. The flux as a function of phase angle ($F(\Phi)$) is given by the more general form of Eq. (7.1). Assuming unit radius (Chamberlain & Hunten 1987),

$$F(\Phi) = \int_{\phi=\Phi-\frac{\pi}{2}}^{\frac{\pi}{2}} \int_{\theta=0}^{\pi} I(\phi, \theta, \Phi; \phi_0, \theta_0) \cos\phi \sin\theta d\Omega. \tag{7.2}$$

The spherical albedo is obtained by integrating $F(\Phi)$ over all solid angles:

$$A_s = \frac{1}{\pi I_{inc}} \int_{4\pi} F(\Phi) d\Omega = \frac{2}{I_{inc}} \int_0^{\pi} F(\Phi) \sin\Phi d\Phi. \tag{7.3}$$

Note that the spherical and geometric albedos are related by $A_s = A_g q$, where

$$q = \frac{2}{F(\Phi = 0)} \int_0^{\pi} F(\Phi) \sin\Phi d\Phi \tag{7.4}$$

is known as the phase integral.

The important *Bond* albedo, A_B, is the ratio of the total reflected and total incident powers. It is obtained by weighting the spherical albedo by the spectrum of the illuminating source and integrating over all wavelengths:

$$A_B = \frac{\int_0^{\infty} A_{s,\lambda} I_{inc,\lambda} d\lambda}{\int_0^{\infty} I_{inc,\lambda} d\lambda}, \tag{7.5}$$

where the λ subscript signifies that the incident intensity varies with wavelength.

The asymmetric Feautrier albedo code (§2.2) produces the spherical albedo, due to an equivalence between uniform planar radiation onto a unit sphere and uniform radiation from 2π steradians onto a plane with unit area. From the spherical albedo, I derive the geometric and bond albedos.

With the above definitions out of the way, let us review the basics of the Jovian atmosphere. At visible and near-infrared wavelengths, Jupiter's upper troposphere and stratosphere shape its albedo spectrum. According to the standard model, a somewhat heterogeneous cloud deck extends from ~ 0.3 to 0.7 bars in the troposphere (West et al. 1986; Griffith et al. 1992). Although the bulk of the cloud deck consists primarily of particles at least 10 μm in size, a layer of smaller particles (~ 0.5–1.0 μm) resides near the cloud tops (West et al. 1986; Pope et al. 1992). Beneath this upper cloud deck is a NH_4SH and NH_3 cloud layer at ~ 2–4 bars, and an H_2O cloud condenses somewhat deeper. Above the NH_3 cloud deck, a stratospheric haze resides at pressures near ~ 0.1 bar. It is worth mentioning that the Galileo probe results deviated from this standard model. One difference relevant to the albedo and reflection spectra is a tropospheric haze inferred from the probe data, likely composed primarily of NH_3, above a somewhat deeper NH_3 cloud deck (Banfield et al. 1998), but it is not known whether the probe entry location is characteristic of the planet as a whole.

In addition to H_2, abundant gaseous species in the upper troposphere include He and CH_4, with mixing ratios relative to H_2 of 0.156 and $\sim 2.1 \times 10^{-3}$, respectively (Niemann et al. 1996). Gaseous NH_3, H_2O, H_2S, and PH_3 are present in small mixing ratios.

It has been suggested that the color differences of Jupiter's belts and zones are largely due to the visibility of chromophores residing within the NH_3 cloud deck (West et al. 1986). No appreciable altitude differences between the belts and zones are found, although the zones likely contain thicker upper cloud and/or haze layers than the belts (Chanover et al. 1997; Smith 1986). Jupiter's ultraviolet/blue albedo is depressed substantially from what one would expect from the increase with frequency of the Rayleigh scattering cross sections. and Raman scattering cannot account for the albedo in this wavelength region. This depressed UV/blue albedo likely is produced by the large imaginary refractive indices of the tropospheric chromophores and, to a lesser degree, stratospheric aerosols (West et al. 1986).

Due to the large optical depth of Jupiter's upper ammonia cloud deck at visible and near-infrared wavelengths, a two-cloud model of the atmosphere suffices (West 1979; Kuehn 1993). I model the top of the upper cloud deck (~ 0.35 bar) with a "cloud" distribution (§5.3) peaked at 0.5 μm. Deeper in the cloud, from 0.45 to 0.7 bar, a particle distribution peaked at 30 μm is used. This size distribution is also used in the lower cloud, spanning from 2 to 4 bars.

In addition to NH_3 condensation, a small mixing ratio of a chromophore, either tholin (2×10^{-8}) or P_4 (5×10^{-9}), is added to the upper cloud. As inferred from limb darkening observations, the condensed chromophore becomes well mixed in the upper ammonia cloud, and perhaps deeper as well (West et al. 1986; Pope et al. 1992). As per Noy et al. (1981), the peak of the chromophore particle size distribution is set to 0.05 μm. However, the nature of the size distribution and whether the chromophore adheres to the ammonia ice particles are as yet unclear.

Gaseous abundances are modeled using the Galileo Probe Mass Spectrometer values (Niemann et al. 1996) as a guide. The H_2, He, and CH_4 abundances are taken directly from the Probe results. However, the tropospheric NH_3 abundance varies considerably with depth. At ~ 0.4 bar, its mixing ratio has been found to be $\sim 5 \times 10^{-6}$ (Griffith et al. 1992; Kunde et al. 1982), while at ~ 0.7 bar, its mixing ratio is $\sim 5 \times 10^{-5}$ to 10^{-4}. In an infrared study using Voyager IRIS data (Gierasch et al. 1986), it was found that only a small fraction ($\sim 1\%$) of the ammonia is in condensed form. Based on my visible albedo modeling, where the smaller particle size distribution dominates, and using the gaseous NH_3 mixing ratios above. I find that a condensation fraction of $\sim$ 5% in the upper cloud is required to provide the necessary reflectance.

I model Jupiter's stratospheric haze using Deirmendjian's "haze" particle size distribution (§5.3) of polyacetylene peaked at 0.1 μm—a particle size justified by limb darkening studies (Rages 1997; West 1998; Tomasko et al. 1986). The abundance of C_2H_2 in Jupiter's stratosphere is $\sim 10^{-8}$ to 10^{-7} (Edgington et al. 1998; Noll et al. 1986), though the abundance of the polymerized variant is not known. In this study, the polyacetylene mixing ratio is set to 5×10^{-8}, in a haze layer from 0.03 to 0.1 bar.

Figure 7.23 shows two model geometric albedo spectra along with the observed full-disk albedo spectrum of Jupiter (Karkoschka 1994). I convert my model spherical albedo to a geometric albedo using an averaged phase integral of q = 1.25 (Hanel et al. 1981). The upper model utilizes tholin as the chromophore throughout the upper ammonia cloud deck, while the lower model utilizes P_4.

Although the general character of Jupiter's geometric albedo is reproduced fairly well, many of the methane absorption features are modeled too deeply. Furthermore, the gaseous ammonia features at $\sim$ 0.65 μm and 0.79 μm do not appear in the models because the database used does not include ammonia absorption shortward of $\sim$ 1.4 μm. Karkoschka (1998) indicates that the absorption feature centered at $\sim$ 0.93 μm may be due to ammonia as well. Relying upon Mie scattering theory and my choices for chromophore particle size distributions, tholin appears to reproduce the UV/blue region of the albedo better than P_4. However, the actual chromophore(s) in Jupiter's atmosphere remains a mystery.

The published Bond albedo of Jupiter is 0.343 (Hanel et al. 1981). Using my model and limited wavelength coverage (0.3 μm to 2.5 μm). I derive a Bond albedo of 0.42-0.44—a fair approximation—depending upon whether P_4 or tholin is used as the chromophore.

Uncertainties in the vertical structure of Jupiter's atmosphere, heterogeneities in Jupiter's cloud layers, and my use of an averaged phase integral all likely play a role in explaining the differences between observational and modeled albedo spectra. These details aside, Jupiter's atmosphere remains a useful benchmark for EGP modeling.

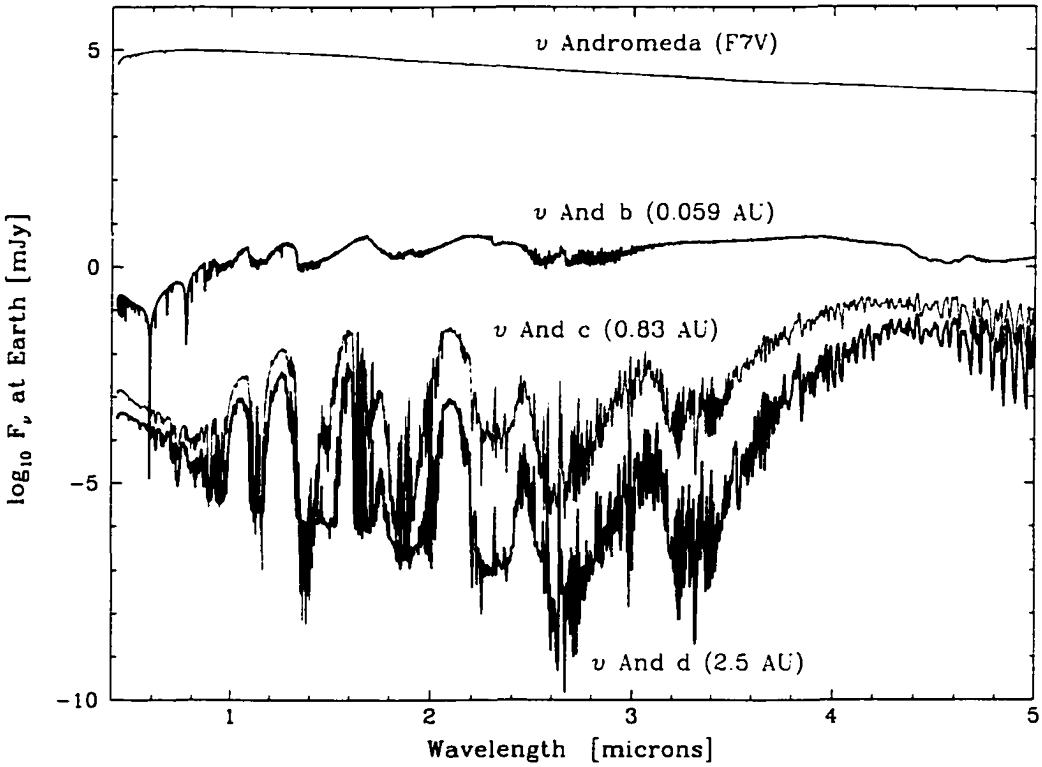

Figure 7.1 Visible and near-infrared spectra of υ And b, c, and d. An estimated spectrum of the primary (a scaled Kurucz model) is also depicted. υ And b, c, and d are Class V, III, and II EGPs, respectively.

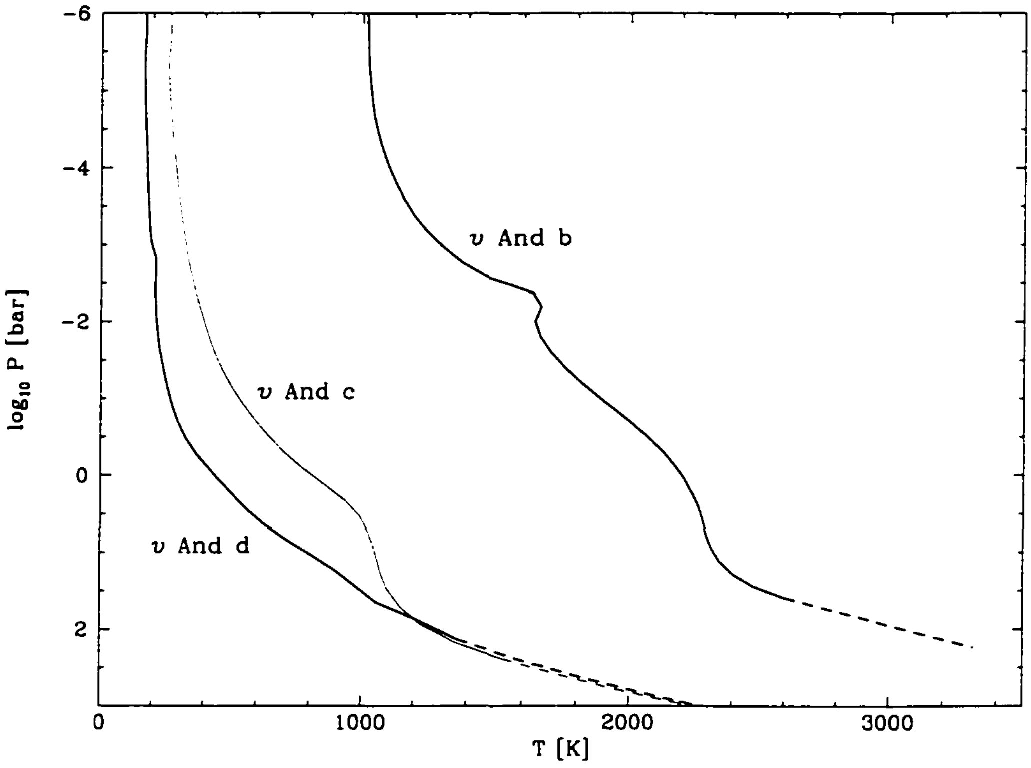

Figure 7.2 T-P profiles of υ And b, c, and d. The dashed portions of the profiles indicate convective regions.

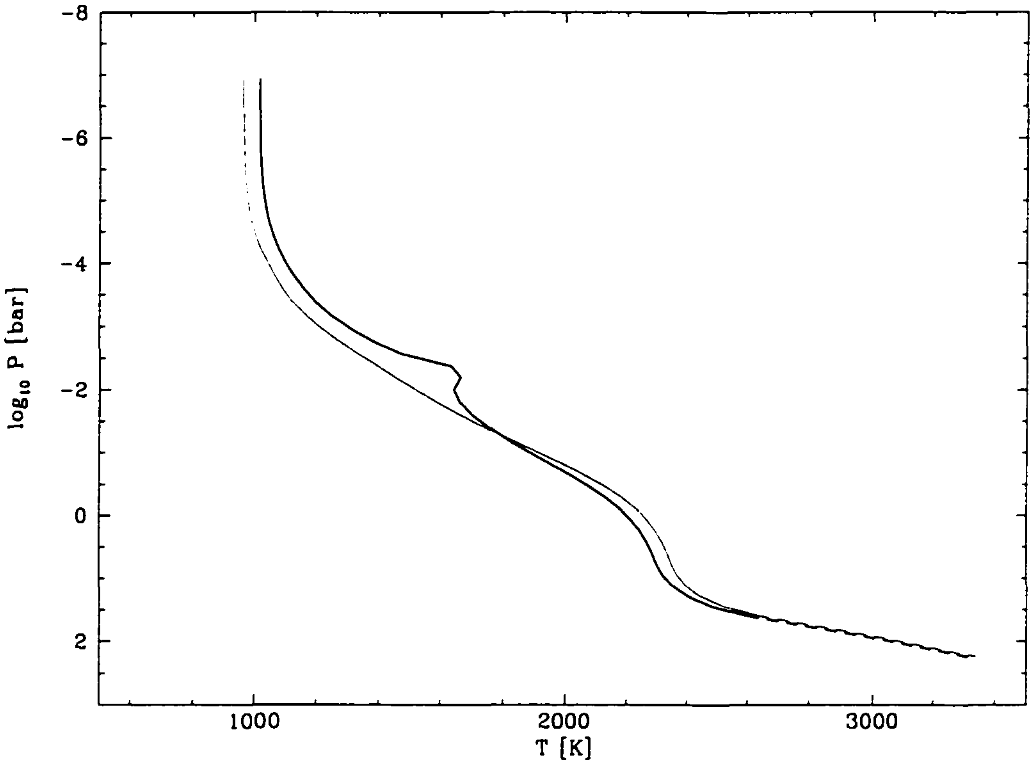

Figure 7.3 Fiducial T-P profile of υ And b (thick curve) versus that of a cloud-free model (thin curve). Removing the iron and silicate clouds results in a cooler outer atmosphere, but a hotter deeper atmosphere. At large pressures ($\gtrsim$ 50 bars), the high clouds appear to have essentially no effect on the T-P profile.

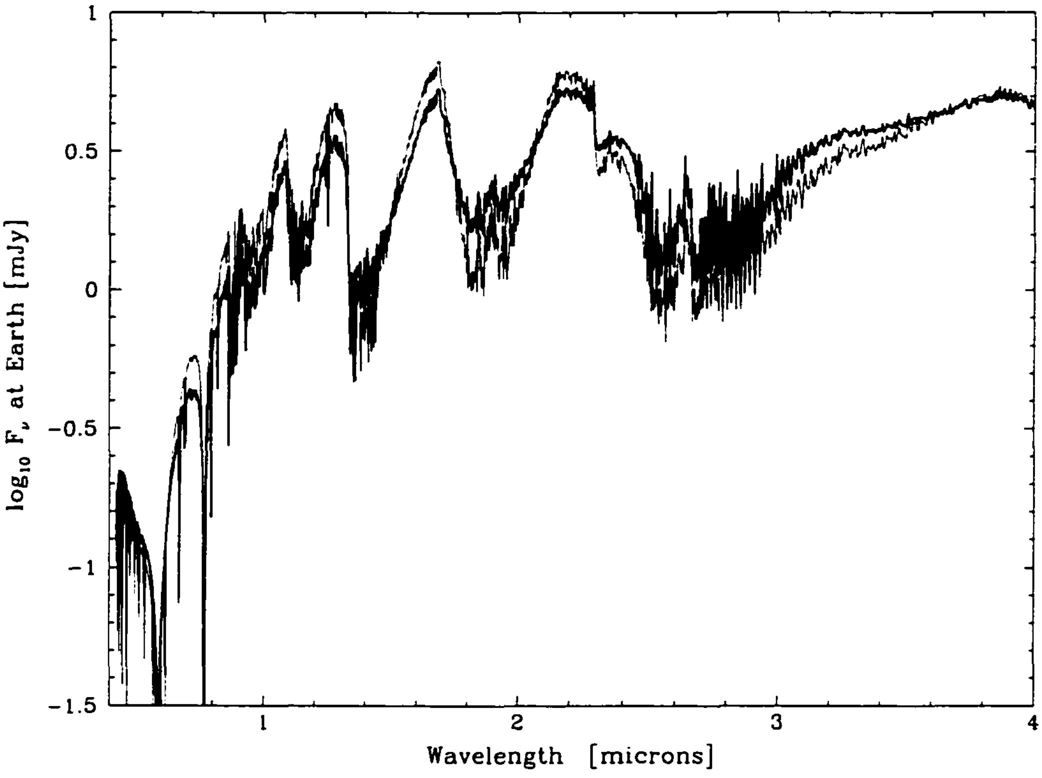

Figure 7.4 Fiducial model spectrum of υ And b (thick curve) versus that of a cloud-free model (thin curve). The removal of the clouds results in a wider variation from peak to troughout most of the spectrum.

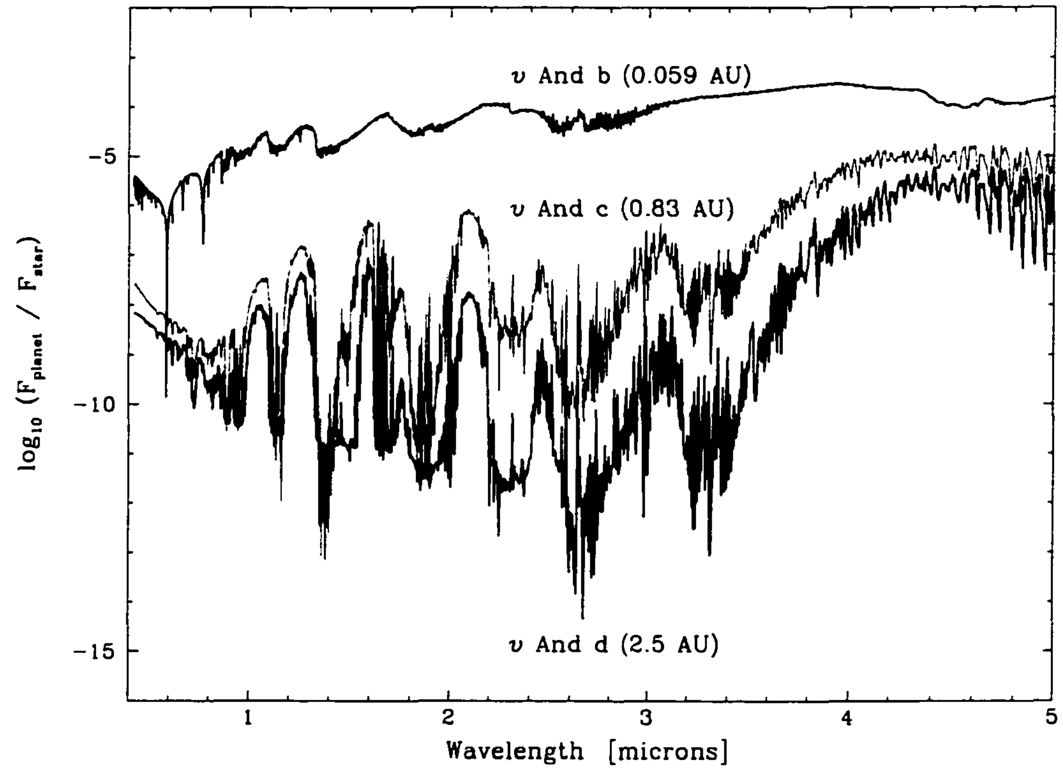

Figure 7.5 Wavelength-dependent, phase-averaged planet-to-star flux ratios for υ And b, c, and d.

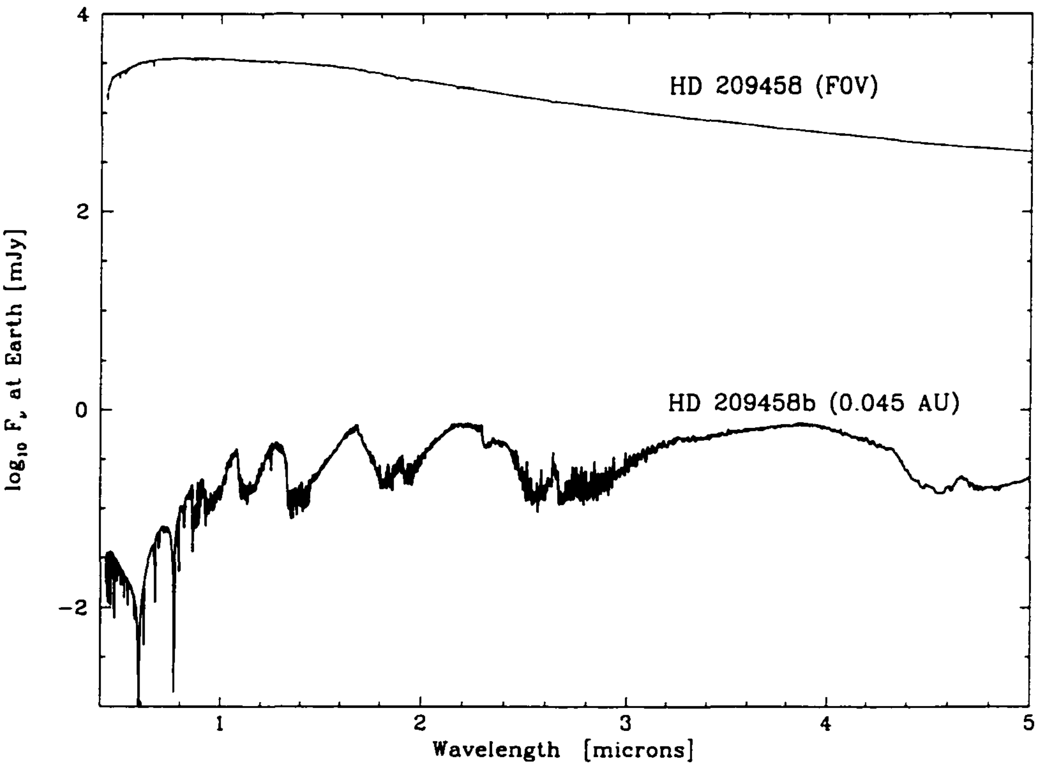

Figure 7.6 Visible and near-infrared spectrum of HD209458b along with an estimated spectrum of its primary (a scaled Kurucz model). These fluxes were calculated using the planetary radius of 1.35 R_J.

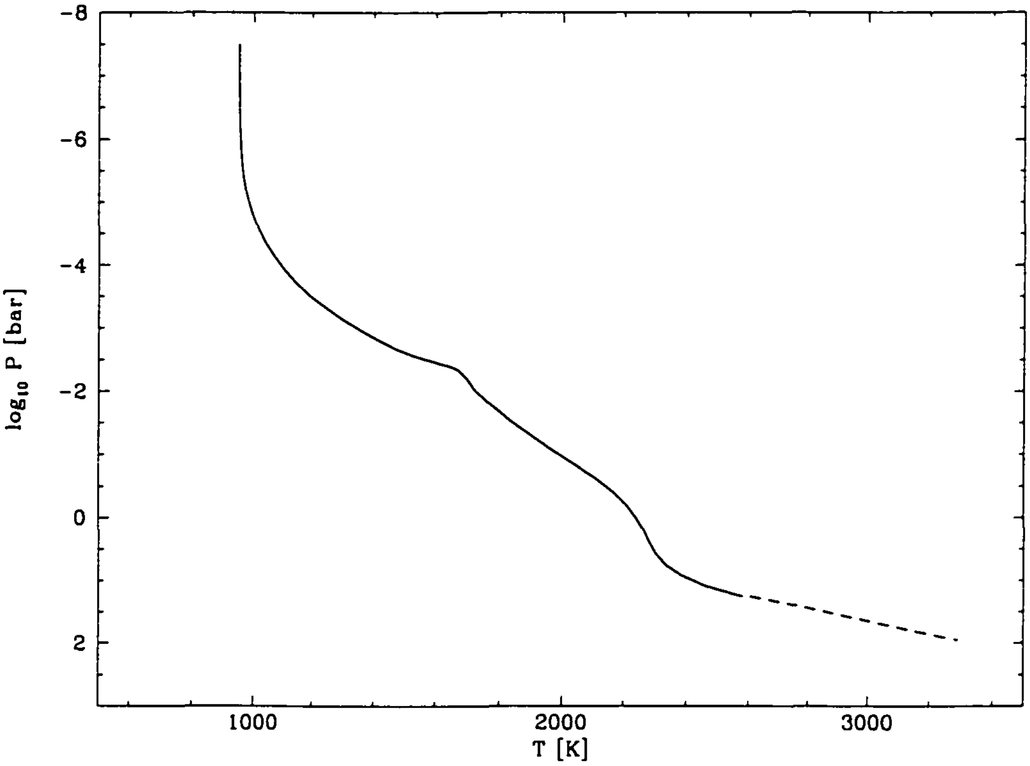

Figure 7.7 T-P profile of HD 209458b. The dashed portion of the profile indicates the convective region.

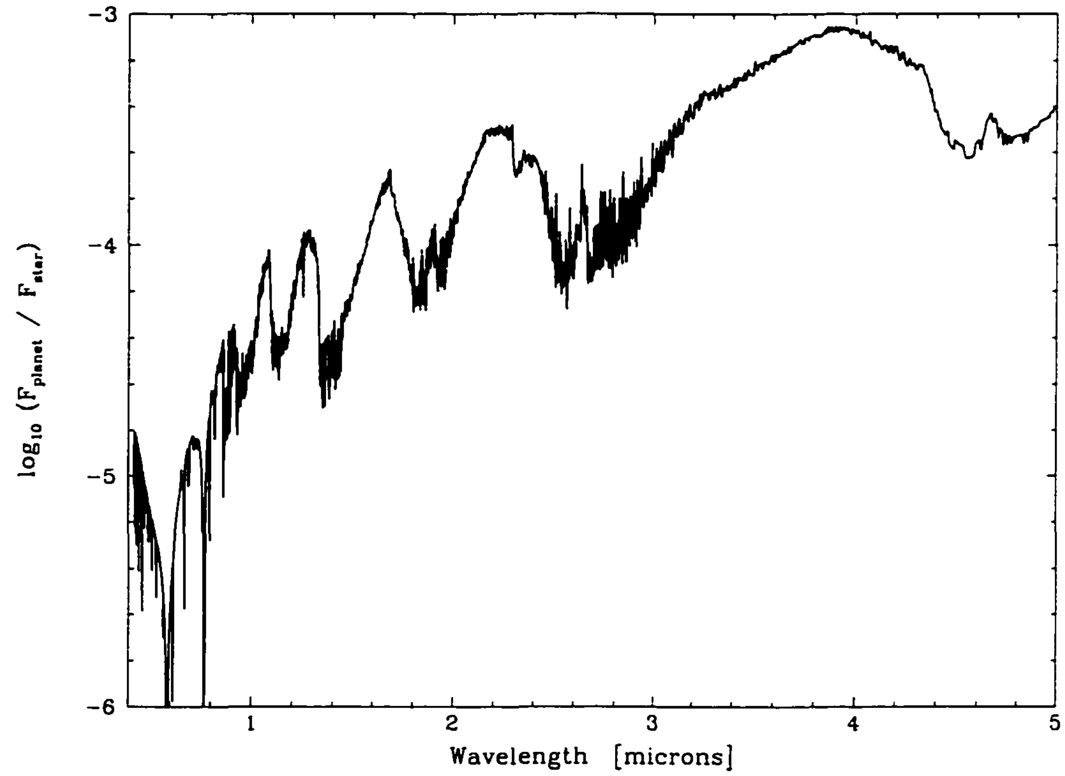

Figure 7.8 Wavelength-dependent, phase-averaged planet-to-star flux ratio of HD209458b. This ratio was calculated using the planetary radius of 1.35 R_J.

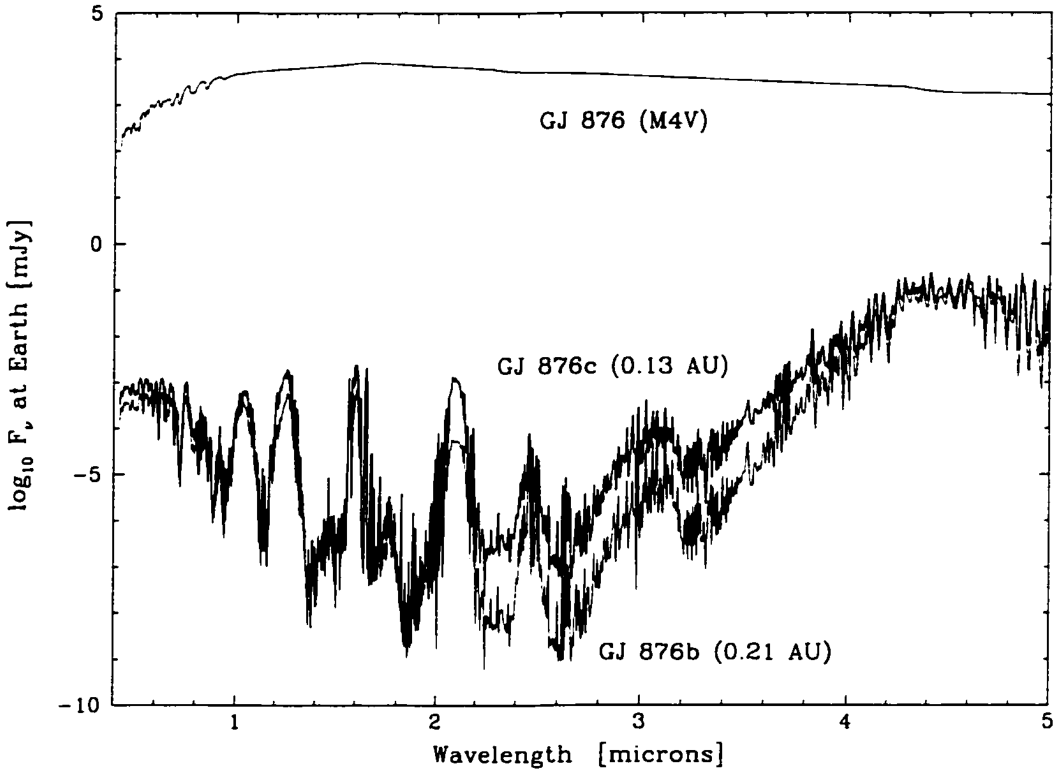

Figure 7.9 Visible and near-infrared spectra of GJ 876b and c. An estimated spectrum of the primary (a scaled Kurucz model) is also depicted. Both GJ 876b and c are Class III EGPs.

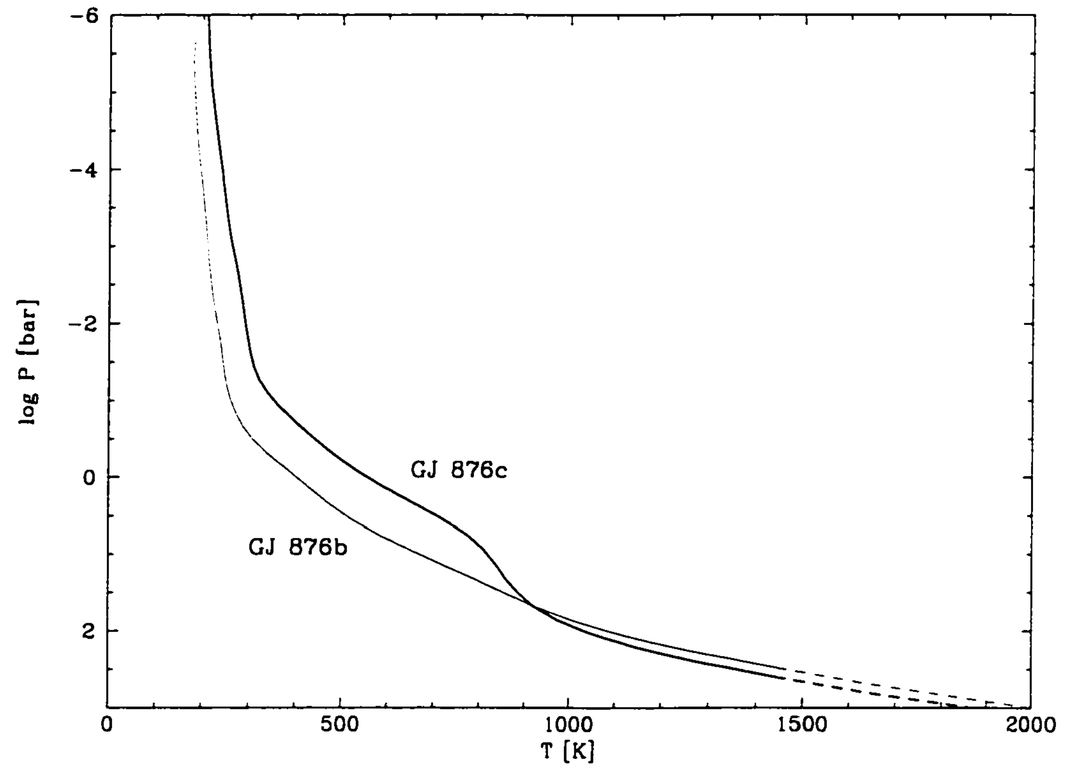

Figure 7.10 T-P profiles of GJ 876 b and c. The dashed portions of the profiles indicate convective regions.

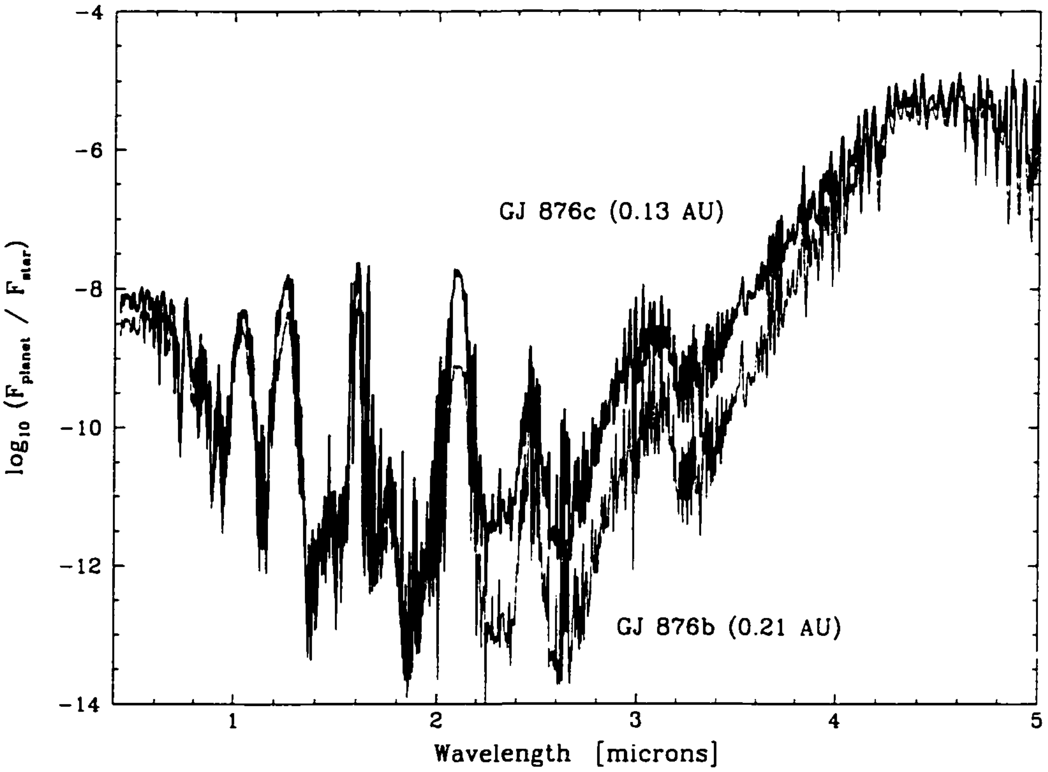

Figure 7.11 Wavelength-dependent, phase-averaged planet-to-star flux ratios for GJ 876 b and c.

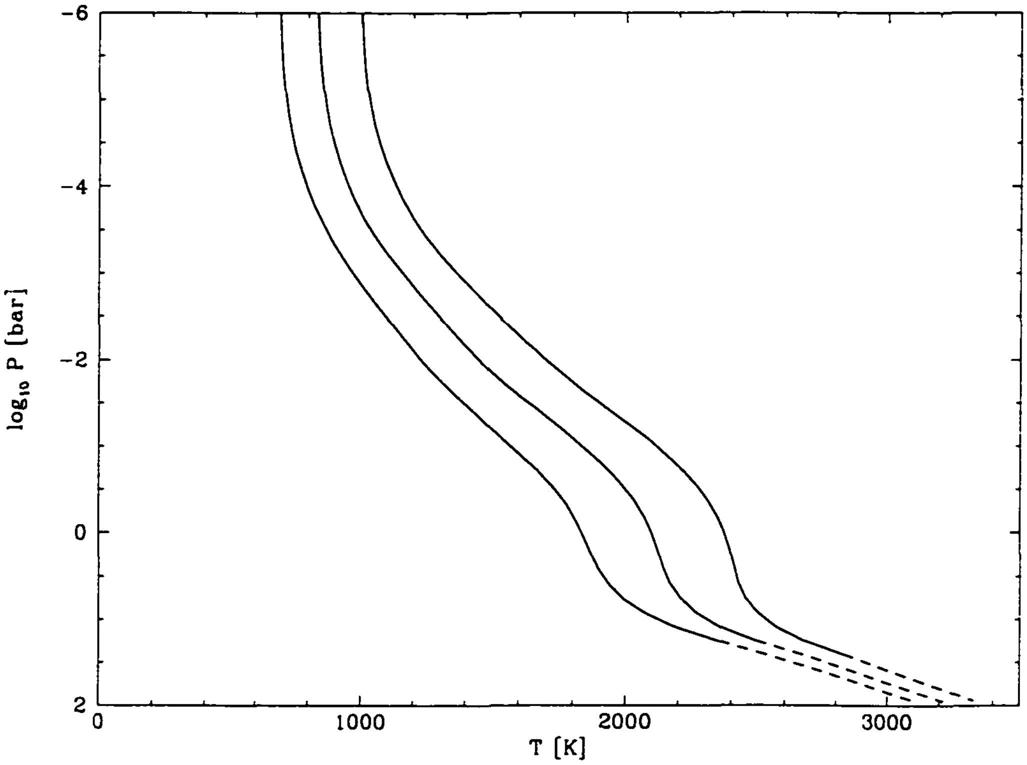

Figure 7.12 Cloud-free 51 Peg b T-P profiles with incident flux weighting of 1/4, 1/2, and 1. The coolest model shown has the flux weighting of 1/4. See text for details.

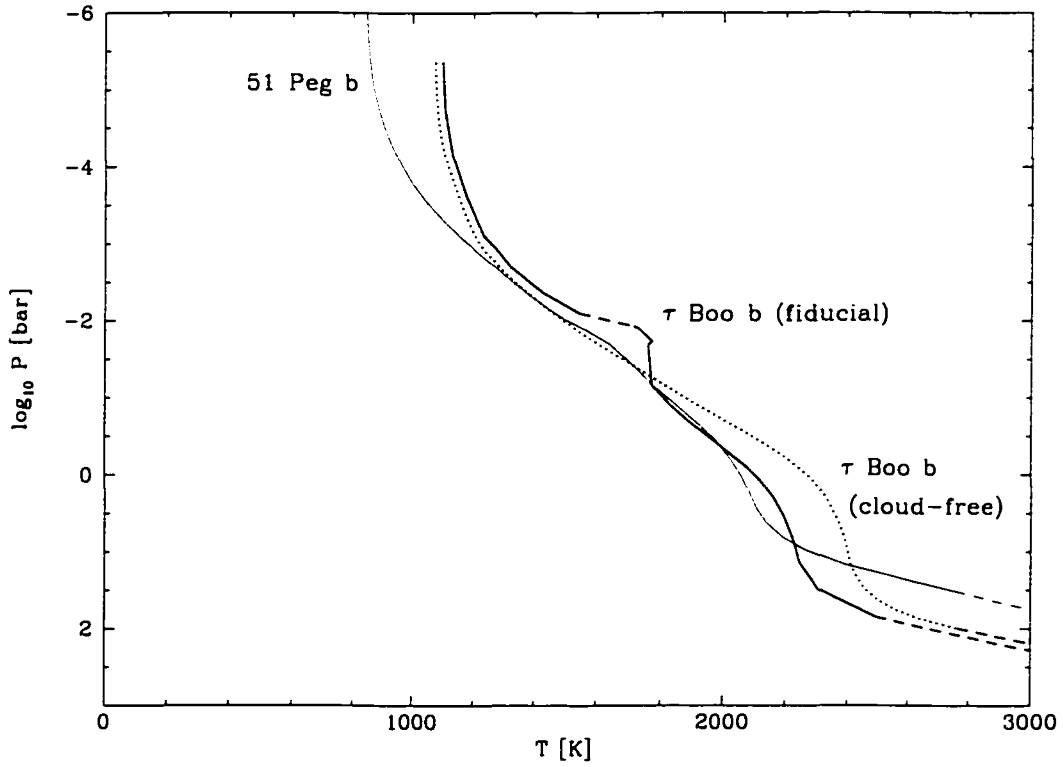

Figure 7.13 T-P profiles of τ Boo b and 51 Peg b. The dashed portions of the profiles indicate convective regions, and the fiducial model of τ Boo b is convective at low pressures, toward the top of the silicate cloud layer. Note that in order to achieve numerical convergence, the silicate and iron cloud layers of 51 Peg b have been attenuated to 10% of the elemental abundances of magnesium and iron, respectively.

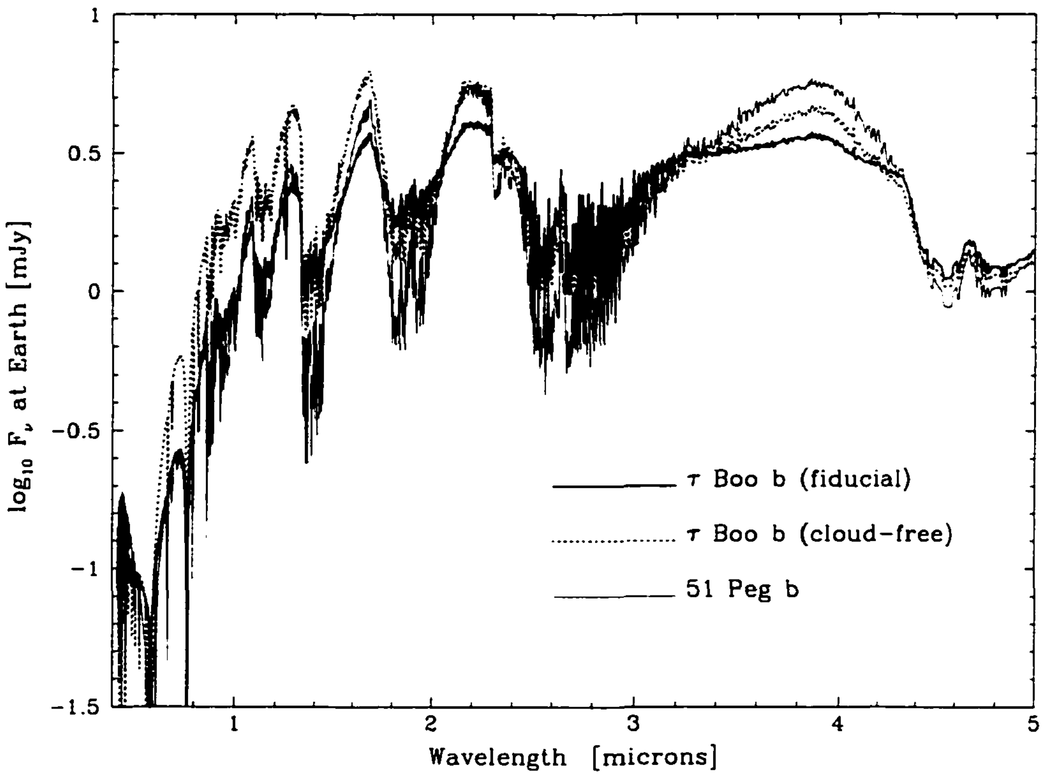

Figure 7.14 Visible and near-infrared spectra of τ Boo b and 51 Peg b. (Note that in order to achieve numerical convergence, the silicate and iron cloud layers of 51 Peg b have been attenuated to 10% of the elemental abundances of magnesium and iron, respectively, which may yield higher than actual fluxes in some spectral regions.)

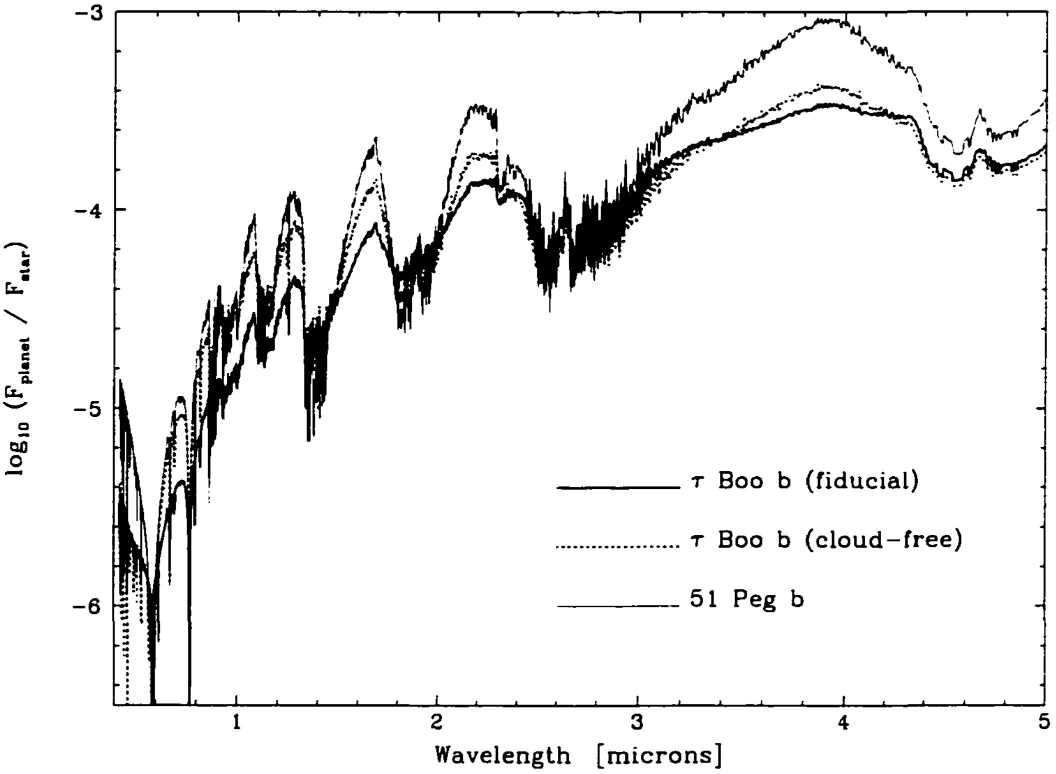

Figure 7.15 Wavelength-dependent planet-to-star flux ratios for τ Boo b and 51 Peg b. (Note that in order to achieve numerical convergence, the silicate and iron cloud layers of 51 Peg b have been attenuated to 10% of the elemental abundances of magnesium and iron, respectively, which may yield higher than actual fluxes in some spectral regions.)

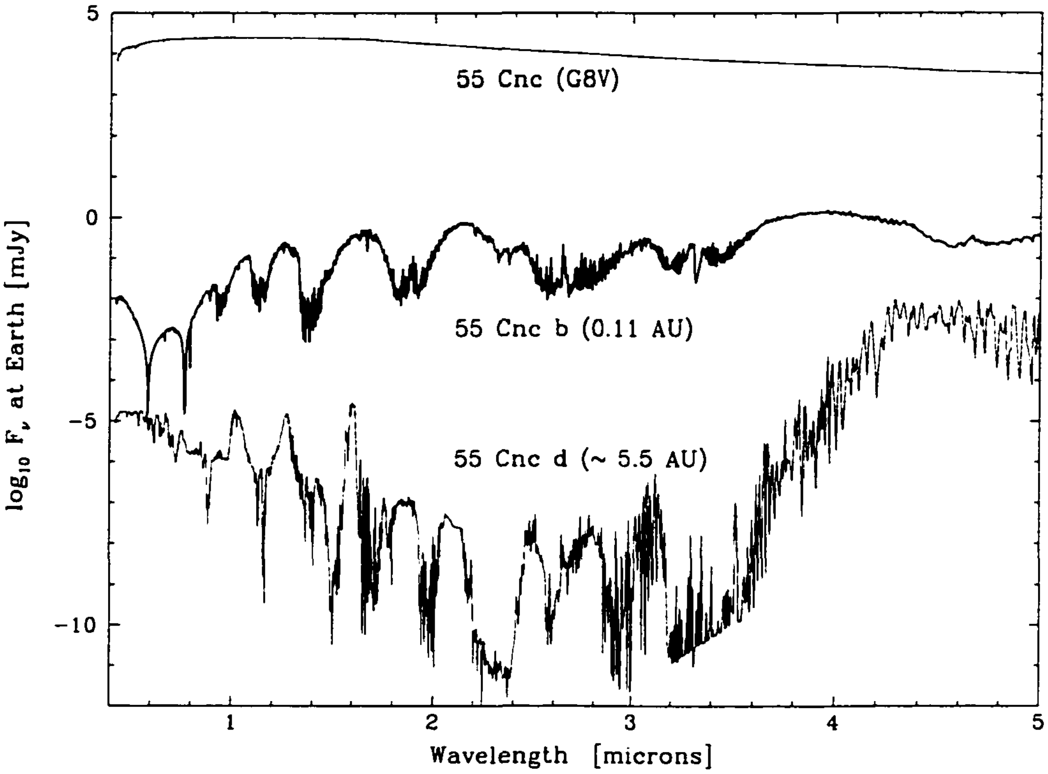

Figure 7.16 Visible and near-infrared spectra of 55 Cancri b and d. An estimated spectrum of the primary (a scaled Kurucz model) is also depicted. 55 Cnc b and d are Class IV and II EGPs, respectively.

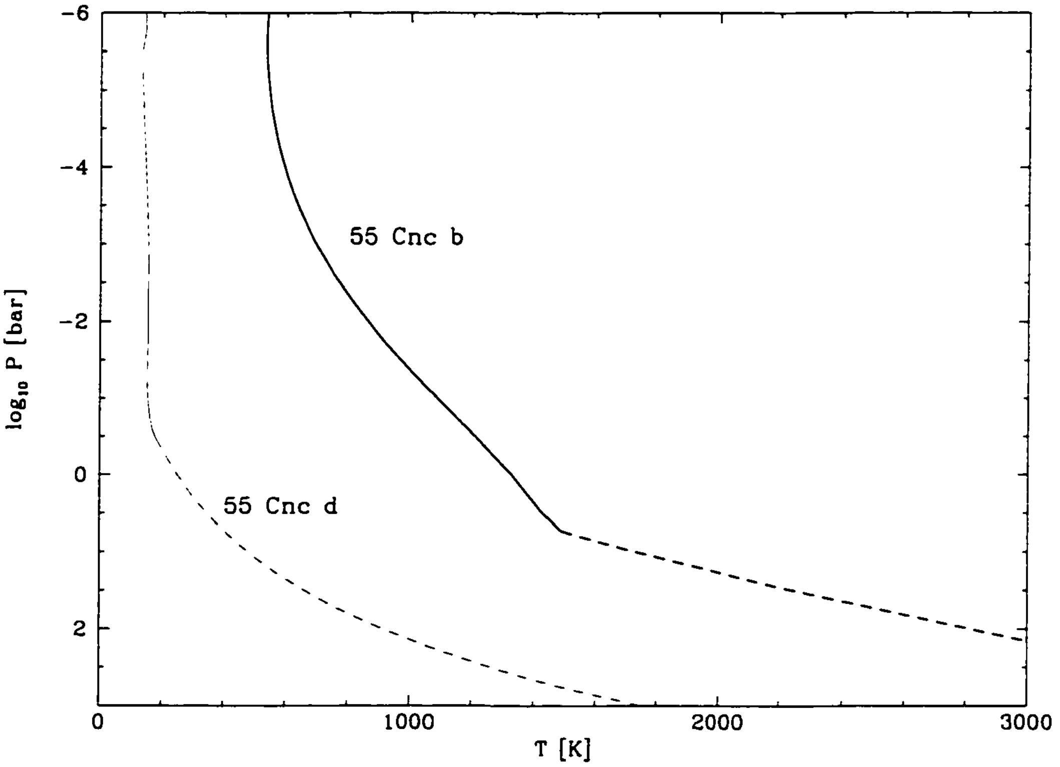

Figure 7.17 T-P profiles of 55 Cancri And b and d. The dashed portions of the profiles indicate convective regions.

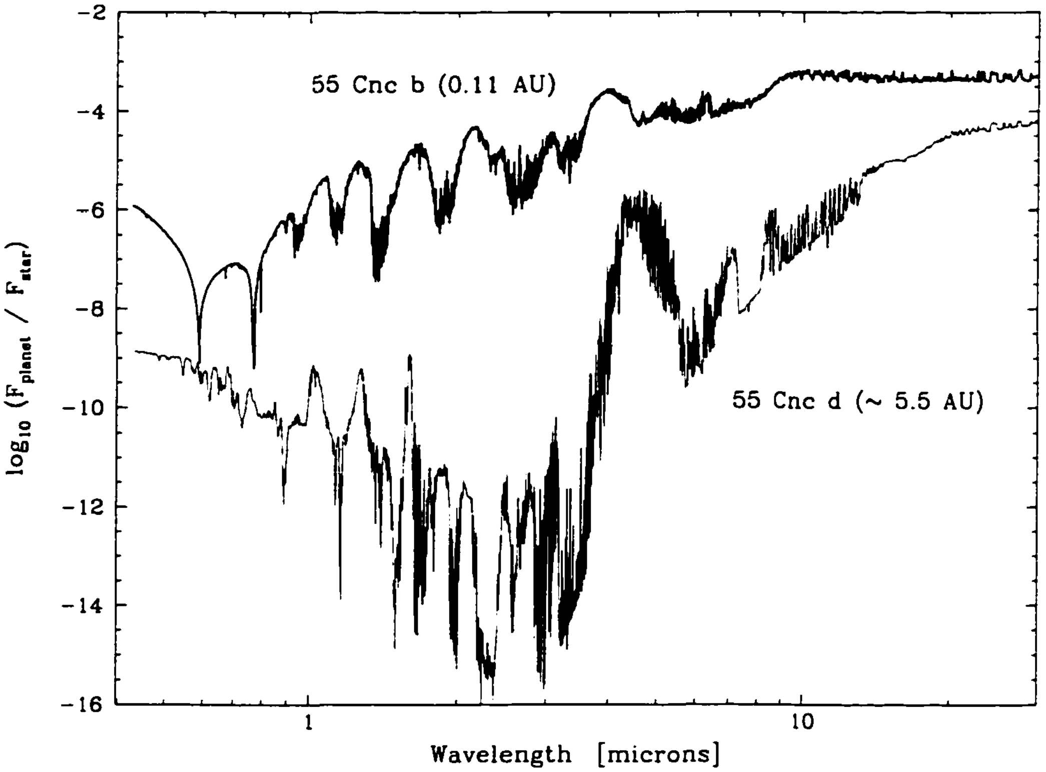

Figure 7.18 Wavelength-dependent, phase-averaged planet-to-star flux ratios for 55 Cnc b and d from 0.4 to 30 μm.

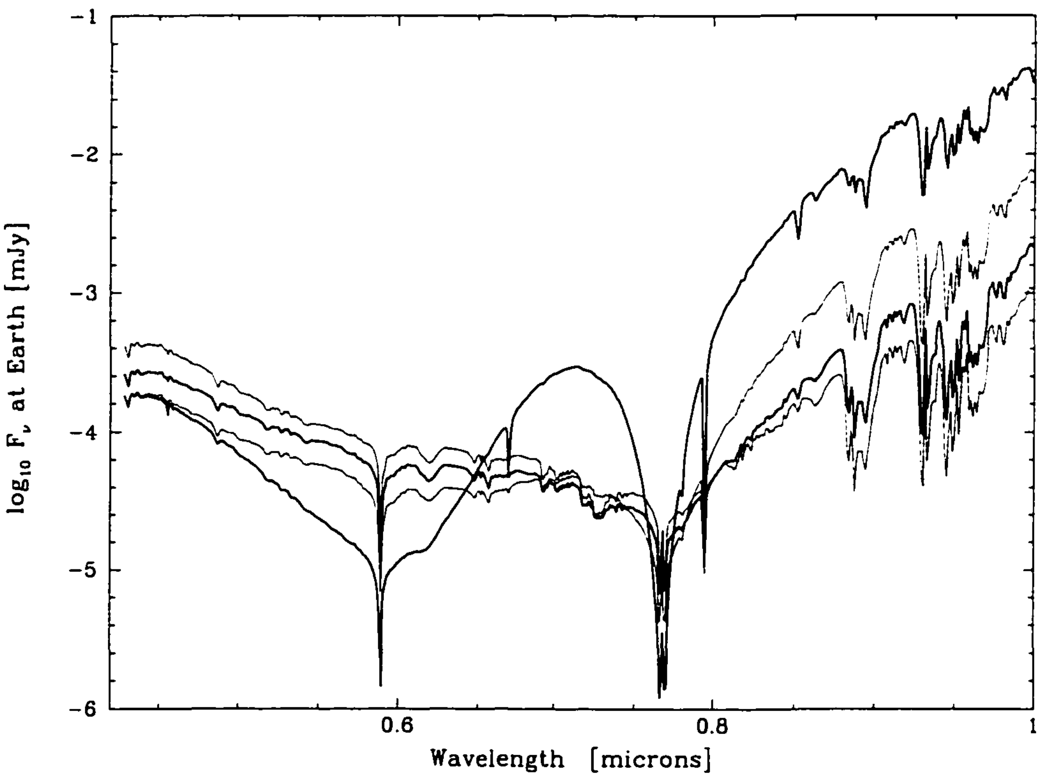

Figure 7.19 Visible model spectra of HD 114762b for various surface gravities and inner boundary fluxes. Four different models of HD 114762b are shown. From top to bottom near the sodium resonance line (or bottom to top near 1 μm) the inner boundary fluxes (in terms of T_{eff}) and surface gravities of the models are 300 K, 3×10^4 cm s^{-2}; 500 K, 10^5 cm s^{-2}; 700 K, 2×10^5 cm s^{-2}; and 1000 K, 3×10^5 cm s^{-2}.

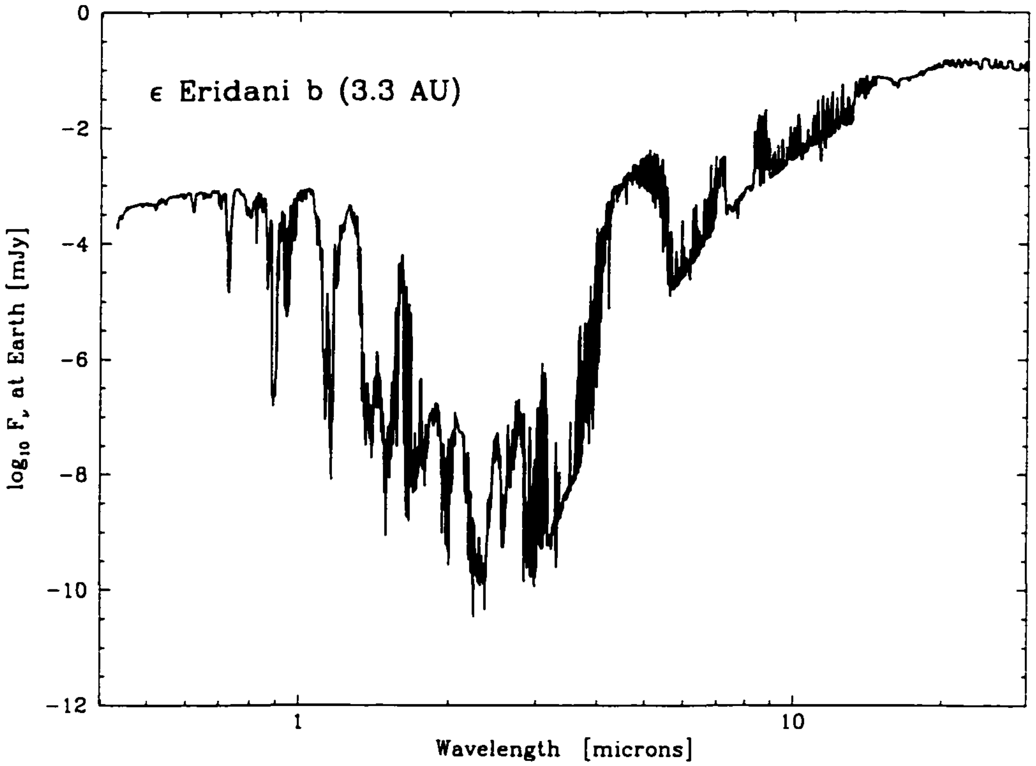

Figure 7.20 Model spectrum of ϵ Eri b from 0.4 to 30 μm. ϵ Eri b is a Class II EGP with a water cloud layer near a pressure of 1 bar. For this fiducial model, a cloud particle size distribution peaked at 5 μm is used, and 10% of the available H_2O is assumed to condense.

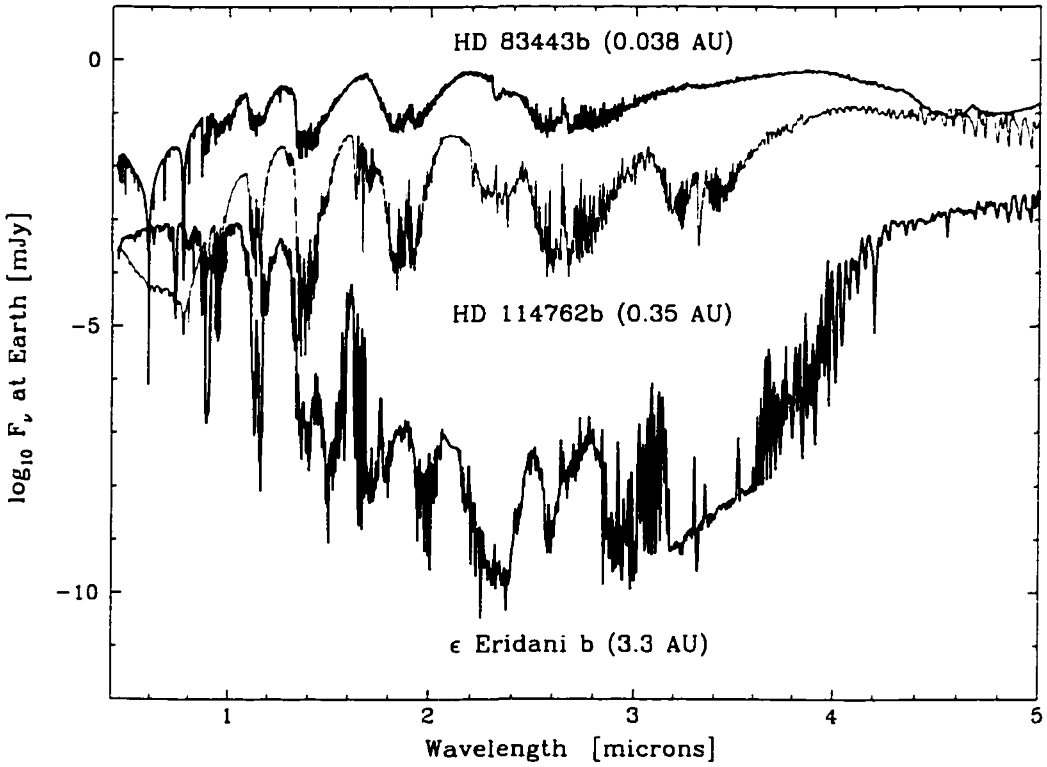

Figure 7.21 Visible and near-infrared spectra of HD 83443b, HD 114762b, and ϵ Eri b. These planets are Class V, III, and II EGPs, respectively.

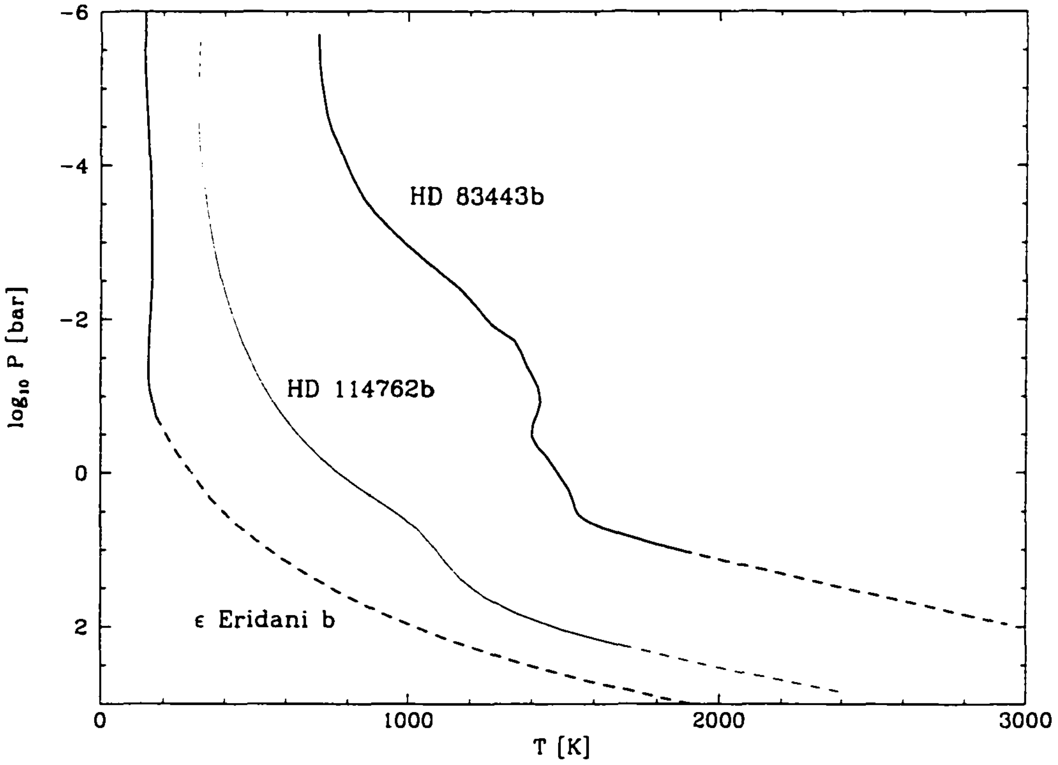

Figure 7.22 T-P profiles of HD 83443b, HD 114762b, and ϵ Eri b. The dashed portions of the profiles indicate convective regions.

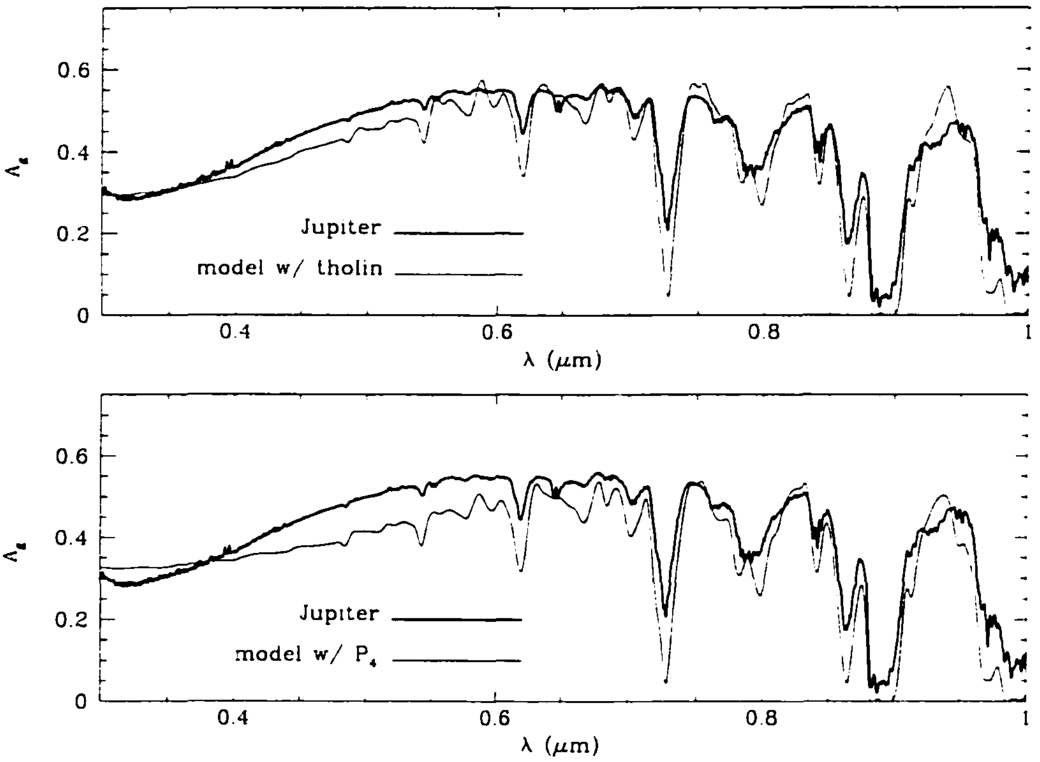

Figure 7.23 Geometric albedo spectrum of Jupiter. Model albedo spectra (thin curves) are compared with the observational full-disk albedo spectrum (thick curve; Karkoschka 1994). The top model uses tholin as a chromophore, while the bottom model uses P_4.

8 PARAMETER STUDIES

In any modeling endeavor, a lack of observational or experimental data leads to poor constraints on the applicability of self-consistent, but unverified, theoretical work. While the present work is grounded in both brown dwarf observations and in observations of the giant planets of our own Solar System, the variation of parameters such as cloud particle sizes, inner boundary fluxes, surface gravity, photoionization level, etc. can, in some cases, have substantial effects on atmospheric structure and emergent spectra. Here, I'll explore such effects in a systematic manner.

8.1. A Generic Model Sequence from 5AU to 0.05 AU

I begin with an instructive, but generic, sequence of cloud-free EGP models about a G0V primary. For simplicity and ease of convergence, the inner boundary flux is set equivalent to that of an isolated object with $T_{eff} = 500$ K, and the resulting EGP models are compared with that of a brown dwarf of the same effective temperature and gravity (3×10^3 cm s^{-2}).

Figure 8.1 illustrates the effects of irradiation on the temperature-pressure structure of an EGP at various distances, from 5 AU to 0.05 AU from a G0V primary. At large distances, the intrinsic luminosity of the planet dominates, but large changes to the T-P profile occur within $\sim$ 1 AU. In particular, the outer atmosphere heats up. As the EGP is moved very close to the star ($\sim$ 0.1 AU), the temperature in even the convective region increases substantially.

Figure 8.2 shows the emergent spectra of these models, including that of the isolated object. From high to low temperature, one can see certain atomic and molecular features appear and disappear. For the objects orbiting most closely to the primary, the alkali absorption lines in the visible are strong, as are the CO features at 2.3 μm and $\sim$ 4.4-5 μm. But as the EGP is moved away from the primary, the alkali lines weaken, giving way to Rayleigh scattering by the gaseous species high in the atmosphere, where the alkali abundances are negligible. The CO features quickly weaken as well, while methane absorption becomes quite strong, particularly at 3.3 μm. Water absorption remains strong for the full model set, which is not surprising considering its high abundance throughout a very broad range in temperature and pressure.

It is clear from Figure 8.2 that for wavelengths greater than $\sim$ 0.8 μ, the emergent spectrum of an EGP approaches that of an isolated object with the same inner boundary flux for larger and larger orbital distances. However, this is not clear in the visible region of the spectrum. Here, reflection of the incident stellar radiation keeps the emergent flux from matching the very low flux of the isolated object. Figure 8.3 indicates that this is true, albeit to a lesser degree, even at an orbital distance greater than 30 AU! While the flux in the potassium doublet ($\sim$ 0.77 μm) is perfectly matched, that in the Na–D doublet is not. If we were to "turn off" Rayleigh scattering in the EGP, this would not be the case. Figure 8.4 contains the emergent spectra of a couple of models without Rayleigh scattering. At $\sim$ 2 AU, the resulting EGP spectrum closely approaches that of the isolated object in the visible. In reality, of course, Rayleigh scattering is present. The upshot is that the emergent spectrum of a planet that is massive or young enough to have a fairly high intrinsic luminosity will have a much different visible spectrum than an isolated brown dwarf of similar temperature, even though a wide planetary orbit yields a very similar T-P profile.

The planet-to-star flux contrast as a function of wavelength is of central importance in any campaign to detect EGPs directly. I plot these planetary phase-averaged, planet-to-star flux ratios for the models of Figure 8.2. It is important to stress that these are generic, cloud-free models, which assume a central star of type G0V, but a sense of the dependence on orbital distance for a very massive and/or young EGP is well illustrated. For a very close-in object, the flux ratio varies from $\lesssim 10^{-5}$ in the visible to $\lesssim 10^{-3}$ in the 3.8-4.0 μm region. In almost all cases, this ratio becomes smaller at all wavelengths with increasing orbital distance (as expected from the a^{-2} diminution of stellar flux at the planet). The exception appears to be in the 4.4-4.8 μm range for orbital distances between $\sim$ 0.1-0.2 AU, because the CO absorption strength there quickly wanes with decreasing atmospheric temperature. The infrared contrast becomes dependent on only wavelength (not distance) once the orbital distance of the planet is great enough that its internal luminosity dominates the emergent spectrum.

8.2. Effects of Inner Boundary Flux Variation

Section 8.1 was a study of the effect of varying the outer boundary flux, while holding the inner boundary flux constant. In this section, I'll explore just the opposite, holding the outer boundary flux constant while varying the inner boundary flux.

Without evolutionary models, it is not possible to know the correct inner boundary flux when modeling the atmospheres of EGPs. This inner boundary flux fixes the *net* flux at the surface (not to be confused with the emergent flux, the outward flux at the surface), so long as there are no sources or sinks throughout the atmosphere. That is, integrated over all frequencies, the net flux at every depth zone is constant. For an isolated object with no incident radiation, the emergent flux is equivalent to this net flux. (This, of course, is not true for irradiated objects such as EGPs.)

When modeling atmospheres of EGPs without evolutionary models, one must make reasonable assumptions about the inner boundary. One may choose an inner boundary flux based on the evolutionary models of isolated objects (Burrows et al. 1997). Such a choice would provide the correct intrinsic luminosity of the EGP in isolation, assuming its mass and age are known. While this may provide a good approximation in some cases, such an approach ignores the fact that the interior and atmosphere are inexorably coupled, and so an incident flux will affect the interior and the evolution of the object as a whole Burrows et al. 2000b. For heavily irradiated objects, strong horizontal winds are expected, and it has been suggested recently that even a small vertical component can transport kinetic energy to the interior, acting as an additional heat source (Guillot & Showman 2002).

Since deciding upon the inner boundary condition for an atmosphere model is obviously not a trivial task, it is important to explore the variation in the emergent spectrum and T-P structure as a function of the inner boundary flux. Using a Class IV EGP model (a cloud-free version of 55 Cancri b), I investigate the effects of varying this flux by up to 5 orders of magnitude. Figure 8.5 shows the EGP T-P structures for inner boundary fluxes (= $\sigma T_{\rm eff}^4$) corresponding to $T_{\rm eff}$= 1000 K (top curve), 750 K, 500 K, 300 K, 150 K, and 50 K (bottom curve). The dashed portions of the curves indicate the convective regions. At pressures greater than ~ 1 bar, each of these profiles is substantially different. Clearly, the T-P structure in the deepest regions is determined by the chosen inner flux. However, at pressures of less than a bar, only the 1000 K and 750 K models deviate significantly from those with lower temperature inner boundary fluxes.

The emergent spectra associated with these models are depicted in Figure 8.6. The lowest curves (300 K, 150 K, and 50 K; overlapping at the bottom) are nearly identical, indicating that below 300 K, the inner boundary condition ceases to have any noticeable effect on the emergent spectrum of an object as hot as Class IV. The 500 K boundary model is also very close to these lower temperature models at most, but not all wavelengths, with the most significant deviations appearing in the flux peaks between ~ 0.8 and 1.4 μm. The 750 K and 1000 K models have higher fluxes than the other models at most wavelengths. Still, the ~ 5 dex increase in the inner boundary flux between the 50 K model and the 1000 K model translates to well under a 1 dex difference in the emergent spectrum at most wavelengths.

8.3. Effects of Surface Gravity Variation

Since only the minimum masses of most EGPs are known, and their radii are given only by theoretical models, the surface gravities of EGPs are problematic. In this section, I explore the dependence of the T-P structure and emergent spectrum on surface gravity, which is an input to the atmosphere models.

An estimate of the minimum surface gravity for most objects can be made by assuming a radius close to that of Jupiter, or more accurately, obtaining the radius from evolutionary models of isolated objects. Statistically speaking, upper limits can be estimated crudely by noting that the actual mass of an EGP should rarely be more than a factor of 3 or 4 greater than its Msin$i$. Otherwise a clearly disproportionate number of detected EGPs would be nearly face-on. But no degree of certainty for a given object can be claimed without accurate astrometry or the fortuity of an EGP that transits its primary. The only certain case presently known is HD 209458b. As a low-mass roaster, HD 209458b has a particularly low surface gravity; its larger than predicted radius is probably the result of a good part of its evolutionary history taking place under intense stellar irradiation (Burrows et al. 2000b). For the majority of EGPs, regardless of their proximity to their central star, the surface gravities are rather poorly constrained. Hence, a parameter study on gravity is important.

Using a Class III EGP model, I vary the surface gravity from 10^3 to 3×10^5 cm s^{-2} in steps of 1/2 dex. Figure 8.7 depicts the resulting T-P profiles. (The top curve is the lowest gravity model.) Increasing the gravity by 1/2 dex increases the pressure at a given atmospheric temperature by roughly 1/2 dex as well, as one could estimate from hydrostatic equilibrium. Of course, since compositions and opacities vary with pressure and temperature, this problem is not merely one of hydrostatic equilibrium, but such simple arguments hold reasonably well. Since the surface gravity varies roughly in concert with the mass (the radius does not vary too strongly with mass), a 1/2 dex uncertainty in the mass of an EGP might correspond to the differences between two adjacent T-P profiles in Figure 8.7.

The associated emergent spectra for these models are shown in Figure 8.8. For these Class III models, an increase in gravity results in a general decrease in flux shortward of ~ 2.2 μm, and an increase longward. Additionally, a larger gravity tends to reduce the peak-to-trough variations throughout the spectrum. While there certainly are some large differences between the 10^3 and 3×10^5 cm s^{-2} (a massive brown dwarf) models, a 1/2-dex difference in surface gravity produces a relatively small difference in the emergent spectrum.

8.4. Effects of Condensate Particle Size Variation

The scattering and absorption of radiation by condensates is a wavelength-dependent function of particle size. Ice and grain clouds with various particle size distributions are treated with Mie theory (see Chapter 5). Here, I vary the median particle size for a water cloud size distribution to investigate the effects on the emergent spectrum of the Class II EGP, ϵ Eridani b.

As presented in §7.6, my fiducial median particle size for ϵ Eridani is 5 μm. For two other models, I use median sizes of 0.5 μm and 50 μ. The effects on the visible and near-infrared emergent spectrum are shown in Figure 8.9 along with a cloud-free spectrum of the planet (bottom curve). The 0.5 μm model (top curve) produces the most reflection, followed by the 5 μm model, and then the 50 μm model. The cloud-free model visible and near-infrared fluxes are substantially lower because Rayleigh scattering alone provides limited reflection with increasing wavelength. In the visible spectral region, the three cloudy models differ by less than a factor of 2 at any given wavelength. However, in the infrared J and H bands the variation is significantly larger, with the 0.5 μm and 50 μm models differing by roughly an order of magnitude. The effects out to 30 μm are depicted in Figure 8.10. The cloudy models simply to not differ much beyond the near-infrared. However, each of the cloudy models does differ from the cloud-free model in the 4-5 μm opacity window region by up to two orders of magnitude. The clouds act to close-off the window, blocking radiation from the deeper atmosphere, which can escape through this window in the cloud-free case.

In general. different condensate particle sizes will translate to significant differences in some wavelength regions of an EGP's emergent spectrum. However. such differences are unlikely to rival the differences between cloud-free and cloudy EGP models.

8.5. Photoionization Depths of the Alkali Metals

As discussed in detail in §3.5, photoionization of the alkali metals in the outermost atmosphere of a close-in EGP is likely due to strong incident ultraviolet radiation from the primary. Here, I'll quantify the effects on the emergent spectrum of a Class V EGP. The simplest approach to simulating the spectral effects of ionization is just to eliminate or reduce the neutral alkali metal abundances at all pressures lower than some given pressure depth. Of course, this is a rather crude means of dealing with a very complex problem, but it allows us to get a quick handle on the effects.

Figure 8.11 is a plot of the visible spectral region for three model spectra: no ionization, ionization to 1 mbar, and ionization to 100 mbar. For the sake of numerical convergence of the two ionization models, a gradual decline in the alkali abundances with decreasing pressure was implemented. The alkali abundances were weighted by P/P_0 (for $P < P_0$ only), where $P_0 = 1$ mbar or 100 mbar for the ionization models. The 1-mbar ionzation model is hardly distinguishable from the no-ionization model, though for the 100-mbar model, the absorptions at the sodium and potassium resonance lines are reduced somewhat. Since 100 mbar is almost certainly the greatest conceivable photoionization depth expected for most systems (§3.5), I conclude that the reduction or elimination of the neutral alkali metals in the outermost atmosphere of an EGP will not have substantial effects on its *emergent* spectrum because the alkali lines are formed mainly at pressures greater than 0.1 bar. Nevertheless, the effect could be slightly larger than shown in Figure 8.11 because of the gradual decline in the alkali abundances implemented and due to the use of a planar atmosphere code, which does not account for effects toward the limb of the EGP, where a more oblique column depth does not probe to deep pressures. In this regard, the emergent spectrum should not be confused with the transit spectrum (or wavelength-dependent transit radius), for which the outer atmosphere is most relevant. For a transit spectrum, the ionization of the alkalis in the outer atmosphere should produce a large difference relative to the no-ionization case (Fortney et al. 2002).

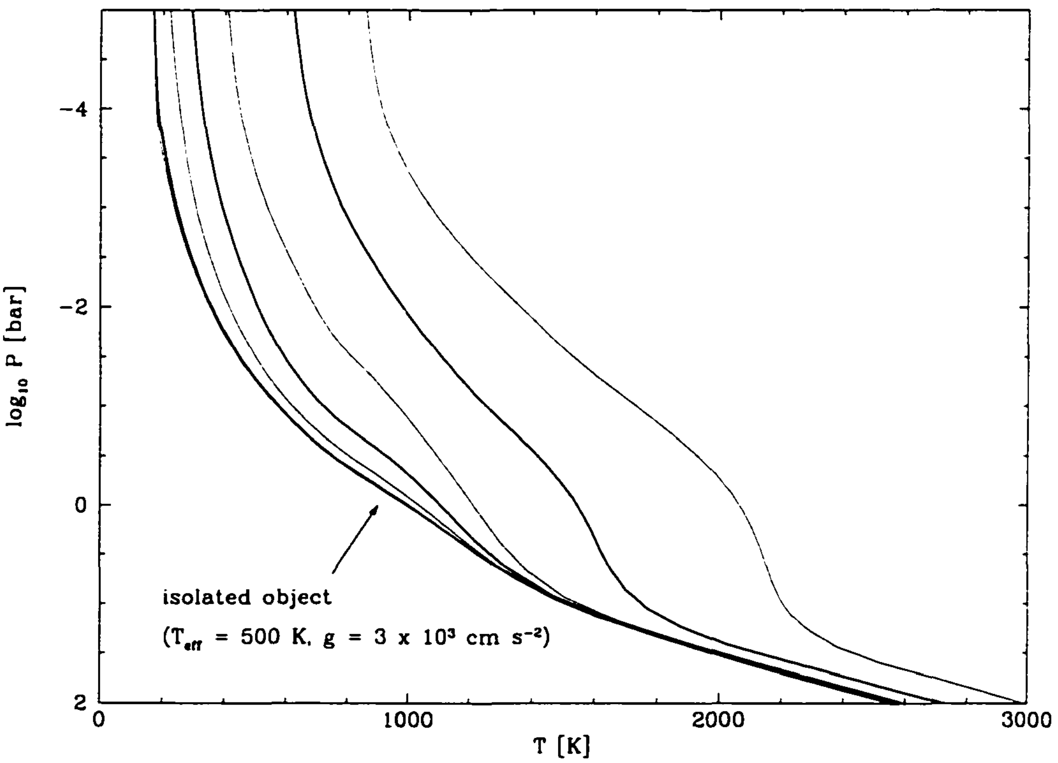

Figure 8.1 Cloud-free EGP T-P profiles as a function of orbital distance from a G0V primary. From right to left, the orbital distance is 0.05 AU, 0.1 AU, 0.25 AU, 0.5 AU, 1 AU, and 5 AU. Additionally, the leftmost profile (thin curve) is that of an isolated brown dwarf. In all cases, the gravity is 3×10^3 cm s^{-2} and the lower boundary flux is set equal to that of an isolated object with $T_{\text{eff}} = 500$ K. The T-P profile of such an object at 5 AU (leftmost thick curve) approaches that of the isolated brown dwarf.

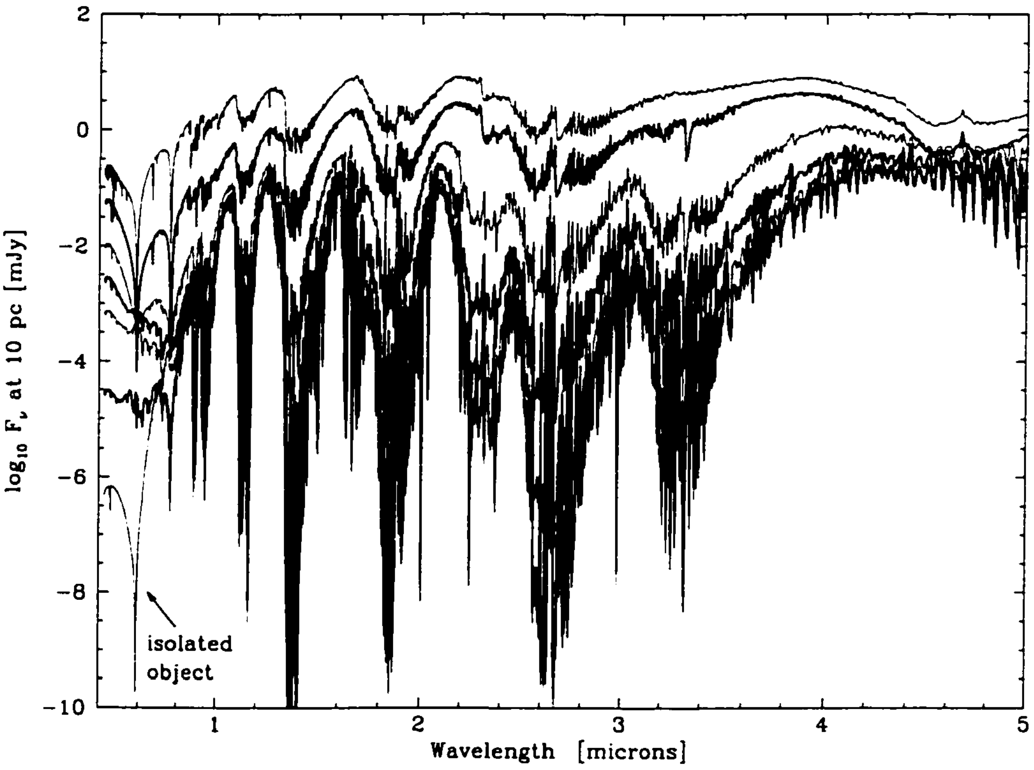

Figure 8.2 Cloud-free EGP emergent spectra as a function of orbital distance from a G0V primary. From top to bottom, the orbital distance is 0.05 AU, 0.1 AU, 0.25 AU, 0.5 AU, 1 AU, and 5 AU. Additionally, the bottom curve is that of an isolated brown dwarf. In all cases, the gravity is 3×10^3 cm s^{-2} and the lower boundary flux is set equal to that of an isolated object with $T_{\rm eff} = 500$ K. Rayleigh scattering of the incident stellar radiation keeps the EGP emergent flux in the visible significantly above that of the isolated brown dwarf.

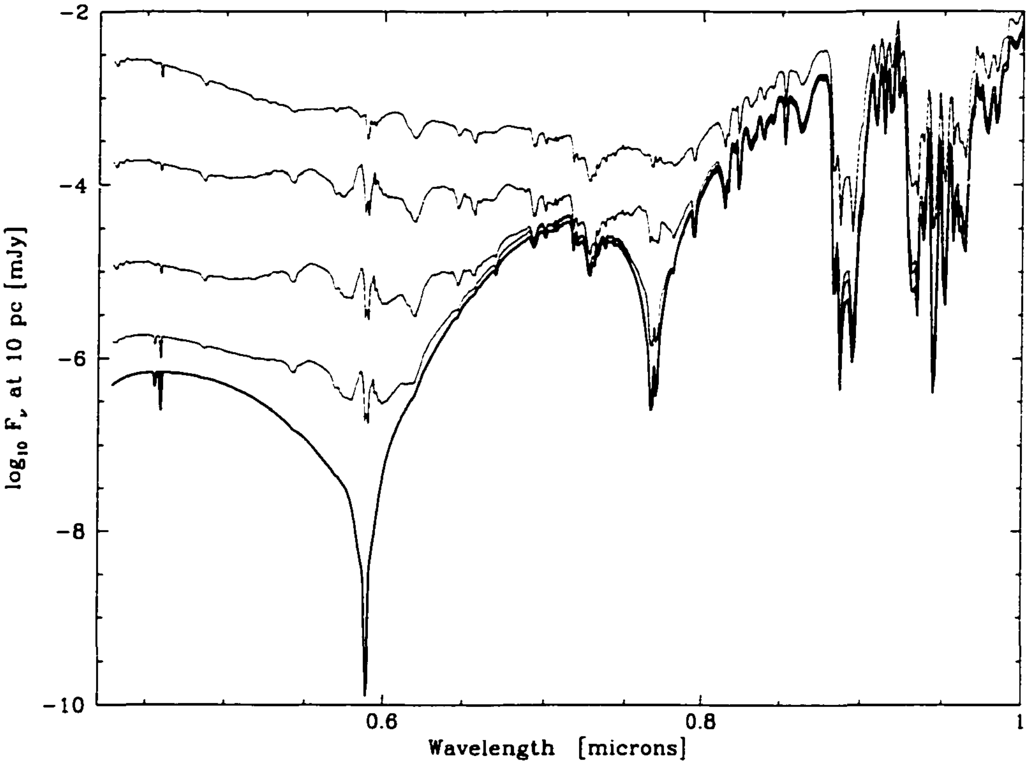

Figure 8.3 Comparison of the visible spectra of cloud-free EGPs orbiting a G0V primary with that of an isolated brown dwarf (thick curve). From top to bottom, the orbital distance is 0.5 AU, 2 AU, 8 AU, and 32 AU. In all cases, the gravity is 3×10^3 cm s^{-2} and the lower boundary flux is set equal to that of an isolated object with $T_{\rm eff} = 500$ K. Even at an orbital distance of 32 AU, the EGP spectrum in the vicinity of the sodium doublet is elevated above that of the isolated brown dwarf

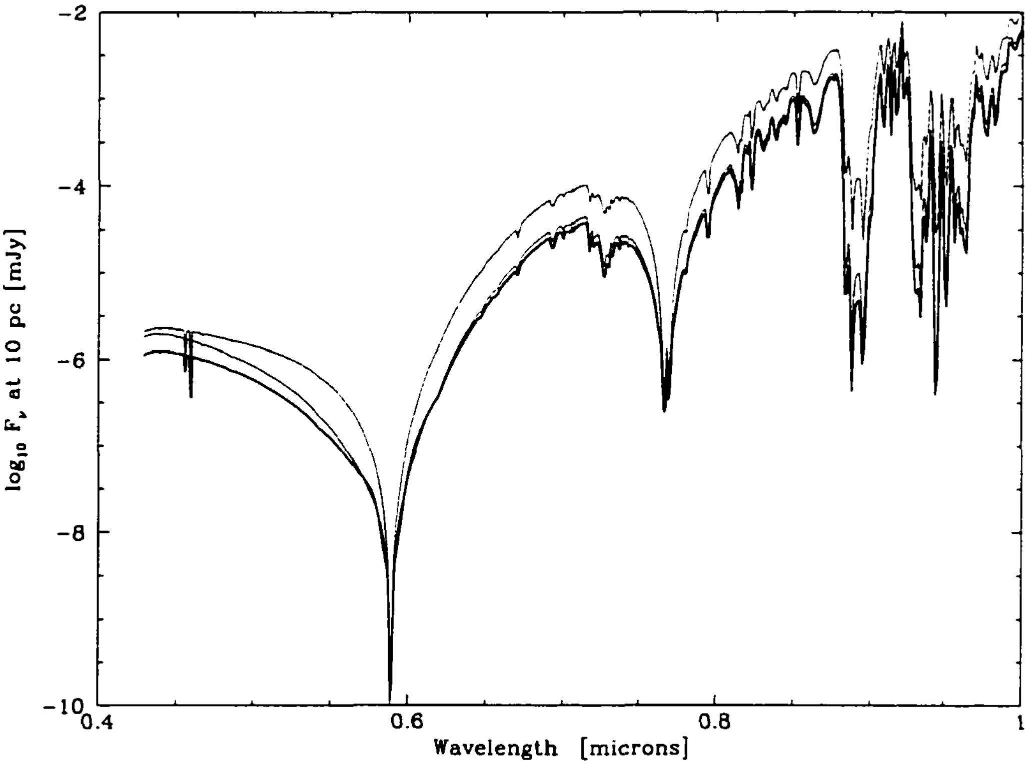

Figure 8.4 Same as Figure 8.3, but without any Rayleigh scattering. The EGP models shown are for orbital distances of 0.5 and 2 AU. Without rayleigh scattering, at 2 AU the emergent spectrum of the EGP approaches that of the isolated object (thick curve).

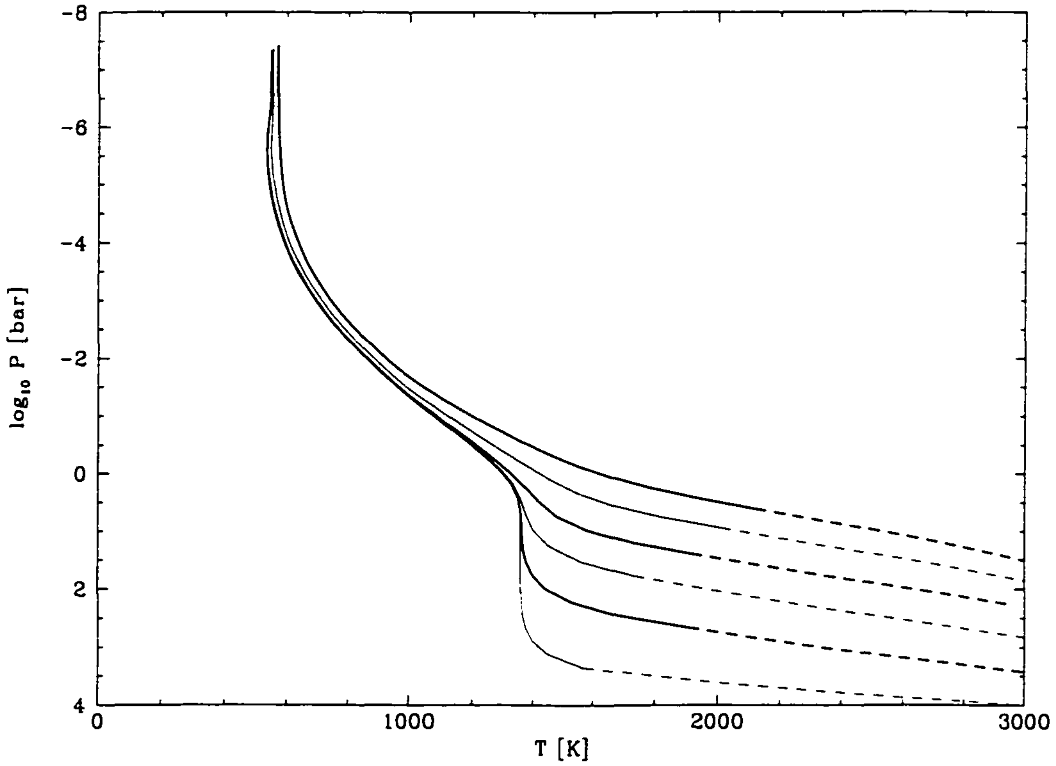

Figure 8.5 EGP T-P structure as a function of inner boundary flux. The inner boundary flux of a cloud-free Class IV model is varied. From the top profile to the bottom profile, models with inner boundary fluxes ($= \sigma T_{\rm eff}^4$) corresponding to $T_{\rm eff}$= 1000 K, 750 K, 500 K, 300 K, 150 K, and 50 K are shown.

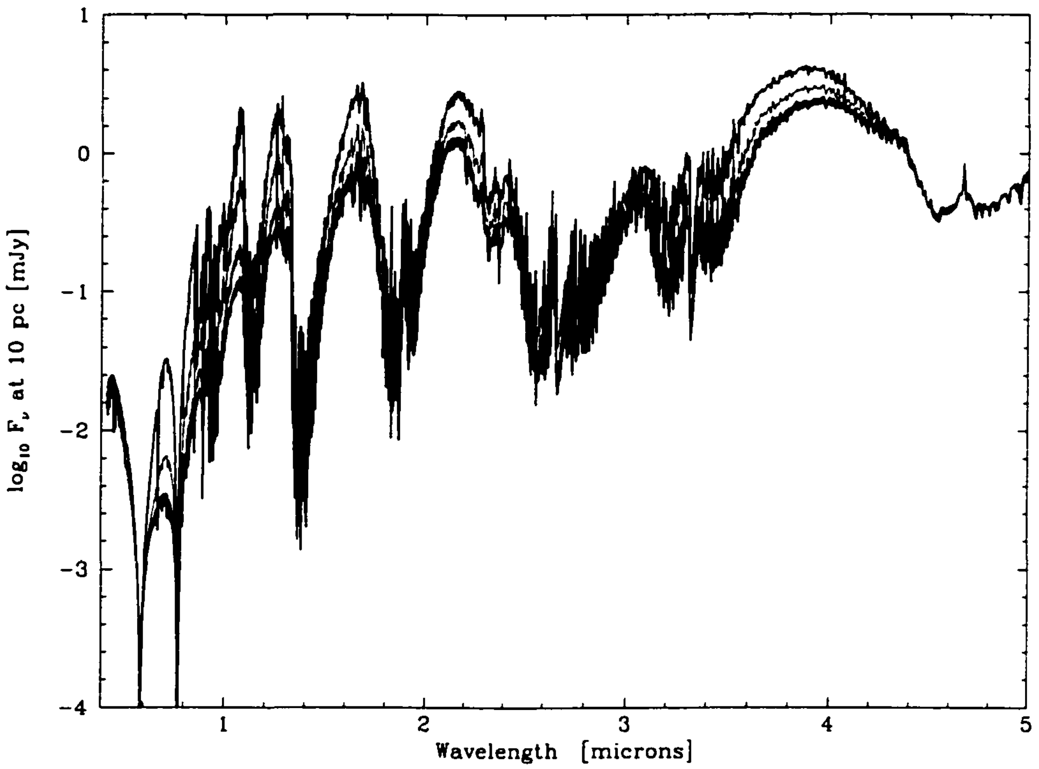

Figure 8.6 EGP emergent spectra as a function of inner boundary flux. Each spectral curve corresponds to each of the models depicted in Figure 8.5, from 1000 K (top curve) to 50 K (bottom curve, overlapping with that of 150 K and 300 K).

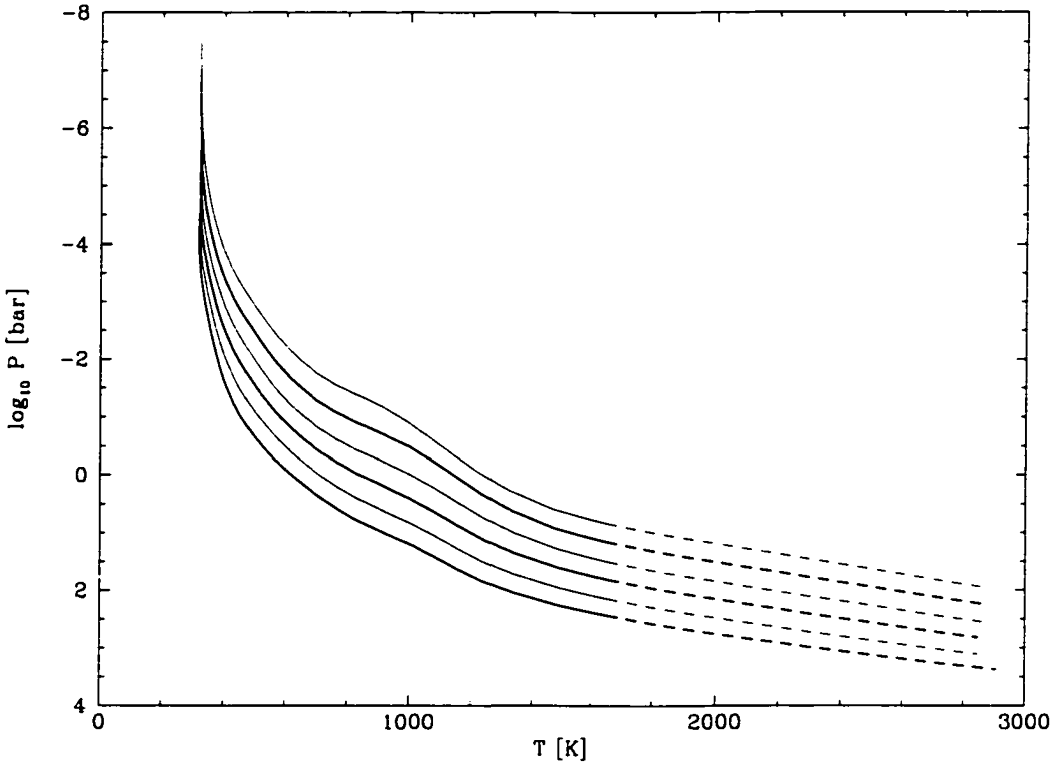

Figure 8.7 EGP T-P structure as a function of surface gravity. The surface gravity of a Class III model is varied from 10^3 cm s^{-2} (top curve) to 3×10^5 cm s^{-2} (a massive brown dwarf; bottom curve) in intervals of 1/2 dex.

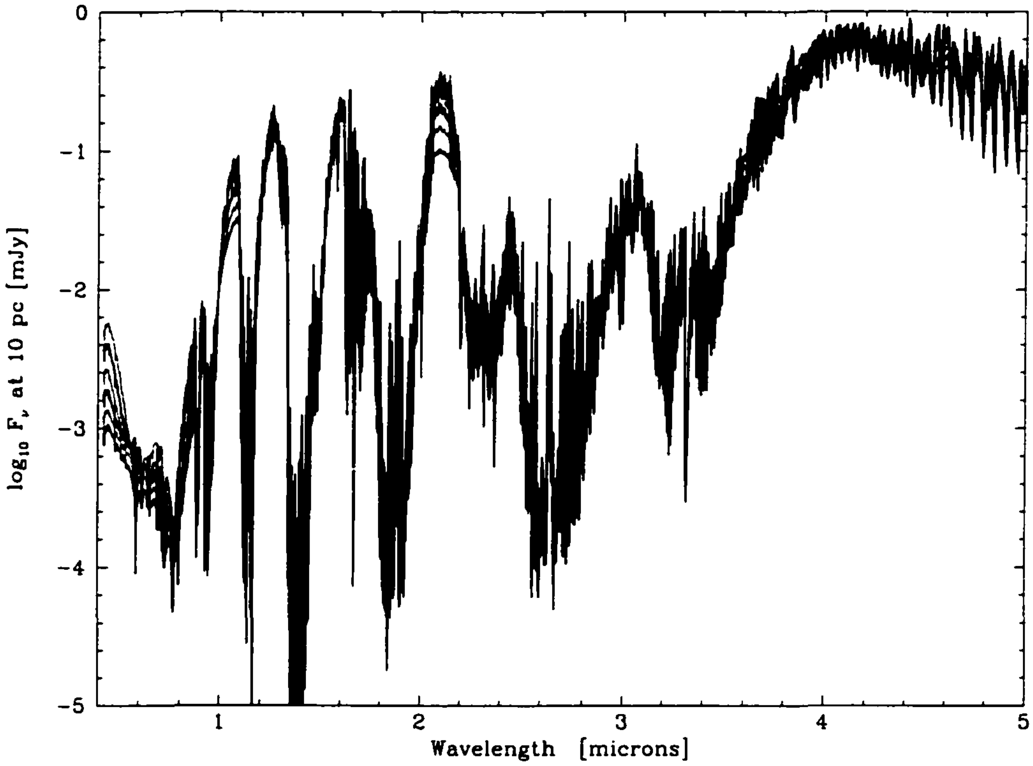

Figure 8.8 EGP emergent spectra as a function of surface gravity. Each spectral curve corresponds to each of the models depicted in Figure 8.7. For these models, an increase in gravity results in a general decrease in flux shortward of $\sim$ 2.2 μm, and an increase longward. Additionally, a larger gravity tends to reduce the peak-to-trough variations throughout the spectrum.

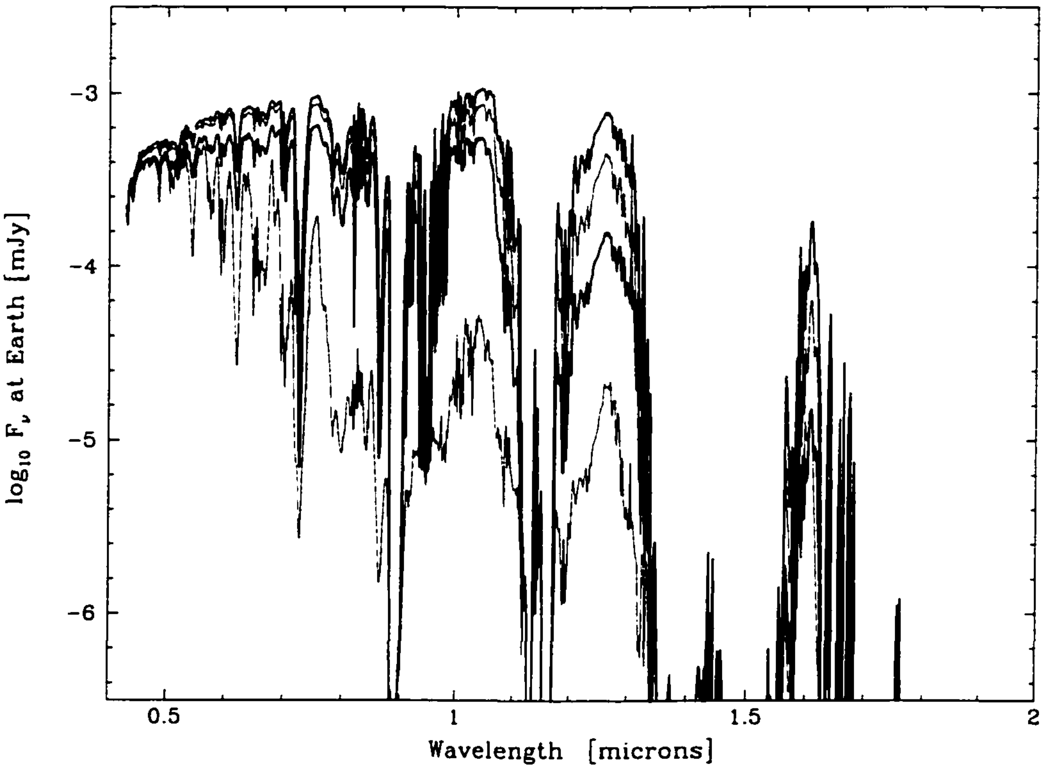

Figure 8.9 Effects of cloud particle size variation on the emergent spectrum of a Class II EGP. The resulting emergent spectra are shown for EGPs with three different median ice particle sizes, along with a cloud-free model of the same object. From top to bottom, the curves correspond to a size distribution peaked at 0.5 μm, one peaked at 5 μm, and another at 50 μm. In each case, 10% of the available H_2O was assumed to condense. The bottom curve is that of the cloud-free model.

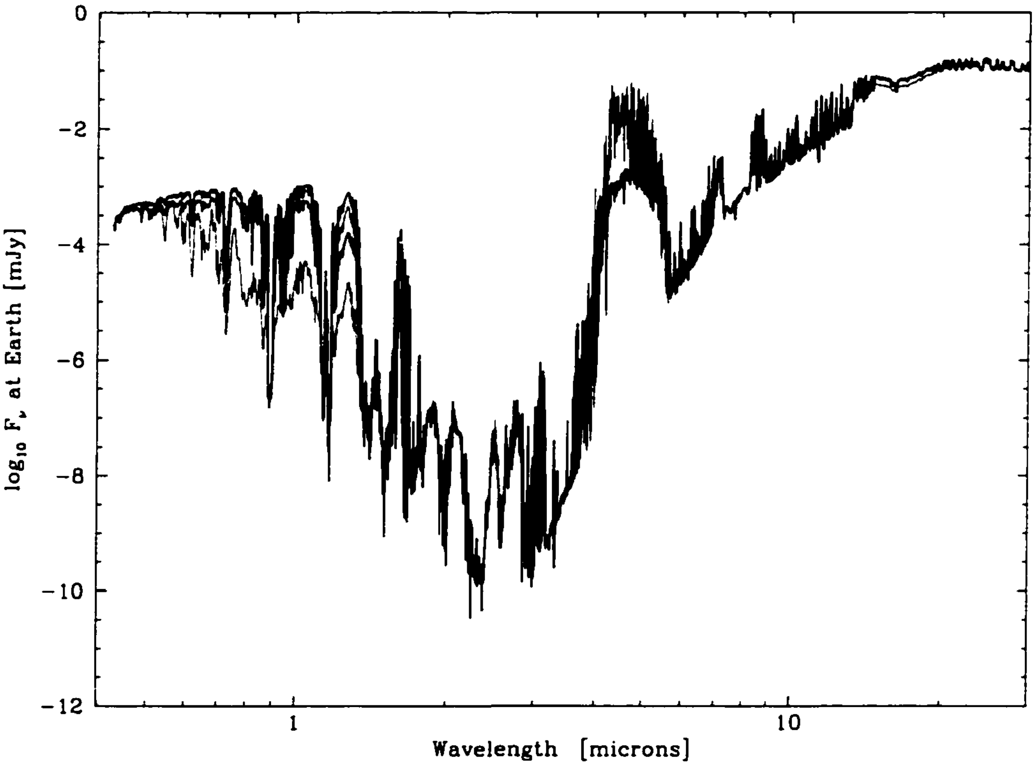

Figure 8.10 Effects of cloud particle size variation on the emergent spectrum of a Class II EGP out to 30 μm. Models are the same as depicted in Figure 8.9. In the 4-5 micron opacity window, the cloud-free model flux is up to 2 orders of magnitude greater than those that include clouds of any particle size.

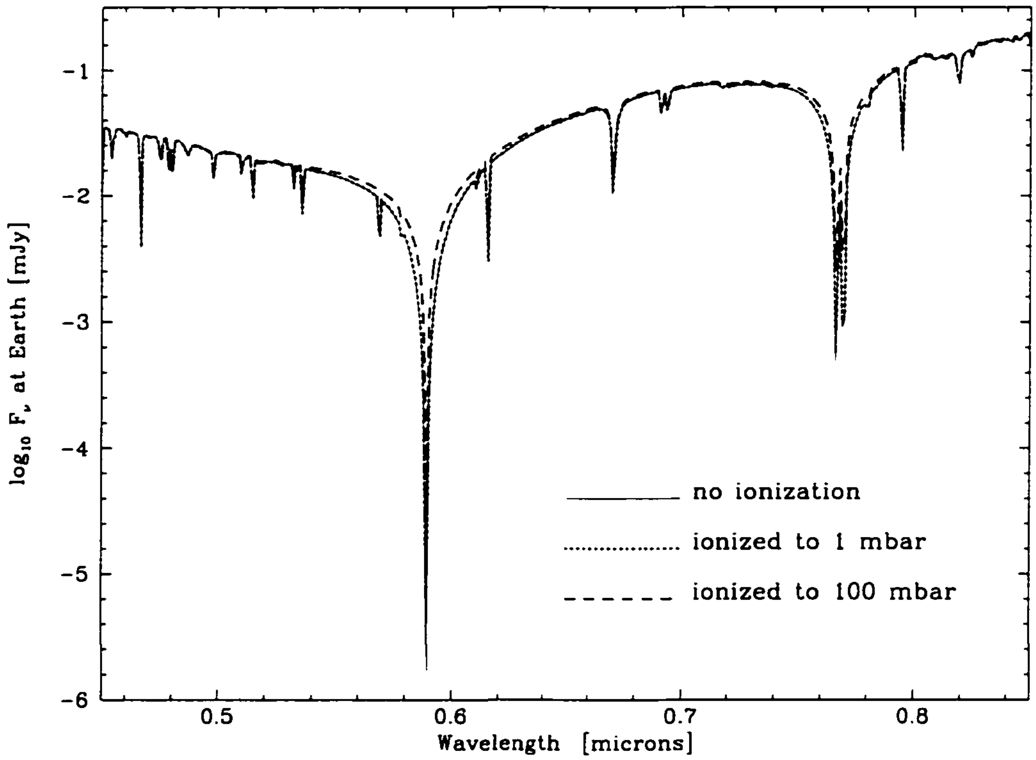

Figure 8.11 Simulated spectral effects of photoionization in the outermost atmosphere of a Class V roaster. For two ionization models, the alkali abundances were weighted by P/P_0 (for $P< P_0$ only), where $P_0 = 1$ mbar for one model and 100 mbar for the other. The 1-mbar ionzation model is hardly distinguishable from the no-ionization model, though for the 100-mbar model, the sodium and potassium resonance line absorption is reduced somewhat.

9 DETECTION AND IMAGING OF EGPs IN LIGHT OF THEORETICAL MODELS

EGP detection and imaging promises to be a very exciting field in the coming years. In addition to the highly successful radial-velocity detection methods, a number of very innovative ground-based and space-based methods are now under development or under serious consideration.

Theoretical models have had and will continue to have a firm place in guiding observational campaigns to detect EGPs. This final chapter reviews some of the many observational methods and their prospects for success in light of theoretical models. Where available, instrumental sensitivities are used in combination with spectral models to reveal which of the currently known EGPs are likely to be detectable.

The central problem in direct imaging, photometric phase detection, spectral separation methods, etc. is the huge contrast between the central star and its companion(s). The tiny planet-to-star flux ratios and minuscule angular separations require observers and instrumentalists to develop very clever detection methods. Space-based instrumentation has a clear advantage due to the absence atmospheric turbulence, but these missions are costly and will not be in operation for several years. Hence, a plethora of ground-based techniques are already in use or in the advanced stages of development.

9.1. Spectral Separation Methods

Close-in EGPs, such as 51 Peg b or τ Boo b, are separated from their primaries by only 0.8–4 milliarcseconds. While direct imaging of such systems from the ground at any wavelength would be a great challenge, a radial-velocity-based spectral separation method is being used by some researchers (Cameron et al. 1999; Charbonneau et al. 2000). With knowledge of the radial velocity variation of the stellar absorption lines due the primary's orbit about the system's center of mass, one can also expect a time-dependent opposite shift of the component of the stellar spectrum that is reflected by the planet. By modeling and subtracting the radial velocity-dependent stellar spectrum, the reflected component of the stellar spectrum should be left in the noisy residuals. The great difficulty is the large contrast between the actual stellar spectrum and the reflected component.

The intensity of the reflected stellar component depends upon the albedo of the EGP, which is highest in the visible region of the spectrum. At short enough wavelength (i.e., in the blue region of the spectrum), the thermal emission of even a Class V roaster is negligible. Hence, to a good approximation, all the flux in this region is reflected flux, so the wavelength dependence of the reflected stellar component can be derived by combining the stellar spectrum with the planetary albedo. According to my models, the phase-averaged planet-to-star flux ratio in this region is below 2×10^{-5} in all cases, and worse than 10^{-5} in some. When the planet is near full phase, these values may improve by a factor of 2-3, bringing the ratio into the vicinity of the detection limit of $\sim 0.5 - 1 \times 10^{-4}$, although the shift in the reflected component relative to the stellar spectrum approaches zero as the planet approaches opposition.

The difficulty of this method is illustrated by the false detection reported (and later retracted) of τ Boo b by Cameron et al. (1999), as discussed in §7.4. Yet, this technique may be our best hope for detecting a roaster in reflected light from the ground. Even if no detections are made, improvements in the accuracy of this method can provide upper limits to planetary albedos as a function of wavelength and orbital inclination, thereby putting minor contraints on the outer atmospheric compositions. However, the motivation and rationale for spectral separation methods will continue to be the detection of reflected light.

9.2. Ground-Based Differential Direct Imaging

Differential imaging entails the simultaneous imaging of a candidate system in two or more adjacent narrow band filters. The bandpasses are chosen so that at least one resides in a spectral region where a deep planetary absorption feature is expected, and another is situated in an adjacent opacity window, where the planet flux is predicted to be relatively large. However, the central star is bright in both bandpasses, so by imaging the candidate system and then differencing the two bandpass fluxes, one can virtually subtract out the offending starlight, hopefully revealing the dim planet. Just how dim a planet can be detected depends on a number of parameters, including the angular separation, the telescope size, instrument design, filter bandpasses, CCD efficiency, etc.

One instrument design makes use of dual Wollaston prisms for image splitting using the Arizona Infrared Imager and Echelle Spectrograph (ARIES), the MMT 6.5-meter telescope, and an adaptive optics (AO) secondary (Freed et al. 2002). With this set-up, on schedule for use in mid-2003, a 3σ detection in the H-band region is expected for an EGP-primary separation of 0.2″ and planet-to-star flux ratio of $\sim 3 \times 10^{-6}$. For larger separations, the detectable flux ratio improves significantly. For example, at a 1″ separation, the limit is $\sim 10^{-7}$ for a 2-hour exposure. These estimations are based on the placement of three narrow-band filters between 1.56 and 1.68 μm, toward the short-wavelength edge of a strong methane absorption feature. None of the currently known EGPs will be detectable given these sensitivities, since there are only a few with separations on the order of $\gtrsim 0.2''$ and their theoretical plant-to-star flux ratios are too low by 2-3 orders of magnitude. However, this method may succeed in discovering new, young Class III EGPs at 5-10+ AU from their primaries.

Another similar instrument, TRIDENT, is also optimized for the detection of EGPs with orbital distances greater than 5 AU in a narrow spectral region between 1.57 and 1.68 μm (Marois 2002). Using the CFHT 3.6-meter telescope with an AO system, a successful test observation was made of a faint companion 0.5″ from its primary. In this case, the contrast ratio was $\sim 2 \times 10^{-4}$, a very easy detection relative to that of an EGP. However, this detection confirms that the basic technique does work, and plans to use this instrument on the Gemini 8.2-meter telescope are under way.

9.3. Transit Searches and Photometric Reflected Light Detection

EGPs that have highly inclined orbits from our vantage point have a good chance of transiting their stars. In particular, this is true of Class V roasters, for which the probability of a transit is approximately 10%, assuming a random distribution of orbital inclinations (§7.2). The resulting stellar photometric dimming of $\sim 1\%$ is easily observable from the ground. This fact has led to an abundance of inexpensive ground-based transit searches far too numerous to discuss here. One such search, STARE (Brown & Charbonneau 1999), proved its worth with the detection of HD 209458b (see also Henry et al. 2000), the first and only (to date) transiting EGP. Like STARE, most other programs use small telescopes, a number of which monitor stars in an automated fashion. One search collaboration is OGLE (Optical Gravitational Lensing Experiment; Udalski et al. 2002). Originally developed for the detection of optical gravitational lensing events in the galactic disk and bulge, OGLE amassed an impressive collection of stellar light curves. Over 50,000 stars have been analyzed for variability due to a possible transiting planet (a light curve showing a flat-bottomed eclipse). For 42 of the stars, multiple transits were observed, and two of these may be close-in transiting EGPs given their short periods and photometric dimmings similar to that of HD 209458b (Udalski et al. 2002). Follow-up work, including a radial velocity determination of M$\sin i$ for these putative companions will be necessary to confirm their planetary nature.

In principle, one should be able to detect photometric variations for EGPs that do *not* transit their stars, due to differences in reflected light as a planet runs through its various orbital phases. The difficulty is that such variations are likely to be only a micromagnitude to tens of micromagnitudes, depending on the inclination of the orbit, the existence of high clouds, and their constituent species (Green et al. 2002; Seager et al. 2000). Such variations are too small to be observed from the ground, but several space-based missions are in the works, including MOST (Microvariability and Oscillations of Stars; Matthews et al. 2001), COROT (Antonello & Ruiz), MONS (Measuring Oscillations in Nearby Stars; primarily for use as an instrument to study stellar structure; Christensen-Dalsgaard 2000), and Kepler (Koch et al. 1998).

MOST is essentially complete and due for launch in April of 2003. This small, but very sensitive instrument, will be used for transit observations and for reflected light detection. MOST contains a 15-cm mirror and a single broad-band filter from 0.35 to 0.70 μm. An array of microlenses projects a large, stable image onto a CCD. Sensitivities are on the order of a few μmag, easily sufficient for the detection of Class V roasters with high enstatite clouds, which are quite reflective in the visible. However, if the clouds are buried and/or are composed of more highly absorbing species (such as forsterite), detection will be much more difficult. At the very least, MOST will constrain the outer atmospheric compositions of a number of close-in EGPs, but hopefully a few ground-breaking detections will be made.

COROT, scheduled for launch in 2005, will be capable of multicolor photometry. Its wide field of view, 27.4-cm telescope is suitable for the simultaneous monitoring of many stars. Throughout its mission, 6,000-12,000 stars will be targeted in search of transits of planets from terrestrial size to gas giants. Additionally, detections of reflected light from close-in nontransiting planets through blue and red bandpasses may be possible. Such observations could provide rudimentary color data for some EGP atmospheres.

Kepler has been selected as a NASA Discovery mission for the detection of Earth-like planets, and it is scheduled for launch in 2006. A much larger instrument than MOST or COROT, Kepler has a 1.6-meter primary mirror and an array of 42 CCD detectors. It will monitor $\sim$ 100,000 stars in visible light in search of transiting planets. Literally hundreds of EGP transits are expected, and follow-up radial-velocity measurements will be possible for some of the closer systems. A determination of the planetary albedos of transiting planets should be possible by inferring a planetary radius from the transit depth, a semimajor axis from the period of the orbit. and the amplitude of the reflected light modulation between transits.

9.4. Interferometric Imaging

The precision of interferometry provides promising methods for the detection of EGPs. These include both astrometric and direct imaging techniques. which are being developed for ground-based and space-based programs.

One of the most innovative methods is nulling interferometry, whereby the light from a star is strongly suppressed while that from a companion is not. A nulling interferometer is similar to a Michelson interferometer. except that the path lengths from a pair of collectors are purposely maintained at a difference of half a wavelength so that the light from the star interferes destructively. However, at a minuscule separation angle from the central star (perhaps at the position of a planetary companion), the phase relation for the incoming radiation is such that the light will interfere constructively. Moreover, the instrument can be tuned so that the peak of the constructive interference occurs at various angles from the central star.

The nulling of a star was tested successfully on the multiple-mirrored MMT telescope before its decommissioning and upgrade to a 6.5-meter telescope (Hinz et al. 2000). However, the successful detection of EGPs likely will be left to the Large Binocular Telescope Interferometer (LBTI), a twin 8.4-meter mirror common-mount telescope due to be operational by late 2005. Using the telescope's AO system along with a nulling beam combiner, which includes a dielectric material to correct for the color-dependence of light interference, at least a few of the currently known EGPs should be detectable according to my models. An *image* of the field around a nulled star, not fringes, will be observable because the point spread function is broader than the transmission function due to the interferometer (Hinz 2001). In the infrared L′ Band ($\sim$ 3.6 μm), the LBTI sensitivity is expected to be 2.1 μJy for a 1-hour integration, and the M-band (4.5-5 μm) sensitivity should be 21 μJy for a 1-hour integration. A planet-star separation of $\gtrsim$ 0.03″ will be required (Hinz 2001). Optical wavelengths are not currently being considered for ground-based nulling due to the enormous difficulty of wavefront corrections at these shorter wavelengths.

Among the systems I have modeled, υ And c and d, 55 Cnc d, and ϵ Eri b all have sufficient angular separations from their primaries. In the L′ band, υ And c's average flux density is near 10 μJy, roughly a factor of five greater than the LBTI sensitivity for a 1-hour integration. Upsilon And d will be too dim in the L′ band by about an order of magnitude, but its M-band flux density of $\sim$ 20 μJy is commensurate with the LBTI sensitivity in that wavelength region, and the υ And c M-band flux density is approximately a factor of 5 greater. Although their angular separations are large, my ϵ Eridani b and 55 Cnc d models indicate that these objects will be too dim for imaging via nulling interferometry with the LBTI in either the L′ or M bands.

A nulling interferometer is one of two proposed designs for the Terrestrial Planet Finder (TPF), part of a very ambitious plan by NASA for the detection and spectroscopy of Earth-sized planets. The LBTI will provide a ground-based test of the techniques that in principal can work even better outside of Earth's turbulent atmosphere. In addition to the characterization of terrestrial planets, TPF should provided unprecedented spectral data for EGP atmospheres. Launch is anticipated between 2012 and 2015.

Another innovative interferometric development is the differential phase method (Akeson & Swain 2000). Using the Keck Interferometer in the infrared, a faint companion might be detected by simultaneously measuring the fringe phase at two (or more) wavelengths at which the planet/star flux ratio is expected to differ. Because the primary and secondary sources provide different fractions of the total light received at each of two wavelengths, and because the fractional fringe separation depends on wavelength, a small phase difference will occur. With the twin 10-meter apertures of the Keck, a phase difference as small as 0.1 milliradian might be detectable (Akeson & Swain 2000). Due to their higher luminosities, hot EGPs with temperatures of $\gtrsim$ 1000 K are favored by this technique. Of the currently known EGPs, most of the close-in Class IV and V objects meet this criterion.

The differential phase signal in radians is roughly given by twice the difference of the planet-to-star flux ratios (Akeson 2002, private communication). This estimate holds for separations as small as ~2 milliarcseconds. Using the H and K bands (Akeson & Swain 2000), the Class V roasters that I have modeled, such as 51 Peg b, τ Boo b, and υ And b, fall into the 0.1-0.2 milliradian phase-difference range using the H and K bands, the two bands emphasized by Akeson & Swain (2000), indicating that these roasters may be detectable by this method. In contrast, Class IV EGPs translate to well below 0.1 milliradians.

A recent test run on the Palomar Testbed Interferometer (PTI) revealed that the differntial phase method may have some difficulties in practice reaching 0.1 milliradian accuracy, probably due to water vapor turbulence in Earth's atmosphere (Akeson et al. 2000). Some ideas for overcoming these difficulties are currently in the works. A refinement of the differential phase method is highly desirable, because if it does prove to be successful, not only detections, but low-resolution spectra of roasters may be obtained by applying it at various wavelengths.

9.5. Interferometric Astrometry

Another class of interferometric work for the discovery of new EGPs is high-accuracy, infrared astrometry. This technique will complement the radial velocity data for those EGPs currently known, providing orbital inclinations from which companion masses can be derived. The two dominant ground-based efforts now in development are the VLTI (Very Large Telescope Interferometer) and the Keck Interferometer. Using standard Michelson interferometry techniques, astrometric accuracies of ~ 10 microarcseconds are expected. Such precision will enable the measurement of planet masses and inclinations for a majority of the EGP systems known today.

Astrometric interferometry is an indirect detection method because it is the position of the central star that is monitored as it orbits the system's center of mass. The reflex amplitude of the star is proportional to the mass and distance of the secondary ($a_* = a_p M_p / M_*$). Therefore, with a system such as τ Boo b, for which the planet-star angular separation is ~ 2.7 milliarcseconds, the reflex motion of the F7V primary will be ~ 11 microarcseconds, assuming a planetery mass of 5 M_J. Most other roasters are less massive than τ Boo, so they may fall below the detection limit (depending on their angular separation). Nevertheless, the inclinations and masses of most of the currently known Class I through Class IV EGPs should be revealed by this method.

In the case of the VLTI, its auxiliary 1.8-meter telescopes will be dedicated to full-time interferometry, while the 8.2-meter telescopes will be used for interferometry only intermittently. Due to a baseline of up to 202 meters, very high accuracy will be possible. At 10 parsecs, a Jupiter could be detected at an orbital distance as small as 0.1 AU, and that of a 0.1 $M_J$object at 1 AU should be measurable as well (Paresce 2001). The Keck Interferometer, with a somewhat shorter baseline, is expected to have similar, though perhaps slightly inferior, resolving power (van Belle & Vasisht 1998).

The Space Interferometry Mission (SIM), scheduled for launch in 2009, is expected to achieve 1-microarcsecond astrometry, an accuracy capable of revealing the orbits of all the EGP systems discovered to date. The 10-meter baseline instrument could also act as an ideal space-based testbed for one of two possible designs for the larger TPF mission. GAIA, a European equivalent of SIM in terms of astrometric accuracy, is scheduled for launch between 2010 and 2012.

9.6. Coronagraphic Imaging

Coronagraphic imaging is a direct imaging method in which starlight is blocked by a specially-designed phase mask, or coronagraph. Without such a mask, the extremely faint image of an off-axis EGP would be washed out. Due to the difficulties of visible and near-infrared imaging from the ground, coronagraphic instruments suitable for EGP detection are space-based.

Eclipse is a 1.8-meter visible and near-infrared coronagraphic space telescope currently in development at Jet Propulsion Laboratory (Trauger et al. 2000; Trauger et al. 2001). Specifically designed for direct imaging of nearby ($\sim$ 15 pc) EGPs, this ambitious instrument will contain precision wavefront control technology to correct for even minute imperfections in the optical systems. With such technology, Eclipse is predicted to reduce the scattered and diffracted starlight between 0.3 and a few arcseconds by 3 orders of magnitude better than any HST instrument (Trauger et al. 2000). Within 1″ of an F or G star, 10^9-contrast imaging capability is expected for a wide R-band filter (0.55-0.85 μm.), and for angular separations of only 0.1–0.3″, 10^8 contrast imaging may be possible. ϵ Eri b, has a separation of $\sim$ 1″ and a modeled R-band plant-to-star flux ratio of $\sim 3 \times 10^{-9}$, making it a very likely candidate for direct imaging by Eclipse. With a separation of $\sim$ 0.45″ and a planet-to-star ratio of $\sim 3 \times 10^{-10}$, 55 Cnc d will be close to the detection limit, but it may be slightly too dim for direct R-band imaging.

The large 6.5-meter Next Generation Space Telescope, scheduled for launch in 2010, will house the Near Infrared Camera (NIRCam), including a coronagraphic module. From 2-5 μm, the NIRCam coronagraph will be capable of 10^8–10^9 high-contrast imaging for planet-star separations of $\gtrsim$ 0.1″ (Rieke et al. 2002). Tunable narrow-band filter modules from $\sim$ 2.5-4.5 μm will allow for the construction of infrared EGP spectra (M. Rieke 2002, private communication). Of the detected EGPs that I have modeled, υ And d, 55 Cnc d, and ϵ Eri b all have sufficient angular separations and planet-to-star flux ratios to be imaged by NIRCam. For υ And d, the most advantageous wavelength regions for imaging are the J band (2.2 μm) and the broad wavelength region between 3.6 and 5 μm, according to my theoretical spectral models. 55 Cnc d and ϵ Eri b have sufficient planet-to-star flux ratios for coronagraphic imaging within only the 4-5 μm opacity window.

The Extra-solar Planet Imager (ESPI) is a space telescope design proposal, the basis of which is a 1.5-meter square aperture with a custom mask (Melnick et al. 2001). The resulting diffraction pattern is cross-shaped rather than circular, and the telescope can be rotated so that a faint companion EGP appears between two edges of the pattern. The planet-star separation limit is expected to be in the 0.3″

range. Hence, for many systems, Jupiter-like EGPs orbiting at a few AU or more may be detectable. Another space-based coronagraphic instrument of similar size is the Jovian Planet Finder (JPF), a 1.46-meter coronagraphic optical telescope that would be located on the International Space Station. The JPF would survey 50 of the closest stars for EGPs orbiting between 2 and 20 AU, and 2000 stars for more massive brown dwarf companions.

A visible coronagraphic instrument is also a design concept for TPF. If this path is chosen instead of the interferometric design, extremely precise optics will be required to image terrestrial planets. Even minute imperfections scatter light and degrade contrast, so an AO system will be used to correct the wavefront for such imperfections (as with Eclipse). Whichever concept is adopted, it is assured that any instrument designed to reveal information about terrestrial planets and their atmospheres will provide even more detailed information about the gas giants known today and the hundreds more that will be discovered in the coming years.

REFERENCES

Ackerman, A., & Marley, M. S. 2001, Astrophysical Journal, **556**, 872

Akeson, R. L. & Swain, M. R. 2000, in *From Giant Planets to Cool Stars*, ed. C. A. Griffith & M. S. Marley, ASP Conference Series, **212**, 300

Akeson, R. L., Swain, M. R., & Colavita, M. M 2000, in *Interferometry in Optical Astronomy*, ed. P. J. Lena, Proc. SPIE 4006, 321

Anders, E. & Grevesse, N. 1989, Geochim. Cosmochim. Acta, **53**, 197

Antonello, E. & Ruiz, S. M. 2002, *The Corot Mission*, http://www.astrsp-mrs.fr/projects/corot/corotmission.ps

Baliber, N. R. & Cochran, W. D. 2001, AAS DPS, **40**, 40.01

Banfield, D., Geirasch, P. J., Bell, M., Ustinov, E., Ingersoll, A. P., Vasavada, A. R., West, R. A., & Belton, M. J. S. 1998, Icarus, **135**, 230

Barman, T. S., Hauschildt, P. H., & Allard, F. 2001, Astrophysical Journal, **556**, 885

Bar-Nun, A., Kleinfeld, I., &Ganor, E. 1988, J. Geophys. Res., **93**, 8383

Black, D. C. & Stepinski, T. F. 2001, AAS DDA Meeting 32, 13.03

Boccaletti, A. 1999, The NGST Coronagraphic Mode Study, http://www.nasa.ngst.gov

Bohren, C. F. & Huffman, D. R. 1983, *Absorption and Scattering of Light by Small Particles*, (New York: Wiley)

Brown, T. M. & Charbonneau, D. 1999, BAAS, **31**, 1534

Burrows, A., Marley, M., Hubbard, W. B., Lunine, J. I., Guillot, T., Saumon, D., Freedman, R., Sudarsky, D., & Sharp, C. 1997, Astrophysical Journal, **491**, 856

Burrows, A. & Sharp, C. M. 1999, Astrophysical Journal, **512**, 843

Burrows, A., Marley, M., & Sharp, C. M. 2000, Astrophysical Journal, **531**, 438

Burrows, A., Guillot, T., Hubbard, W. B., Marley, M. S., Saumon, D., Lunine, J. I., & Sudarsky, D. 2000b, **534**, 97

Burrows, A., Burgasser, A. J., Kirkpatrick, J. D., Liebert, J., Milsom, J. A., Sudarsky, D., & Hubeny, I. 2002, Astrophysical Journal, **573**, 394

Burshtein, Z., Shimony, Y., & Levy, I. 1993, J. Opt. Soc. Am. A, **10**, 2246

Butler, R. P., Marcy, G. W., Williams, E., Hauser, H. & Shirts, P. 1997, Astrophysical Journal Letters, **474**, L115

Butler, R. P., Marcy, G. W., & Vogt, S. S. & Apps, K. 1998, PASP, **110**, 1389

Butler, R. P, Marcy, G. W., Fischer, D. A., et al. 1999, Astrophysical Journal, **526**, 916

Butler, R. P., Marcy, G. W., Vogt, S. S., Tinney, C., Jones, H., McCarthy, C., Penny, A., Apps, K., & Carter, B. 2002, Astrophysical Journal (in press)

Cameron, A. C., Horne, K., Penny, A., & James, D. 1999, Nature, **402**, 751

Castor, J. I., Dykema, P. G., & Klein, R. I. 1992, Astrophysical Journal, **387**, 561

Chamberlain J. & Hunten, D. 1987, Theory of Planetary Atmospheres, 2nd Edition (San Diego: Academic Press Inc.), 201

Chanover, N. J, Kuehn, D. M., & Beebe, R. F. 1997, Icarus, **128**, 294

Charbonneau, D., Brown, T. M., Latham, D. W., & Mayor, M. 2000, Astrophysical Journal Letters, **529**, L45

Charbonneau, D., Brown, T. M., Noyes, R. W., & Gilliland, R. L. 2002, Astrophysical Journal, **568**, 377

Christensen-Dalsgaard, J. 2000, http://bigcat.obs.aau.dk/hans/mons/

Clampin, M., Ford, H. C., Illingworth, G., & Petro, L. 2001, AAS Meeting 199, 33.02

Cody, A. M. & Sasselov, D. D. 2002, Astrophysical Journal, **569**, 451

Cooper, C. S., Sudarsky, D., Milsom, J. A., Lunine, J. I., & Burrows, A. 2002, submitted to the Astrophysical Journal

Deirmendjian, D. 1964, Applied Optics, **3**, 187

Deirmendjian, D. 1969, *Electromagnetic Scattering on Spherical Polydispersions*, (New York: Elsevier)

Delfosse, X., Forveille, T., Mayor, M., Perrier, C., Naef, D., & Queloz, D. 1998, Astronomy & Astrophysics, **338**, L67

Dorschner, J., Begemann, B., Henning, Th., Jager, C., and Mutschke, H. 1995, Astronomy & Astrophysics, **300**, 503

Draine, B. T. 2000, Astrophysical Journal, **532**, 273

Edgington, S. G., Atreya, S. K. Trafton, L. M., Caldwell, J. J, Beebe, R. F., Simon, A. A., West, R. A., & Barnet, C. 1998, Icarus, **133**, 192

Fortney, J. J., Sudarsky, D., Hubbard, W. B., Burrows, A., Lunine, J. I., & Cooper, C. S. 2002, *in preparation*

Freed, M. E., Close, L. M., & McCarthy, D. W. 2002, in *Scientific Frontiers in Research on Extrasolar Planets*, ed. D. Deming & S. Searger, *in preparation*

Gatewood, G. 2000, BAAS, **32**, 32.01

Gervais, F. 1990, in Handbook of Optical Constants of Solids II, ed. E. D. Palik (Orlando: Academic), 766

Gierasch, P. J., Conrath, B. J., & Magalhaes, J. A. 1986, Icarus, **67**, 456

Goukenleuque, C., Bezard, B., Joguet, B., Lellouch, E., & Freedman, R. 2000, Icarus **143**, 308

Gray, D. F. 1997, Nature, **385**, 795

Gray, D. F. & Hatzes, A. P. 1997, Astrophysical Journal, **490**, 312

Greaves, J., Holland, W., Moriarty-Schiven G., et al. 1998, Astrophysical Journal Letters, **506**, L133

Green, D., Mathews, J., & Seager, S. 2002, in *Scientific Frontiers in Research on Extrasolar Planets*, ed. D. Deming & S. Searger, *in preparation*

Griffith, C. A., Bezard, B., Owen, T., & Gautier, D. 1992, Icarus, **98**, 82

Gudzenko, L. I., Evstigneev, V. V., Filippov, S. S., & Yakovlenko, S. I. 1974, Teplofizika Vysokikh Temperatur, **12**, 96

Guillot, T., Burrows, A., Hubbard, W. B., Lunine, J. I., & Saumon, D. 1996, Astrophysical Journal, **459**, 35

Guillot, T. & Showman, A. P. 2002, Astronomy and Astrophysics, **385**, 156

Han, I., Black, D. C., & Gatewood, G., Astrophysical Journal Letters, **548**, L57

Hanel, R. A., Conrath, B. J., Herath, L. W., Kunde, V. G., & Pirraglia, J. A. 1981, J. Geophys. Res., **86**, 8705

Hatzes, A., Cochran, W., McArthur, B., et al. 2000, Astrophysical Journal Letters, **544**, L145

Helmer, M. & Plane, J. M. C. 1993, Journal of Geophysical Research, **98**, 23207

Henry, G., Marcy, G. W., Butler, R. P., & Vogt, S. S. 2000, Astrophysical Journal Letters, **529**, L41

Hinz, P. M, Angel, J. R. P., Woolf, N. J., Hoffman, W. F., & McCarthy, D. W. 2000, in *Interferometry in Optical Astronomy*, ed. P. J. Lena, Proc. SPIE 4006, 349

Hinz, P. M. 2001, PhD Thesis, The University of Arizona

Hubbard, W. B., Fortney, J. F., Lunine, J. I., Burrows, A., Sudarsky, D., & Pinto, P. A. 2001, Astrophysical Journal, **560**, 413

Hubeny, I. 1992, in *The Atmospheres of Early-Type Stars*, ed. U. Heber & C. J. Jeffery, Lecture Notes in Phys. 401, (Berlin: Springer), 377

Hubeny, I. & Lanz, T. 1995, Astrophysical Journal, **439**, 875

Irvine, W. M. 1964, Journal of the Optical Society of America, **55**, 16

Karkoschka, E. 1994, Icarus, **111**, 174

Karkoschka, E. 1998, Icarus, **133**, 134

Khare, B. N., Sagan, C. 1984, Icarus, **60**, 127

Koch, D., Borucki, W., Webster, L., Dunham, E., Jenkins, J., Marrion, J., & Reitsema, H. 1998, SPIE Conference 3356: *Space Telescopes and Instruments V*, 599

Kuehn, D. M. & Beebe, R. F. 1993, Icarus, **101**, 282

Kunde, V, Hanel, R., Maguire, W., Gautier, D., Baluteau, J. P., Marten, A., Chedin, A., Husson, N., & Scott, N. 1982, Astrophysical Journal, **263**, 443

Kurucz, R. 1970, Smithsonian Astrophysical Observatory Special Report, 309

Kurucz, R. 1994, *Kurucz CD-ROM No. 19*, (Cambridge: Smithsonian Astrophysical Observatory)

Latham, D. W., Stefanik, R. P., Mazeh, T., Mayor, M., & Burki, G. 1989, Nature, **339**, 38

Lodders, K. 1999, Astrophysical Journal, **519**, 793

Lodders, K. 2002, Astrophysical Journal (submitted)

Marcy, G. W., Butler, R. P., Vogt, S. S, Fischer, D., & Lissauer J. J. 1998, Astrophysical Journal Letters, **505**, L147

Marcy, G. W., Butler, R. P., Fischer, D. A., Laughlin, G., Vogt, S. S., Henry, G. W., & Pourbaix, D. 2002, submitted to the Astrophysical Journal

Marley, M. S., Gelino, C., Stephens, D., Lunine J. I., & Freedman, R. 1999, Astrophysical Journal, **513**, 879

Marois, C. 2002, in *Scientific Frontiers in Research on Extrasolar Planets*, ed. D. Deming & S. Searger, *in preparation*

Martonchik, J. V., Orton, G. S., & Appleby, J. F. 1984, Applied Optics, **23**, 541

Matthews, J. M., Kuschnig, R., Walker, G. A. H. et al. in *The Impact of Large-Scale Surveys on Pulsating Star Research*, ed. L. Szabados & D. Kurtz, p. 74

Mayor, M. & Queloz, D. 1995, Nature, **378**, 355

Mayor, M., Naef, D., Udry, S., Santos, N., Queloz, D., Melo, C., & Confino, B. 1999, Exoplanet message no. 116

Mayor, M., Naef, D., Pepe, F., Queloz, D., Santos, N., Udry, S., & Burnet, M. 2000, in *Planetary Systems in the Universe*, IAU Symposium 202, eds. A Penny, P. Artymowicz, A.-M. Lagrange, & S. Russel, ASP Conference Series

Mazeh, T., Naef, D., Torres, G., et al. 2000, Astrophysical Journal Letters, **532**, L55

Melnick, G. J., Fischer, D., Geary, J. C. et al. 2001, AAS Meeting 199, 09.10

Mihalas, D. 1978, *Stellar Atmospheres*, (New York: Freeman & Co.)

Mihalas, D. 1980, Astrophysical Journal, **238**, 1034

Milkey, R. W., Shine, R. A., & Mihalas, D. 1975, Astrophysical Journal, **202**, 250

Motley, R. W. & Jassby, D. L. 1970, Physical Review A, **1**, 265

Niemann et al. 1996, Science, **272**, 846

Noll, K. S., Knacke, R. F, Tokunaga, A. T., Lacy, J. H., Beck, S., & Serabyn, E. 1986, Icarus, **65**, 257

Noy, M., Podolak, M. & Bar-Nun, A. 1981, J. Geophys. Res., **86**, 11985

Paresce, F. 2001, *Scientific Objectives of the VLTI Interferometer*

Plane, J. M. C. 1991, International Reviews in Physical Chemistry, **10**, 55

Pope, S. K., Tomasko, M. G., Williams, M. S., Perry, M. L., Doose, L. R., & Smith, P. H. 1992, Icarus, **100**, 203

Rages K. A, Galileo Imaging Team 1997, AAS DPS, **29**, 19.17

Rieke, M., Beichman, C., Eisenstein, D., & Meyer, M. 2002, http://ircamera.as.arizona.edu/nircam/

Rossman, G. R. & Taran. M. N. 2001, American Mineralogist, **86**, 896

Ryan, S. G. 2001, Monthly Notices of the Royal Astronomical Society (in press)

Rybicki, G. B. & Hummer, D. G. 1991, Astronomy & Astrophysics, **245**, 171

Santos, N. C., Israelian, G., and Mayor, M. 2001, Astronomy & Astrophysics (in press)

Scott, A. & Duley, W. W. 1996, Astrophysical Journal Supplements, **105**, 401

Saumon, D., Chabrier, G., & Van Horn, H. 1995, Astrophysical Journal Supplments, **99**, 713

Seager, S. & Sasselov, D. D. 1998, Astrophysical Journal, **502**, 157

Seager, S., Whitney, B. A. & Sasselov, D. D. 2000, Astrophysical Journal, **540**, 504

Seager, S. & Sasselov, D. D. 2000, Astrophysical Journal, **537**, 916

Smith, P. H. 1986, Icarus, **65**, 264

Stepinski, T. F. & Black, D. C. 2001, Astronomy & Astrophysics, **371**, 250

Strong, K., Taylor, F. W., Calcutt, S. B., Remedios, J. J., & Ballard, J. 1993, Journal of Quantitative Spectroscopy and Radiative Transfer, **50**, 363

Sudarsky, D., Burrows, A., & Pinto, P. 2000, Astrophysical Journal, **538**, 885

Tomasko, M. G., Karkoschka, E., & Martinek, S. 1986, Icarus, **65**, 218

Trafton, L. M. 1967, Astrophysical Journal, **147**, 765

Trauger, J., Backman, D., Brown, R. A. et al. 2000, AAS Meeting 197, 49.07

Trauger, J., Hull, A. B., & Redding, D. A. 2001, AAS Meeting 199, 86.04

Tropf, W. J. & Thomas, M. E. 1990, in Handbook of Optical Constants of Solids II, ed. E. D. Palik (Orlando: Academic), 883

Tsuji, T., Ohnaka, K., & Aoki, W. 1999, Astrophysical Journal Letters, **520**, L119

Udalski, A., Paczynski, B., Zebrun, K., Szymanski, M., Kubiak, M., Soszynski, I., Szewczyk, O., Wyrzykowski, L. & Pietrzynski, G. 2002, *The Optical Gravitational Lensing Experiment. Search for Planetary and Low-Luminosity Object Transits in the Galactic Disk. Results of 2001 Campaign*, http://bulge.princeton.edu/ ogle

Unwin, S. C. & Shao, M. 2000, in Interferometry in Optical Astronomy, ed. P. J. Lena & A. Quirrenbach, 754

van Belle, G. & Vasisht, G. 1998, *The Keck Interferometer Science Requirements Document, Revision 2.2*, Jet Propulsion Laboratory

van de Hulst, H. C. 1957, *Light Scattering by Small Particles*, (New York: Dover)

van de Hulst, H. C. 1974, Astronomy & Astrophysics, **35**, 209

Verner, D. A. & Ferland, G. J. 1996, Astrophysical Journal, **103**, 467

Warren, S. G. 1984, Applied Optics, **23**, 8

Warren, S. G. 1991, in *Handbook of Optical Constants of Solids II*, ed. E. Palik (San Diego: Academic Press, Inc.), 236

Weast, R. C. 1983, Handbook of Chemistry and Physics (64th edition; Boca Raton: CRC)

West, R. A. 1979, Icarus, **38**, 34

West, R. A., Strobel, D. F. & Tomasko, M. G. 1986, Icarus **65**, 161

West, R. A. 1988, Icarus, **75**, 381

Zheng, C. & Borysow, A. 1995, Icarus, **113**, 84